3

METAMATERIAL TRANSMISSION LINES: FUNDAMENTALS, THEORY, CIRCUIT MODELS, AND MAIN IMPLEMENTATIONS

3.1 INTRODUCTION, TERMINOLOGY, AND SCOPE

There is not a universal definition of the term *metamaterial*. However, there is a general agreement that metamaterials are artificial structures exhibiting unusual and controllable electromagnetic (EM), optical, or acoustic properties.[1] Metamaterials are periodic (or quasi-periodic) structures with unit cells (or "atoms") consisting of combinations of metals and/or dielectrics.[2] Rather than from the composition of their constituent elements, the unusual (and sometimes exotic) properties of metamaterials come from their structure. Therefore, by properly engineering or designing these artificial materials, it is possible not only to achieve properties beyond those properties that can be found among natural media,[3] but also to control or tune them, in order to obtain certain requirements, specifications, or performance. Probably, the most popular metamaterial structures (or at least those that have been able to attract the interest of broadcasting media) are those devoted to hide objects (also known

[1] Sometimes, metamaterials are classified according to the nature of the waves to which they interact as acoustic, electromagnetic (including RF, microwave, millimeter-wave, and terahertz), or optical (photonic) metamaterials.

[2] Exceptions to this are random media, although for many researchers such artificial structures do not belong to the domain of metamaterials. On the other hand, by quasiperiodic structures we refer to artificial structures where the period, or any other structure parameter, is modulated in order to obtain variable properties with position, or improved functionalities.

[3] From the Greek language, the prefix "meta" means "beyond," "of a higher order."

Artificial Transmission Lines for RF and Microwave Applications, First Edition. Ferran Martín.

as invisibility cloaks.[4]) These structures are clear examples of metamaterials engineered to achieve unprecedented properties, such as controllable wave guiding, in such a way that scattering is inhibited and the cloak (and the "objects" inside it) cannot be detected.

For many researchers in the field, the term *metamaterial* is restricted only to those artificial periodic structures with unit cell dimensions much smaller than the guided wavelength. In these artificial materials, the incident radiation "sees" the structure as a continuous (or effective) medium, so that it can be described or modeled in terms of effective parameters, such as the effective permittivity, permeability, or refractive index (these effective medium metamaterials operate in the refraction regime). For other researchers, metamaterials do also include those periodic structures exhibiting their properties at wavelengths comparable to the period of the structure (i.e., working in the diffraction regime), such as the photonic crystals (PCs) or electromagnetic bandgaps (EBGs), studied in the previous chapter (particularly EBG-based artificial lines). It is obvious that the properties of effective medium metamaterials and PCs (or EBGs) come from different principles, but a discussion on the scope of the term *metamaterial* is not worthy. Nevertheless, effective medium metamaterials seem to offer a higher degree of flexibility and controllability (as compared to PCs or EBGs) for the design of novel functional devices, or to improve the performance of existing ones. Indeed, the research activity in the field has been progressively dominated by effective medium metamaterials in the recent years, and probably this explains that most researchers consider the operation in the refraction regime as a requirement for designating an artificial periodic structure as a metamaterial.

In Chapter 2, periodic transmission lines based on EBGs or capacitively loaded transmission lines were studied, but they were not designated as metamaterial transmission lines. Essentially, EBG-based lines are periodic structures able to inhibit signal propagation at certain frequency bands, and capacitively loaded periodic lines are not only able to filter certain frequencies, but they also exhibit a slow wave effect useful for device miniaturization. However, the controllability of the dispersion diagram and Bloch impedance of EBG-based and capacitively loaded lines is very limited, as compared to that of artificial transmission lines that mimic effective medium metamaterials. These latter lines, consisting of host lines loaded with reactive elements (inductors, capacitors, resonators, or a combination of them) are usually referred to as metamaterial transmission lines, and become the aim of the present chapter. Despite the fact that metamaterial transmission lines are one-dimensional structures, effective parameters, such as the effective permeability and permittivity, can be defined (and tailored) in such lines, as will be shown later. However, rather than the permeability or permittivity, the interest in these lines is the controllability of the main line parameters, that is, the characteristic impedance and the phase constant (or dispersion). Thanks to this controllability (much superior than in conventional lines), RF/microwave devices with improved performance, or devices with novel functionalities can be implemented, as will be demonstrated in Chapter 4 (several RF/microwave applications of

[4] There are many papers focused on the implementation of invisibility cloaks. The author recommends the seminal paper by Smith and co-workers [1], where a realization at microwave frequencies is reported.

metamaterial transmission lines can also be found in general textbooks covering the topic of electromagnetic metamaterials [2–4]).

Although the first proposed metamaterial transmission lines were implemented by means of periodic structures with many periods [5–8], few cells (and even a single unit cell) sometimes suffice to achieve the required line specifications (this is interesting for device miniaturization) [9]. Therefore, in this book, the periodicity is not a requirement for the consideration of an artificial transmission line with controllable dispersion and characteristic impedance as a metamaterial transmission line. The key aspect is the superior controllability, as compared to conventional lines, of line parameters. If the metamaterial transmission line comprises many periods, the guided wavelength at the frequencies of interest is typically much longer than the unit cell dimensions, as required in effective medium metamaterials. However, if the number of cells is small, or if the artificial transmission line contains a single-unit cell, the long wavelength condition may not be satisfied at the frequencies of interest. In the context of this book, metamaterial transmission lines are artificial lines, consisting of a host line loaded with reactive elements, which allow for further control on phase constant and characteristic impedance, as compared to conventional lines. These lines are useful in the design of circuits based on dispersion and impedance engineering, as will be seen, and homogeneity and periodicity are not relevant [9]. For simplicity purposes, metamaterial transmission lines can be designated as *metalines* and the microwave circuits based on them as *metacircuits*.[5]

For completeness, we will also include in this book (Chapter 4) transmission lines loaded with metamaterial resonators, that is, electrically small resonators coupled to the lines, and formerly used for the implementation of effective medium metamaterials. Such lines are usually identified as transmission lines with metamaterial loading, and their functionality is based on particle resonance, rather than on dispersion and impedance engineering.[6] For this main reason, these lines are included in the next chapter, where several applications will be pointed out.

The chapter begins with a very short overview of effective medium metamaterials, with special emphasis on negative index and left-handed (LH) media, including their synthesis and EM properties. This introduction to negative index and LH media is convenient to properly understand the link between effective medium metamaterials and metamaterial transmission lines, and is of special interest to understand the origin of the so-called resonant-type metamaterial transmission lines [4, 8, 10] (exhaustively

[5] It is important to clarify that there are two- and three-dimensional effective media metamaterials implemented by extending the metamaterial transmission line concept to two and three dimensions. Such artificial structures are called transmission line metamaterials. Indeed, metamaterial transmission lines satisfying the periodicity and homogeneity condition are one-dimensional transmission line metamaterials, but not all the transmission line metamaterials are metamaterial transmission lines. In other words, the terms "metamaterial transmission line" (or metaline) and "transmission line metamaterial" are not pure synonymous.

[6] Notice that metamaterial transmission lines, that is, lines with controllable dispersion and characteristic impedance (above that achievable in conventional lines), can be implemented by means of metamaterial resonators loading the line. However, as long as the functionality of these lines is based on dispersion and impedance engineering, they are classified as metamaterial transmission lines (metalines), rather than as transmission lines with metamaterial loading.

studied in this chapter),[7] and other properties of metamaterial transmission lines as well. The chapter will continue with the introduction of the dual transmission line concept, as a ladder network consisting of a cascade of series capacitances and shunt connected inductances, that is, the dual counterpart of the lossless model of a conventional line. Although dual lines mimic the behavior of LH media (i.e., such lines support backward waves), in practice purely dual transmission lines are difficult (not to say impossible) to implement. As will be shown, these lines are implemented by loading a host line with series capacitors and shunt inductors, which means that at sufficiently high frequencies the line parameters are dominant and the structure behaves as a conventional line at these frequencies. Thus, the synthesis of artificial lines exhibiting backward wave propagation (i.e., LH lines) leads to metamaterial transmission lines actually exhibiting a composite right-/left-handed (CRLH) behavior [11], that is, backward wave propagation at low frequencies and forward (or right handed—RH) wave propagation at high frequencies. CRLH lines are the subject of an exhaustive analysis and study in this chapter. This includes the main CRLH line types, their properties, and their physical implementations. Since the applications of CRLH lines are very extensive and constitute an important part of this book, they are covered in a separate chapter (Chapter 4), together with the applications of transmission lines with metamaterial loading. Thus, Chapter 4, entirely focused on applications, has been mainly conceived as an independent chapter in order to avoid an excessively long Chapter 3. Other advanced artificial transmission lines are left for Chapter 6.

3.2 EFFECTIVE MEDIUM METAMATERIALS

The research activity in the field of metamaterials and their applications has experienced a significant growth since 2000, when the first effective medium metamaterial structure exhibiting negative permeability and permittivity simultaneously was fabricated and characterized [12]. This work and other subsequent works [13–15] confirmed some of the predictions of Veselago [16], made more than three decades before, relative to the properties of hypothetical media exhibiting a simultaneous negative value of the dielectric permittivity and magnetic permeability (such properties will be discussed later). Nowadays, it is accepted that *Metamaterials* constitute a transversal topic within science and technology, where disciplines as diverse as physics, chemistry, electromagnetism, electronics engineering, microwaves, photonics, optoelectronics, acoustics, micro/nanotechnology, and materials science, among others, and applications in fields such as sensors, medical diagnosis, security, antennas and radiofrequency identification (RFID), and so on, are involved. The increasing number of available books [2–4, 17–22], conferences, focused sessions, journal issues, and funded projects worldwide related to metamaterials is indicative of the high interest of these artificial structures in the past years, and many researchers, including the author of this book, refer to the

[7] Since resonant-type metamaterial transmission lines are exhaustively studied in this chapter, the analysis of several electrically small resonators useful for the synthesis of such lines and for the design of microwave circuits based on them, is also included.

exponential growth of the topic starting in 2000 as the "big bang" of *Metamaterials Science and Technology*. Key to this exponential growth was the physical implementation of artificial structures with unprecedented properties, derived from the simultaneous negative value of the effective permittivity and permeability. Such structures have been designated as double-negative (DNG) media [23], negative refractive index (NRI) media [24], backward media [25], Veselago media [26], or left-handed (LH) media [12, 16]. The latter term is the one which will be mainly used along this chapter, although some of the alternative designations will be occasionally used to highlight some medium properties linked to the term.

Although the LH structures (mainly due to their unique and controllable properties) are those artificial media that motivated the intensive research activity in the field of metamaterials from the beginning of the century, single negative (SNG) artificial structures were already pointed out before 2000. Indeed, structures consisting of parallel plates, waveguides, and metallic wires were presented as artificial plasmas scaled at microwave frequencies at the beginning of sixties by Rotman [27]. Since lossless plasmas exhibit a negative permittivity below the so-called plasma frequency, the work by Rotman and subsequent works [28, 29] opened the way to the design of artificial media with negative permittivity (such SNG media exhibiting negative permittivity have been called epsilon negative—ENG—structures). Artificial structures with negative permeability (also called mu negative—MNG—media), consisting of an array of split-ring resonators (SRRs), were also proposed in the late nineties by Pendry *et al.* [30]. However, SNG structures (either ENG or MNG) do also exist in natural form. Thus, low-loss plasmas and metals and semiconductors at optical and infrared frequencies exhibit a negative permittivity below the plasma frequency. Media with negative permeability are less common in nature due to the weak magnetic interaction in most solid state materials. Nevertheless, ferrites magnetized to saturation exhibit a tensor magnetic permeability with negative elements near the ferromagnetic resonance.[8] By contrast, DNG materials do not exist in natural form. The lack of naturally available DNG materials essentially means that the electrodynamics of media having simultaneously negative permittivity and permeability has been obviated for years. Nevertheless, notice that since the propagation constant of a plane wave is given by $k = \omega(\varepsilon\mu)^{1/2}$, a simultaneous change of sign in the permittivity and permeability does not make the medium opaque. In other words, LH media are transparent (provided the wave impedance of the DNG medium is not very different from that of the surrounding medium). However, with the exception of the seminal and meritorious work of Veselago [16], the electrodynamics, main properties, and limitations of DNG media were not an object of interest until 2000, when the physical implementation of LH media became a reality.

3.2.1 Wave Propagation in LH Media

Wave propagation in media with simultaneously negative permittivity and permeability was first analyzed and discussed by Veselago [16] at the end of 1960s, although it

[8] Ferrimagnetic materials are widely used in microwave engineering for the implementation of nonreciprocal devices, such as circulators.

was necessary to wait for more than 30 years to see the first practical realization of an LH medium [12]. In order to study wave propagation in LH media, let us first consider the wave equations (see Appendix A):

$$\nabla^2 \vec{E} + \omega^2 \mu \varepsilon \vec{E} = 0 \tag{3.1a}$$

$$\nabla^2 \vec{H} + \omega^2 \mu \varepsilon \vec{H} = 0 \tag{3.1b}$$

Since expressions (3.1) are not affected by a simultaneous change of sign in ε and μ, it is clear that low-loss LH media must be transparent. In fact, in view of equations (3.1), it can be erroneously concluded that solutions of (3.1) are invariant after a simultaneous change of the signs of ε and μ. However, when Maxwell's first-order differential equations are explicitly considered,

$$\nabla \times \vec{E} = -j\omega\mu \vec{H} \tag{3.2a}$$

$$\nabla \times \vec{H} = j\omega\varepsilon \vec{E} \tag{3.2b}$$

it follows that these solutions are quite different. In fact, for plane-wave fields of the form $\vec{E} = \vec{E}_o \exp\left(-j\vec{k}\cdot\vec{r} + j\omega t\right)$ and $\vec{H} = \vec{H}_o \exp\left(-j\vec{k}\cdot\vec{r} + j\omega t\right)$, the above equations become:

$$\vec{k} \times \vec{E} = \omega\mu \vec{H} \tag{3.3a}$$

$$\vec{k} \times \vec{H} = -\omega\varepsilon \vec{E} \tag{3.3b}$$

According to (3.3), for double-positive (DPS) index media (i.e., $\varepsilon > 0$ and $\mu > 0$), $\vec{E}$, $\vec{H}$, and $\vec{k}$ form a RH orthogonal system of vectors. However, for DNG media, expressions (3.3) rewrite as

$$\vec{k} \times \vec{E} = -\omega|\mu| \vec{H} \tag{3.4a}$$

$$\vec{k} \times \vec{H} = \omega|\varepsilon| \vec{E} \tag{3.4b}$$

and $\vec{E}$, $\vec{H}$ and $\vec{k}$ now form an LH triplet,[9] as illustrated in Figure 3.1. However, the direction of the time-averaged flux of energy, which is determined by the real part of the Poynting vector,

[9] For this reason, media with ε and μ simultaneously negative are called left-handed (LH) media [16]. In analogy, artificial media with ε and μ simultaneously positive (or even conventional dielectrics) can be designated as right-handed (RH) media, besides double-positive (DPS) media.

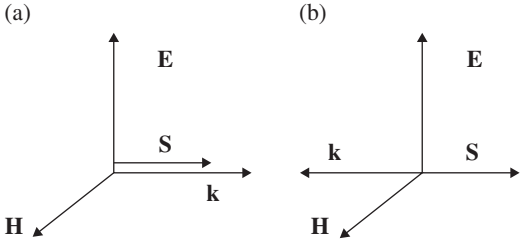

FIGURE 3.1 System of vectors $\vec{E}$, $\vec{H}$, $\vec{k}$, and $\vec{S}$ (depicted as bold symbols) for an ordinary (a) and a LH (b) medium. Reprinted with permission from Ref. [4]; copyright 2008 John Wiley.

$$\vec{S} = \frac{1}{2}\vec{E} \times \vec{H}^{*} \tag{3.5}$$

is unaffected by a simultaneous change of sign in ε and μ. This means that $\vec{E}$, $\vec{H}$, and $\vec{S}$ form a RH triplet in both types of media (DNG and DPS). Hence, in LH media, $\vec{S}$ and $\vec{k}$ are antiparallel, or, in other words, the direction of energy flow is opposite to the direction of the wave fronts in LH media. Thus, LH media support backward waves; and for this reason, the term *backward media* has also been proposed to designate such media. Nevertheless, the concept of backward waves to describe propagating waves with antiparallel phase and group velocities is not new. Such waves may appear in nonuniform waveguides and periodic structures, and also in the so-called backward-wave (or dual) transmission lines (as will be shown later) [31–33]. However, backward wave propagation in homogenous isotropic media seems to be a unique property of LH media, and the exotic EM properties of such media are intimately related to backward wave propagation, as will be seen in Section 3.2.3.

3.2.2 Losses and Dispersion in LH Media

So far, losses have been neglected in this chapter. In ordinary (RH) media, waves decay as they propagate since the energy is lost due to the effect of losses. However, in LH media, waves grow in the direction of propagation of the wavefronts (i.e., they decay in the direction of propagation of the energy). This result can be obtained, by considering that the real part of the permeability and permittivity are negative, as corresponds to LH media, whilst the imaginary parts are both negative, as results from the well-known complex Poynting theorem and energy conservation considerations [31, 34]. By considering a plane wave with square wave number

$$k^2 = \omega^2 \varepsilon \mu \tag{3.6}$$

it can be deduced that $\mathrm{Im}(k^2) > 0$ in LH media [4]. To demonstrate this, let us express k, ε and μ as

$$k = k' + jk'' \tag{3.7a}$$

$$\varepsilon = \varepsilon' - j\varepsilon'' \tag{3.7b}$$

$$\mu = \mu' - j\mu'' \tag{3.7c}$$

where the explicit negative sign in the imaginary part of ε and μ has been considered, namely, $\mathrm{Im}(\varepsilon) = -\varepsilon''$ and $\mathrm{Im}(\mu) = -\mu''$, ε'' and μ'' being positive quantities. Introducing (3.7) into (3.6), we obtain the following:

$$k'^2 - k''^2 + 2jk'k'' = \omega^2[\mu'\varepsilon' - \mu''\varepsilon'' - j(\mu'\varepsilon'' + \varepsilon'\mu'')] \tag{3.8}$$

From which it follows that $\mathrm{Im}(k^2) = 2k'k'' > 0$ if ε' and μ' are negative. Finally, if $\mathrm{Im}(k^2) > 0$, either

$$\mathrm{Re}(k) > 0 \quad \text{and} \quad \mathrm{Im}(k) > 0 \tag{3.9a}$$

or

$$\mathrm{Re}(k) < 0 \quad \text{and} \quad \mathrm{Im}(k) < 0 \tag{3.9b}$$

Notice that (3.9a) corresponds to a backward wave with the energy propagating in the negative direction, whereas (3.9b) corresponds to a backward wave with the energy propagating in the positive direction (according to the usual sign conventions).

An important consequence of the negative values of permittivity and permeability in LH media is that such media are inherently dispersive. Indeed, if negative values of ε and μ are introduced in the usual expression for the time-averaged density of energy in transparent nondispersive media, U_{nd}, given by

$$U_{\mathrm{nd}} = \frac{1}{4}\left(\varepsilon\left|\vec{E}\right|^2 + \mu\left|\vec{H}\right|^2\right) \tag{3.10}$$

a negative density of energy is obtained, which is a nonphysical result. Inspite that any physical media other than vacuum must be dispersive, expression (3.10) can be used as long as the considered medium is weakly dispersive (as occurs in many different cases). The correct expression for the density of energy in the general case (dispersive and nondispersive media) is [35]:

$$U = \frac{1}{4}\left(\frac{\partial(\omega\varepsilon)}{\partial\omega}\left|\vec{E}\right|^2 + \frac{\partial(\omega\mu)}{\partial\omega}\left|\vec{H}\right|^2\right) \tag{3.11}$$

From (3.11), the requirement of positive energy density gives

$$\frac{\partial(\omega\varepsilon)}{\partial\omega} > 0 \quad \text{and} \quad \frac{\partial(\omega\mu)}{\partial\omega} > 0 \tag{3.12}$$

which is compatible with $\varepsilon < 0$ and $\mu < 0$ provided $\partial\varepsilon/\partial\omega > |\varepsilon|/\omega$ and $\partial\mu/\partial\omega > |\mu|/\omega$. This means that any physical implementation of an LH medium must be highly dispersive, in agreement with the low-loss Drude–Lorenz model for ε and μ, which provides negative values for ε and/or μ in the highly dispersive regions, just above the resonances [36].

From the inequalities (3.12), it can also be deduced that the phase and group velocities are of opposite sign in LH media. Namely,

$$\frac{\partial k^2}{\partial\omega} = 2k\frac{\partial k}{\partial\omega} = 2\frac{\omega}{v_p v_g} \tag{3.13}$$

where $v_p = \omega/k$ and $v_g = \partial\omega/\partial k$ are the phase and group velocities, respectively. From (3.6) and (3.12), the following inequality results:

$$\frac{\partial k^2}{\partial\omega} = \omega\mu\frac{\partial(\omega\varepsilon)}{\partial\omega} + \omega\varepsilon\frac{\partial(\omega\mu)}{\partial\omega} < 0 \tag{3.14}$$

provided $\varepsilon < 0$ and $\mu < 0$. Therefore, from (3.13) it is apparent that v_p and v_g have opposite signs, that is, wavepackets and wavefronts travel in opposite directions in LH media.

3.2.3 Main Electromagnetic Properties of LH Metamaterials

Besides backward wave propagation, LH media exhibit further unusual properties, such as a negative refractive index [13, 37–42], subwavelength resolution and focusing [43, 44],[10] inverse Doppler effect, backward Cerenkov radiation [45], and negative Goos–Hänchen shift [46–50], among others. Except backward wave propagation and backward Cerenkov radiation (intimately related to backward leaky wave radiation in LH and CRLH transmission lines), the other exotic properties of LH media are of interest in bulk two-dimensional or three-dimensional metamaterials, rather than in metamaterial transmission lines. Therefore, only the implications of backward wave propagation in LH media relative to negative refraction[11] and backward Cerenkov

[10] The topic of subwavelength resolution and focusing has been an object of an intensive research in the recent years. A complete list of references would be too long for inclusion in a book focused on artificial transmission lines. Therefore, only the seminal work by J.B. Pendry [43] and a recent paper that includes many references on the topic [44] are cited for those readers willing to be introduced in the field.

[11] Although negative refraction is not of interest for metamaterial transmission lines, this topic is succinctly considered in this book since the negative refractive index is probably the most genuine characteristic of an LH medium, and it has been the subject of an intensive research activity, both theoretical and experimental. Moreover, negative refractive index materials realized by extending the metamaterial transmission line concept to two- and three dimensions (2D and 3D transmission line metamaterials) have been proposed.

radiation are considered in this textbook. An exhaustive analysis of the other physical effects derived from backward wave propagation in LH media can be found in the references given earlier, in the seminal paper of Veselago [16], or in several books related to metamaterials (see, e.g., Refs [4, 20]).

3.2.3.1 Negative Refraction In the refraction of an incident beam at the interface between an ordinary material and an LH medium, boundary conditions impose continuity of the tangential components of the wavevector along the interface. Hence, due to backward wave propagation in the LH region, it follows that, unlike in ordinary refraction, the angles of incidence and refraction have opposite signs; or in other words, the incident and refracted beams lie at the same side of the normal, as Figure 3.2 illustrates. From the aforementioned continuity of the tangential components of the wavevectors of the incident and refracted beams, it follows that (Fig. 3.2)

$$\frac{\sin\theta_1}{\sin\theta_2} = \frac{-|k_2|}{k_1} = \frac{n_2}{n_1} < 0 \tag{3.15}$$

which is the well-known Snell's law. In this expression, n_1 and n_2 are the refractive indices of the ordinary and LH media, respectively, given by $n^2 = c^2\varepsilon\mu$. Assuming $n_1 > 0$, from Equation 3.15 it follows that $n_2 < 0$. That is, the sign of the square root in the refractive index definition must be chosen to be negative [16]:

$$n = -c\sqrt{\varepsilon\mu} < 0 \tag{3.16}$$

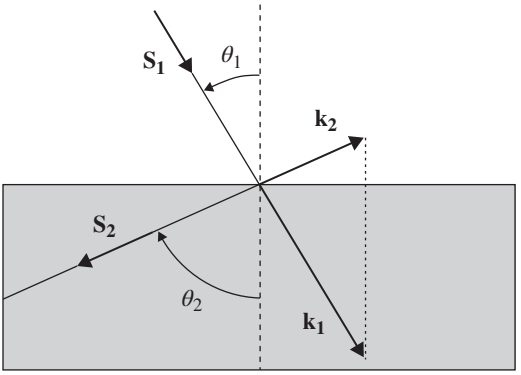

FIGURE 3.2 Graphic illustrating the negative refraction between an ordinary (subscript 1, top) and LH (subscript 2, gray region) medium. Poynting and wavevectors for each medium are labeled as $\vec{S}_1$, $\vec{S}_2$, $\vec{k}_1$, and $\vec{k}_2$, respectively, and depicted as bold symbols in the figure. Negative refraction arises from the continuity of the components of the wavevectors, $\vec{k}_1$ and $\vec{k}_2$, parallel to the interface. The beams propagate along the direction of energy flow, that is, they are parallel to the Poynting vectors. Reprinted with permission from Ref. [4]; copyright 2008 John Wiley.

For this reason, LH media are also referred to as *negative refractive index* (NRI) or *negative refractive* media.

It is important to mention, however, that negative refraction is not exclusive of NRI materials. For instance, it can be achieved at the interface between an ordinary isotropic medium and a hypothetical uniaxial medium with $\varepsilon_\perp > \varepsilon_\parallel$ for very specific angles of incidence and polarization [4], and negative refraction has been demonstrated in PCs [51–53] as well. Thus, the interface between an NRI metamaterial and an ordinary medium exhibits negative refraction, but such unusual effect can be achieved by other means. Light or (more generally) EM radiation bending can be achieved and controlled in anisotropic artificial structures. On the basis of transformation optics, such structures can be engineered in order to exhibit cloaking effects (see, e.g., Ref. [54] and references therein).

3.2.3.2 Backward Cerenkov Radiation Cerenkov radiation is emitted when a charged particle (i.e., an electron) passes through a dielectric medium at a speed, v, greater than the phase velocity of light in that medium (c/n). As the charged particle travels, electrons in the atoms of the medium are displaced, the atoms become polarized, and, to restore equilibrium, photons are emitted. If the particle motion is slow, as compared to the velocity of light in the medium, these photons destructively interfere with each other, and no radiation is detected. Conversely, if the charged particle travels faster than light in the medium the emitted radiation forms a shock wave, similar to the sonic shock waves generated in a supersonic aircraft. This situation is illustrated in Figure 3.3a, where it can be appreciated that the spherical wavefronts radiated by the particles are delayed with regard to the particle motion, with the result of forward Cerenkov radiation. From Figure 3.3a, the radiation angle is given by

$$\cos\theta = \frac{c}{nv} \tag{3.17}$$

In the illustration of Figure 3.3a, it is assumed that the medium surrounding the charged particle is an ordinary medium. Let us now consider that the surrounding medium is LH. Since wave propagation is backward, the spherical wavefronts move inward to the source with velocity $c/|n(\omega)|$, where $n(\omega) < 0$ and the frequency dependence has been explicitly introduced in n to highlight the dispersive nature of the LH medium.[12] Therefore, each wavefront collapses at advanced positions of the particle, as Figure 3.3b illustrates, and the resulting shock wave travels backward forming an obtuse angle with the trajectory of the particle. This angle is given by (3.17) with n replaced with $-|n(\omega)|$.

At this point, it is important to mention that there are similarities between Cerenkov radiation and leaky wave radiation in periodic structures. It was argued in Section 2.2 that open periodic structures may radiate at those frequency regions where the phase velocity of the guided waves, v_p, is higher than the speed of light in vacuum, c,

[12] Since the particle radiates in a broad spectral range, the Cerenkov radiation spectra must exhibit forward and backward wave radiation [45].

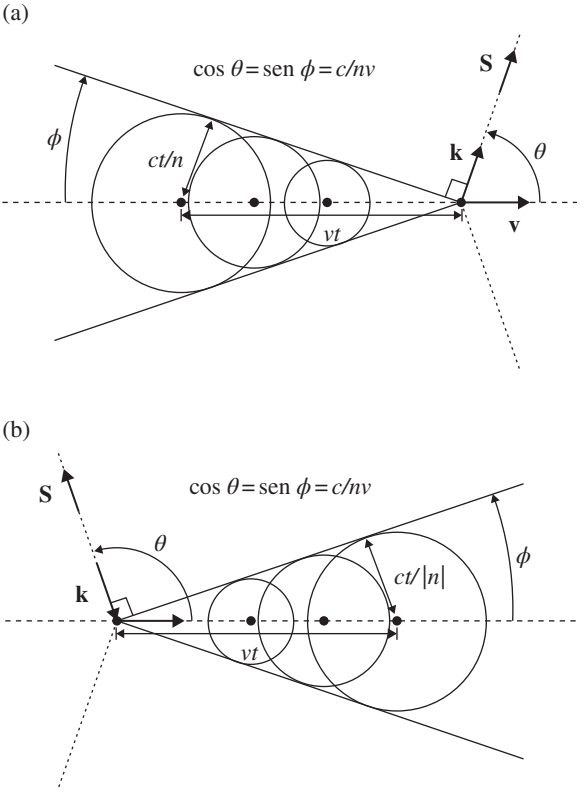

FIGURE 3.3 Illustration of the formation of Cerenkov shock waves in an ordinary medium (a), and in an LH medium (b). In (a), the spherical wavefronts move outward from the source at a velocity c/n; whereas in (b), the spherical wavefronts move inward to the source at a velocity $c/|n(\omega)|$. Reprinted with permission from Ref. [4]; copyright 2008 John Wiley.

(fast-wave regions).[13] This phenomenon can be interpreted in terms of coupling, or energy transfer, between the guided waves and the radiated (leaky) waves. If $v_p > c$ (or c/n in a medium different than vacuum or air), the guided mode can be coupled to a free space (leaky) mode since the wavevector $\vec{k}$ of the space harmonic has a real transversal component, k_{tn}, giving rise to a leaky wave with wavevector $\vec{k}$, as Figure 2.3 illustrates. The Cerenkov radiation can be interpreted in a similar fashion in terms of wave coupling. For superluminal charged particles ($v > c/n$), the fields generated in the transverse direction are responsible for particle radiation since they do not decay, and this can be explained by the real transverse component of the charge wavevector under these conditions. Such coupling can be seen as a conversion

[13] It was assumed in Section 2.2 that the open periodic structure is surrounded by vacuum (or air). However, the analysis of leaky wave radiation in such structures can be generalized to any surrounding medium by simply replacing c with c/n.

between kinetic energy and radiated power. Notice also that (3.17) is equivalent to (2.11), and that these expressions are valid for both forward and backward wave radiation. However, backward Cerenkov radiation occurs because the surrounding medium is LH, whereas backward leaky wave radiation of the space harmonics in periodic structures in certain frequency regions is caused by the backward wave nature of the propagating waves in those regions (the surrounding medium being typically air). For backward Cerenkov radiation, the diagram of Figure 2.3a applies, corresponding to a positive wavevector for the charged particle in the direction of motion. However, notice that since the Poynting vector is in opposite direction to the wavevector, backward wave radiation arises. Forward and backward leaky wave radiation in CRLH transmission lines will be considered in Chapter 4. The phenomenology is essentially the same than leaky wave radiation in periodic structures, although leaky CRLH transmission lines radiate in the fundamental mode.

3.2.4 Synthesis of LH Metamaterials

In this section, the synthesis of the first bulk LH medium, consisting of a combination of metallic posts and split-ring resonators (SRRs) [12], is briefly reviewed, and the SRR is analyzed in certain detail. This will help to understand the origin of the first LH (actually CRLH) transmission line implementation based on SRRs [8], that mimics the one-dimensional medium reported in Ref. [12][14] and constitutes the basis of a set of artificial transmission lines based on the resonant-type approach (such lines and other metamaterial transmission lines will be analyzed in Section 3.5). A complete review of the different reported approaches for the implementation of LH and other artificial media, including two- and three-dimensional structures, would be too long for inclusion in this book. Nevertheless, it is important to mention that implementations of two- and three-dimensional metamaterials based on SRRs [13, 55, 56], as well as structures fabricated by extending the metamaterial transmission line concept to two and three dimensions [57–65], have been reported. It is also worth mentioning that one of the most promising approaches for the synthesis of NRI metamaterials at quasioptical or optical frequencies is based on fishnet structures, which can be implemented by means of micro/nanofabrication technologies (see Ref. [66] and references therein). A recent review of 3D photonic metamaterials can be found in Ref. [67].

The one-dimensional LH structure reported in Ref. [12] consists of a combination of metallic posts (or wires) and SRRs (Fig. 3.4). The structure supports backward waves in a narrow band above SRR resonance (where the effective permittivity and permeability are simultaneously negative) for incident radiation polarized with the electric field parallel to the wires and the magnetic field axial to the SRRs. The metallic wires and SRRs are responsible for the negative effective permittivity and permeability, respectively.

[14] Although the structure reported in Ref. [12] is a bulk LH medium, it is actually a one-dimensional metamaterial, since backward wave propagation occurs only in one direction of propagation and for a specific polarization conditions.

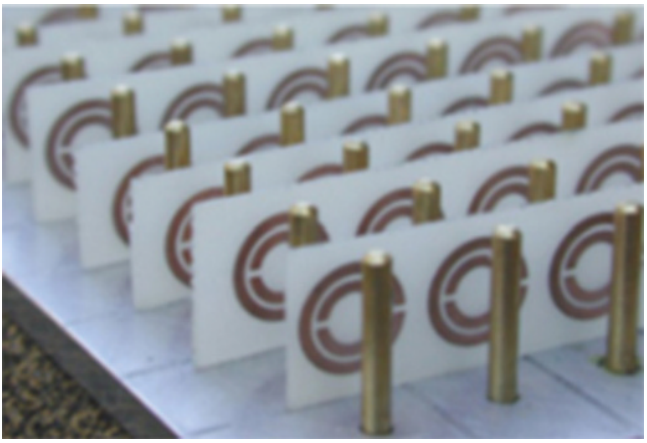

FIGURE 3.4 First synthesized one-dimensional bulk LH metamaterial. Photo courtesy by D.R. Smith.

3.2.4.1 Negative Effective Permittivity Media: Wire Media Let us first consider a square lattice of metallic wires without SRRs for incident plane waves polarized with the electric field parallel to the wires (Fig. 3.5a). Let l and r be the distance between wires and wire radius, respectively. This system can be modeled by a TEM transmission line loaded with metallic posts, as depicted in Figure 3.5b, which in turn can be described by the lumped-element circuit model of Figure 3.5c, where the per-section series inductance and shunt capacitance of the TEM line are $L_s = \mu_o l$ and $C_s = \varepsilon_o l$, respectively, and the shunt inductance of the metallic wires is [4, 28]

$$L = \frac{\mu_o l}{2\pi} \ln\left(\frac{l}{r}\right) \tag{3.18}$$

The dispersion of this periodic structure can be inferred by means of (2.33), with $Z_s(\omega) = j\omega L_s$ and $Z_p(\omega) = Y_p{}^{-1}(\omega) = [j\omega C_s + 1/(j\omega L)]^{-1}$, giving:

$$\cos(kl) = 1 - \frac{1}{2} L_s C_s \omega^2 \left(1 - \frac{1}{LC_s\omega^2}\right) \tag{3.19}$$

In the long wavelength limit ($kl \to 0$), $\cos(kl) \cong 1 - (kl)^2/2$, and the wavenumber (or phase constant) is found to be

$$k^2 = k_o^2 \left(1 - \frac{2\pi}{\mu_o \varepsilon_o l^2 \omega^2 \ln(l/r)}\right) \tag{3.20}$$

where $k_o^2 = \mu_o \varepsilon_o \omega^2$ is the free space wavenumber. The dispersion relation given by (3.20) is identical to that of an ideal plasma, provided the cutoff frequency is

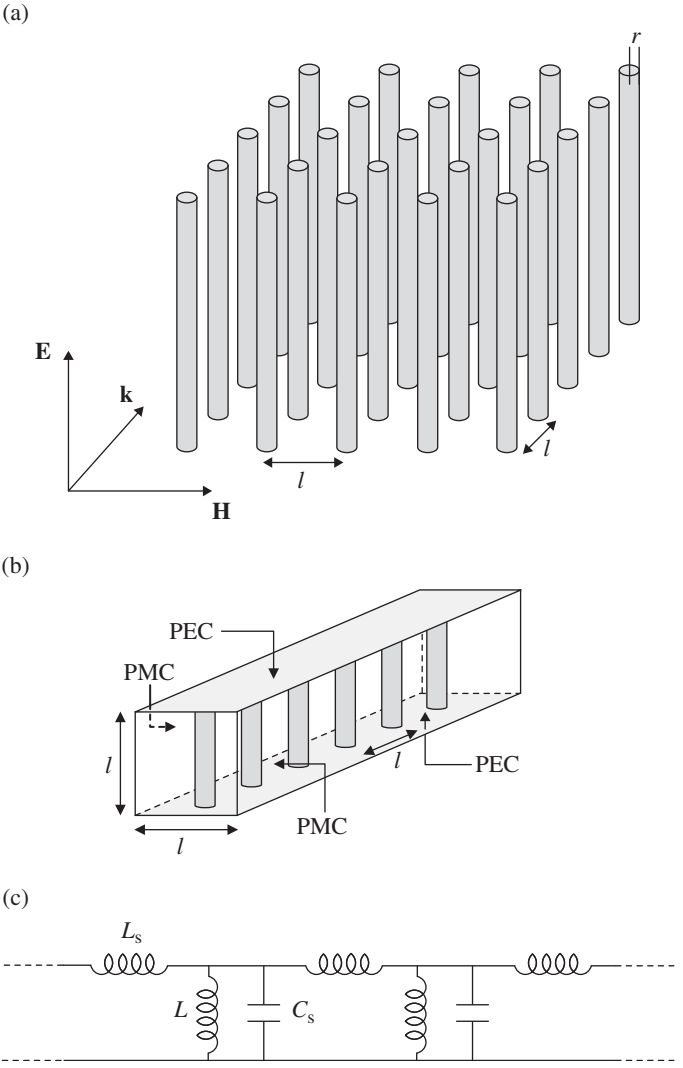

FIGURE 3.5 Artificial wire medium exhibiting negative effective permittivity for incident radiation with the electric field parallel to the wires (a), equivalent structure consisting of a post-loaded TEM transmission line (b), and equivalent circuit model of the transmission line (c). PMC and PEC stand for perfect magnetic and perfect electric conductor, respectively.

substituted by the plasma frequency. Thus the system of wires, for the considered polarization conditions, behaves as an ideal plasma, with plasma frequency:

$$\omega_p^2 = \frac{2\pi}{\mu_o \varepsilon_o l^2 \ln(l/r)} \tag{3.21}$$

and effective permittivity given by

$$\varepsilon_{\text{eff}} = \varepsilon_{\text{o}} \left(1 - \frac{\omega_{\text{p}}^2}{\omega^2} \right) \tag{3.22}$$

being negative for frequencies below ω_{p}. An equivalent expression to (3.21) was derived by Solymar and Shamonina in their textbook [21], by considering the current induced in the wires by the external electric field. It has also been demonstrated that a cubic mesh of metallic wires behaves as an isotropic artificial plasma for all wave polarizations and propagation directions [4].

The expression of the effective permittivity is said to correspond to the Drude model, which is a particular case of the well-known Lorentz model of materials that results when the restoring force is negligible. To gain insight on this, let us assume that an electric field is applied to a certain material. The motion of the electrons is derived from the Newton's second law, giving for the most general case the equation of a forced and damped oscillator, that is,

$$m \frac{d^2 \vec{x}}{dt^2} = e \vec{E} - k_{\text{r}} \vec{x} - m\Gamma \frac{d\vec{x}}{dt} \tag{3.23}$$

where e and m are the electron charge and mass, respectively, $\vec{E}$ is the applied electric field, k_{r} is the proportionality constant between the restoring force and displacement (it is assumed that the attractive force of bounded electrons in atoms has a linear dependence on $\vec{x}$), and Γ is a damping factor that accounts for losses. The solution of (3.23), assuming harmonic type time dependence, is

$$\vec{x} = \frac{e}{m\left(\omega_{\text{o}}^2 - \omega^2 + j\Gamma\omega\right)} \vec{E} \tag{3.24}$$

where $\omega_{\text{o}}^2 = k/m$. If N is the density of electrons, the polarization induced by $\vec{E}$ is simply $\vec{P} = Ne\ \vec{x}$.[15] Since the polarization is related to the external field by the electric susceptibility, χ_{e}, that is, $\vec{P} = \varepsilon_{\text{o}} \chi_{\text{e}}\ \vec{E}$, it follows that the permittivity of the medium $\varepsilon = \varepsilon_{\text{o}}(1 + \chi_{\text{e}})$ is (Lorentz model):

$$\varepsilon = \varepsilon_{\text{o}} \left(1 + \frac{\omega_{\text{p}}^2}{\left(\omega_{\text{o}}^2 - \omega^2 + j\Gamma\omega\right)} \right) \tag{3.25}$$

[15] The polarization is defined as the density of electric dipole moments. Since the electric dipole moment of two point charges separated a distance $\vec{x}$ is $\vec{p} = e\ \vec{x}$, the aforementioned expression for the polarization is obtained.

with

$$\omega_p^2 = \frac{Ne^2}{\varepsilon_o m} \tag{3.26}$$

For free electrons in metals, the restoring force is zero ($\omega_o = 0$), and the Drude model results, that is,

$$\varepsilon = \varepsilon_o \left(1 - \frac{\omega_p^2}{(\omega^2 - j\Gamma\omega)} \right) \tag{3.27}$$

where the real part of the dielectric permittivity is found to be negative for frequencies satisfying $\omega^2 < \omega_p{}^2 - \Gamma^2$. If losses are neglected ($\Gamma = 0$), expression (3.22) results, and the dielectric permittivity is negative below the plasma frequency. It should be mentioned, however, that losses are always present in metals, and therefore (3.27) must be applied. At low frequencies, the real part of the permittivity is negative, but the imaginary part is very large and becomes dominant. Under these conditions, the conduction current dominates over the displacement current, and dispersion is dictated by (1.78). From a physical viewpoint, in the low-frequency regime, electron motion in metals is dictated by continuous dissipative collisions and the plasma-like behavior is not manifested. Conversely, near the plasma frequency, the amplitude of the collective electron oscillations generated by the applied electric field is small as compared to the electron mean free path, and the metal exhibits the plasma-like behavior. Notice that the main difference between the Drude and Lorentz models concerns the bandwidth of the frequency region where the real part of the dielectric permittivity is negative. The Lorentz model predicts a negative dielectric permittivity in a narrow band just above the resonance frequency ω_o.

In ordinary dielectric materials, electrons are bounded to atoms and the restoring force and damping dominate over the acceleration of the charges. Under these conditions, the solution of (3.23) gives a dielectric permittivity of the form

$$\varepsilon = \varepsilon_o \left(1 + \frac{\omega_p^2}{(\omega_o^2 + j\Gamma\omega)} \right) \tag{3.28}$$

corresponding to the Debye model of materials.

Notice that, in the previous analysis, the dielectric permittivity has been considered a scalar and the considered material has been assumed to be isotropic. However, many materials exhibit anisotropy (or even bianisotropy—a concept introduced later), and the permittivity is a tensor, rather than a scalar. Indeed, the one-dimensional wire media discussed before (described by the post-loaded TEM line of Fig. 3.5) and many other artificial media are highly anisotropic. In particular, the analyzed wire structure is an ENG medium only for incident radiation polarized with the electric field parallel to the wires.

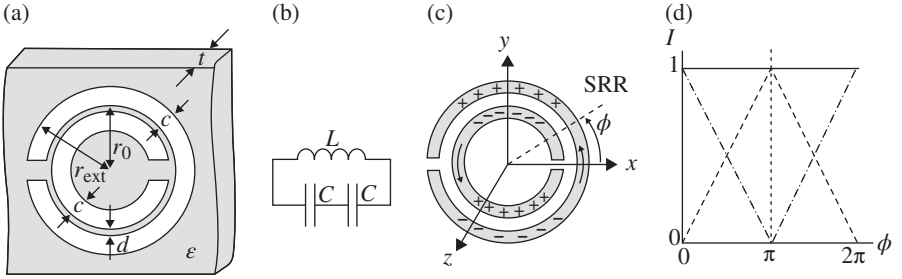

FIGURE 3.6 Topology of the SRR and relevant dimensions (a), equivalent circuit model (b), distribution of charges at the fundamental resonance (c), and plot of the angular dependence of the currents for the inner (dashed line) and outer (dash-dotted line) ring (d). The current flows in the same direction in both rings for the fundamental resonance, and the sum of the currents of both rings is uniform along the whole circumference [4]. Notice that the symmetry plane (*x*-*z* plane) is an electric wall. The metallization in (a) is indicated in white. Reprinted with permission from Ref. [4]; copyright 2008 John Wiley.

3.2.4.2 Negative Effective Permeability Media: SRRs Unlike dielectric materials, magnetic materials (i.e., materials exhibiting magnetic activity) are less common. In particular, except ferrites at certain frequencies, negative permeability materials (MNG) are not available in nature. The implementation of artificial media with negative permeability is of interest not only for the synthesis of LH media but also because the magnetic response of most materials tails off in the GHz range. In principle, a set of conducting rings (all of them with the axis oriented in the same direction) could be a good candidate for the realization of a negative permeability medium for EM radiation polarized with the magnetic field parallel to the rings axis. The time-varying magnetic field induces circulating currents in the rings, which in turn generate a secondary magnetic flux opposite to that created by the external field. The magnetic polarizability of a conducting ring is thus negative, providing a negative dipole moment, and hence a negative magnetic susceptibility for the set of rings. However, this diamagnetic behavior is not strong enough to generate negative permeability (a detailed justification is given in Ref. [4]).

The magnetic polarizability of a closed metallic ring can be enhanced by loading the loop with a capacitor [68], or by any other means providing a resonant behavior. In particular, Pendry *et al*. [30] proposed the topology depicted in Figure 3.6a, known as split-ring resonator (SRR). The SRR can be implemented in fully planar technology, yet achieving small electrical sizes[16] on account of the distributed capacitance of the particle. Above the resonance frequency of the SRR, a strong diamagnetic behavior is expected for the external magnetic field polarized in the axial direction; hence, an

[16] The electrical size of the SRR is usually given by its diameter expressed in terms of the free space wavelength at resonance. Alternatively, if the SRR loads a transmission line (as will be later considered), the electrical size can be expressed in terms of the guided wavelength at resonance.

array of SRRs is expected to exhibit a negative effective permeability in a certain band of frequencies, under these polarization conditions. A detailed demonstration of this is given in Refs. [4, 68]. Nevertheless, a simplified analysis is provided in the next paragraphs for completeness.

When a time-varying magnetic field is applied to the axial direction (z-direction), current loops are induced in the rings, and current flows from one ring to the other through the distributed (edge) capacitances between the rings. As long as both rings are very close one each other, the edge capacitance is significant, resulting in considerable coupling between both rings. Under these conditions, a quasistatic analysis applies, and the SRR can be modeled by the circuit depicted in Figure 3.6b, where L is the SRR self-inductance and C is the edge capacitance corresponding to each SRR half. This capacitance is $C = \pi r_o C_{pul}$, where r_o is the mean radius of the SRR ($r_o = r_{ext} - c - d/2$), and C_{pul} is the per-unit-length capacitance along the slot between the rings. The self-inductance can be calculated as the inductance of a single closed loop with identical width to that of the individual rings (c), and mean radius (r_o) [69]. Quasianalytical expressions for L and C_{pul} are given in Ref. [4] (in particular, C_{pul} is inferred from formulas extracted from Ref. [70]). The fundamental resonance frequency of the SRR is thus:

$$\omega_o = \sqrt{\frac{2}{LC}} = \sqrt{\frac{2}{L\pi r_o C_{pul}}} \tag{3.29}$$

Let us assume that the SRR is excited by an external axial magnetic field that generates a magnetic flux, $\Phi_{ext} = \pi r_o^2 B_z^{ext}$, across the SRR. The induced current in the SRR can be expressed as follows:

$$I = -j\omega\Phi_{ext}\left(\frac{2}{j\omega C} + j\omega L\right)^{-1} \tag{3.30}$$

Since the induced dipolar magnetic moment is given by $m_z = \pi r_o^2 I$, and it is related to the magnetic polarizability by $m_z = \alpha B_z^{ext}$, it follows that the magnetic polarizability is[17]

$$\alpha = \frac{\pi^2 r_o^4}{L}\left(\frac{\omega_o^2}{\omega^2} - 1\right)^{-1} \tag{3.31}$$

[17] In Ref. [4], the magnetic polarizability given by expression (3.31) is designated as α_{zz}^{mm}, where the double subindex zz indicates that it is due to a force directed along the z-axis, and produces an effect along the same axis, and the double superindex mm indicates that the external force is magnetic, and that the effect is also magnetic. The reason for such nomenclature is that the SRR exhibits further polarizabilities, including a resonant-type electric polarizability along the y-axis, and resonant cross-polarizabilities. Such polarizabilities are not considered in this book (the expressions for such polarizabilities can be found in Ref. [4]).

and it experiences a strong variation from highly positive to highly negative values at the resonance frequency of the SRR.

In the previous analysis, losses have been neglected. However, a more realistic picture of the SRR must include ohmic losses. It can be easily demonstrated that the polarizability of the SRR, including the effects of losses through the AC resistance, R, of the SRR, is [4]

$$\alpha = \frac{\pi^2 r_o^4}{L}\left(\frac{\omega^2}{\omega_o^2 - \omega^2 + j\omega\Gamma}\right) \tag{3.32}$$

where $\Gamma = R/L$.

Once the magnetic polarizability has been inferred, the magnetic susceptibility is calculated, to a first-order approximation,[18] as $\chi_m = \mu_o\alpha/a^3$, and the effective permeability is [4]:

$$\mu_{eff} = \mu_o(1+\chi_m) = \mu_o\left(1 + \frac{\mu_o\pi^2 r_o^4}{a^3 L}\left(\frac{\omega^2}{\omega_o^2 - \omega^2 + j\omega\Gamma}\right)\right) \tag{3.33}$$

where a cubic lattice SRR structure with unit cell volume given by a^3 has been considered (Fig. 3.7). Expression (3.33) can be written in a more compact form as follows:

$$\mu_{eff} = \mu_o\left(1 - \frac{F\omega^2}{\omega^2 - \omega_o^2 - j\omega\Gamma}\right) \tag{3.34}$$

where F is a dimensionless factor less than 1[19] given by

$$F = \frac{\mu_o\pi^2 r_o^4}{a^3 L} \tag{3.35}$$

If we assume that losses are very small, the magnetic permeability is negative in the range $\omega_o < \omega < \omega_o/(1-F)^{1/2}$, that is, in a narrow band. The expression for the effective permeability given by (3.34), corresponding to the Lorentz model, is identical to the one reported by Shamonina and Solymar [21], and very similar to the one reported by Pendry *et al*. [30].

Notice that (3.34) gives the effective magnetic permeability of the structure of Figure 3.7 in the z-direction. Actually, the structure of Figure 3.7 is bianisotropic, that is, it exhibits cross polarizabilities, and the constitutive relationships are characterized by electric, magnetic, and magnetoelectric susceptibility tensors [4]. However, for the

[18] This approximation ignores the coupling between adjacent SRRs (more accurate expressions are given in Refs. [4, 21]).

[19] The reason is that $a^2 > \pi r_o^2$ and L is significantly larger than $\mu_o r_o$ [69] for reasonable values of c and r_o (a justification of this for a cylindrical ring can be found in Ref. [4]).

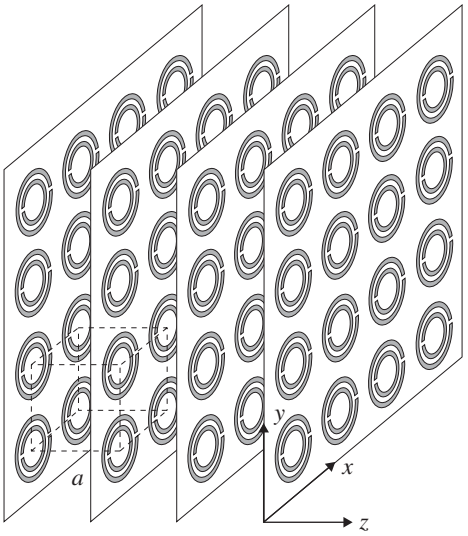

FIGURE 3.7 MNG artificial medium made of a cubic lattice of SRRs for incident radiation with the magnetic field polarized in the z-direction. Reprinted with permission from Ref. [4]; copyright 2008 John Wiley.

purposes of this book, the previous analysis suffices. Nevertheless, it is worth mentioning that the SRR exhibits also an electric dipole moment in the plane of the particle (y-direction), as can be seen from the distribution of charges in the rings (Fig. 3.6c). This means that the SRR can be driven by a time-varying electric field applied in the y-direction as well. In other words, the magnetic and the electric dipole moments of the particle can be induced by either an electric or a magnetic field (applied in the convenient direction). The fact that the SRR exhibits magnetoelectric coupling has implications for the implementation and modeling of metamaterial transmission lines based on these particles, as will be discussed later.

3.2.4.3 Combining SRRs and Metallic Wires: One-Dimensional LH Medium

The first one-dimensional LH artificial structure, designed by Smith and co-workers (Fig. 3.4), was implemented by combining the wire and SRR media discussed in the previous sections [12]. The superposition hypothesis that the combination of an ENG and an MNG medium gives an LH medium was assumed. However, such hypothesis is not in general justified, and the implementation of an LH medium by combining SRRs and wires (or posts) requires the consideration of the possible interactions between the constitutive elements. In particular, in the medium reported by Smith (Fig. 3.4), caution was taken to avoid the potential influence of the SRRs on the inductance of the posts by alternating the planes containing the wires and the SRRs (further details on the superposition principle are given in Refs. [4, 71, 72]).

The structure of Figure 3.4 was illuminated with a plane wave polarized with the electric and magnetic field directed toward the post and SRR axis, respectively, and a

bandpass response was obtained in a narrow band, just above the SRR resonance frequency (Fig. 3.8a). It was also demonstrated that by removing the metallic posts, a stop band behavior results (Fig. 3.8a). Such stop band was attributed to the negative effective permeability of the SRR medium. However, by incorporating the posts, the

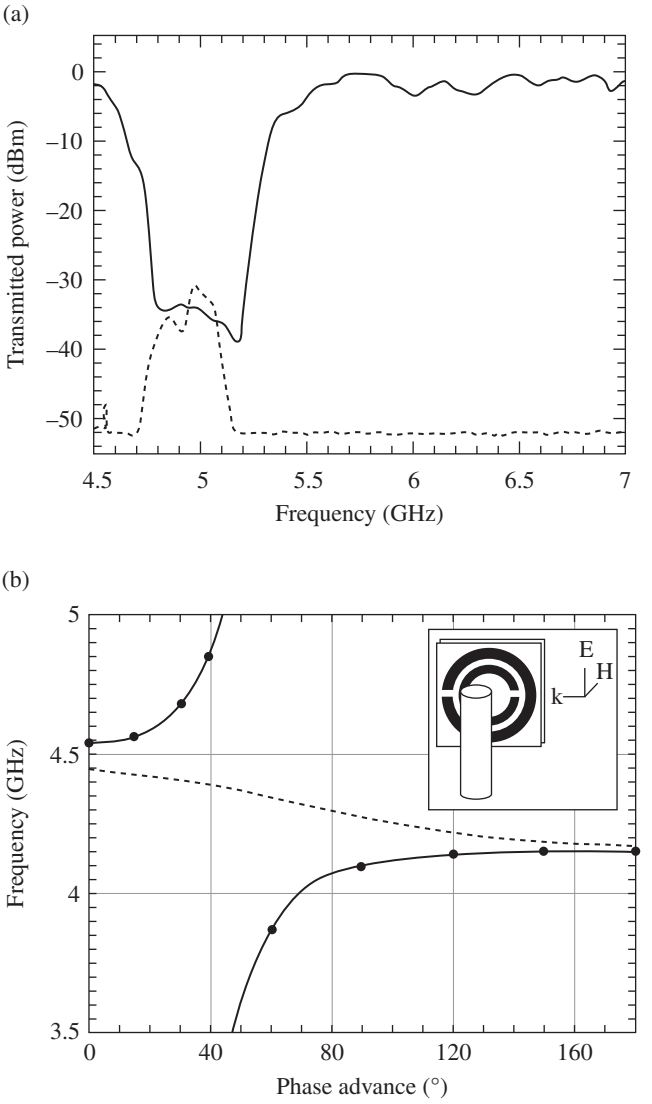

FIGURE 3.8 (a) Transmitted power for the structure of Figure 3.4 (dashed line) and for the structure without metallic posts (solid line); (b) dispersion relation. The polarization conditions are explained in the text, and the details of the experiment are given in Ref. [12]. Reprinted with permission from Ref. [12]; copyright 2000 American Physical Society.

SRRs are embedded in a negative permittivity medium with plasma frequency above the SRR resonance frequency (12 GHz approximately). Therefore, the composite medium exhibits LH wave propagation in the region of negative permeability, where the effective permittivity is also negative. Outside that band, the structure is an opaque ENG medium and the transmitted power is attenuated to below the noise floor. The small power transmission in the LH pass band can be mainly attributed to a significant mismatch between the composite medium and air. The LH behavior of the composite SRR-wire structure was confirmed through the dispersion relation, inferred from a commercial EM mode solver [12]. The results, depicted in Figure 3.8b, indicate that the phase and group velocities have different sign in the pass band region (dashed line between 4.15 GHz and 4.45 GHz), as one expects in a LH medium. The dispersion relation corresponding to the SRR medium without wires, also included in Figure 3.8b as bold line, points out that wave propagation in the allowed regions is forward, and that the stop band (associated to the negative effective permeability) roughly coincides with the LH band of the composite SRR-wire medium.

It is noticeable that an LH medium was also achieved by introducing a row of SRRs inside a rectangular metallic waveguide (along its middle E-plane) designed to exhibit its cutoff frequency above the SRR fundamental resonance frequency [73]. In such structure, the negative permittivity (for the fundamental TE_{10} mode) is provided by the cutoff waveguide, whereas the negative permeability is due to the SRRs. Indeed the dispersion relation of such medium is formally identical to that of the SRR-wire media, which can be inferred from (3.6) replacing ε and μ with ε_{eff} and μ_{eff}, respectively. To end this subsection, let us point out that the equivalence between a rectangular waveguide and a dielectric plasma, valid for evanescent TE modes, has a dual counterpart for magnetic plasmas and evanescent TM modes. Namely, an MNG medium can be simulated by means of TM modes below their cutoff frequencies. Using this concept, a DNG medium, consisting of a square waveguide filled with a transverse two-dimensional array of thin metallic wires, for evanescent TM modes, has been proposed [74].

3.3 ELECTRICALLY SMALL RESONATORS FOR METAMATERIALS AND MICROWAVE CIRCUIT DESIGN

The aim of this section is to analyze several resonator topologies for the synthesis of effective media metamaterials, for the implementation of metamaterial transmission lines, and for the design of RF/microwave components based on such resonators or on such artificial transmission lines. The list is limited to those resonators that are used in the following subsections and chapters of this book. All of them exhibit peculiarities that make them useful for certain applications, or represent some advantages over the original SRR. Indeed, with the exception of the folded stepped impedance resonators (SIRs), the other resonators included in the next subsections are derived from (or inspired by) the original SRR topology proposed by Pendry *et al*. [30]. The classification of these resonators can be made according to several criteria. In this book, the considered electrically small resonators are divided into

metallic and complementary (or slot) resonators (the latter are derived from the former by applying duality considerations).

3.3.1 Metallic Resonators

It was justified in the previous section the need to load a metallic loop with a capacitance in order to achieve a resonant behavior able to produce a strong diamagnetic behavior above resonance. However, the SRR of Figure 3.6 is not the unique topology providing a negative magnetic polarizability. Further topologies are analyzed and discussed in this subsection. Moreover, the concept of open particle will be introduced (as will be seen later, these open particles can be driven by means of a voltage or current source and are also useful for the implementation of metamaterial transmission lines).

3.3.1.1 The Non-Bianisotropic SRR (NB-SRR) The topology of the NB-SRR [75] is depicted in Figure 3.9. The equivalent circuit model and magnetic polarizability are those of the SRR (provided the same dimensions and substrate are considered). However, the distribution of charges in the NB-SRR differs from that of the SRR (Fig. 3.9). Unlike the SRR, a net electric dipole in the y-direction is not induced by an axial magnetic field in the NB-SRR. This means that cross polarizabilities are not present in this particle, which is said to be non-bianisotropic. This resonator can be of interest in certain applications to avoid mixed (i.e., simultaneous electric and magnetic) coupling.

3.3.1.2 The Broadside-Coupled SRR (BC-SRR) Like the NB-SRR, the BC-SRR (Fig. 3.10) exhibits inversion symmetry and is non-bianisotropic [69]. The drawback of this particle as compared to the NB-SRR, or SRR, is that two metal levels are required for its implementation. However, since the rings are etched face-to-face at both sides of the substrate, the distributed capacitance between the rings can be substantially enhanced by merely reducing the substrate thickness (or by increasing its dielectric constant). Therefore, this particle can potentially be electrically much smaller than the SRR or the NB-SRR.

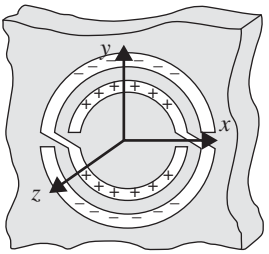

FIGURE 3.9 Topology of the NB-SRR and distribution of charges at the fundamental resonance. The metallization is indicated in white.

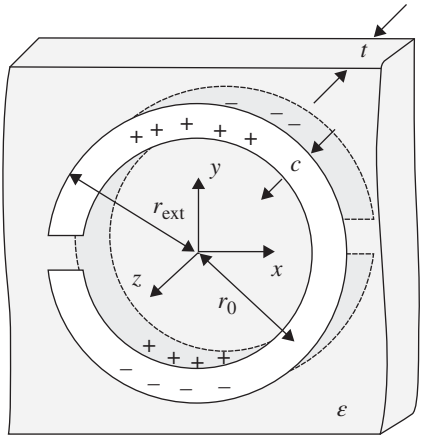

FIGURE 3.10 Topology of the BC-SRR and distribution of charges at the fundamental resonance. The metallization is indicated in white. Reprinted with permission from Ref. [4]; copyright 2008 John Wiley.

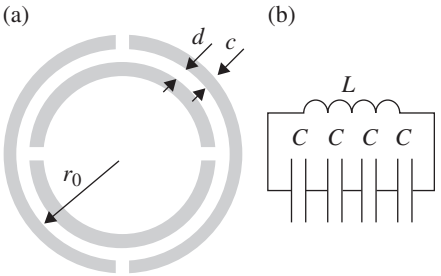

FIGURE 3.11 Topology of the DS-SRR and relevant dimensions (a) and equivalent circuit model (b).

3.3.1.3 The Double-Slit SRR (DS-SRR) The DS-SRR is derived from the original topology of the SRR by adding two cuts in each ring (Fig. 3.11) [75]. The resulting particle is also non-bianisotropic. It is electrically larger than the SRR since the capacitance of the particle is given by the series connection of the four capacitances corresponding to each quadrant. Such capacitances are $C = \pi r_o C_{pul}/2$, and therefore the total particle capacitance is four times smaller than that of the SRR. Since the inductance is identical to that of the SRR, it follows that the resonance frequency of the DS-SRR is twice the resonance frequency of the SRR (provided the same dimensions, shape, and substrate are considered). Although the particle is electrically larger, the symmetry of this particle is useful for the development of isotropic MNG media [4]. Since the ratio L/C is larger than the corresponding ratio in an SRR, the DS-SRR can also be useful for bandwidth broadening in transmission lines loaded with these particles (this aspect will be discussed in Chapter 6, in reference to common-mode suppressed differential lines).

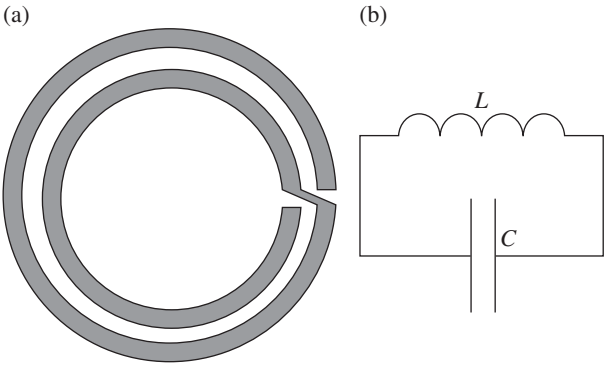

FIGURE 3.12 Topology of a two-turn SR (a) and equivalent circuit model (b).

3.3.1.4 The Spiral Resonator (SR) Spirals are well-known particles that have been largely used for the implementation of inductances in planar technology. However, the parasitic (distributed) capacitance between the turns actually provides a resonant behavior to the particle. Therefore, SRs exhibit a strong diamagnetic behavior above resonance and can be used for the synthesis of MNG media as well. The topology of a two-turn spiral resonator (SR) is depicted in Figure 3.12. Although the two-turn SR is older than the SRR, the elements of the equivalent circuit can be straightforwardly inferred from the analysis of the SRR [76]. Indeed, in terms of the equivalent circuit model, the single difference between these particles concerns the capacitance. In the SR, the edge capacitance is the one corresponding to the whole circumference, and thus given by $C = 2\pi r_o C_{pul}$. Since the inductance is identical to that of the SRR, the SR resonance frequency is half the resonance frequency of the SRR. In other words, the SR is electrically smaller than the SRR by a factor of two.

3.3.1.5 The Folded SIR As was pointed out in Chapter 1, half wavelength resonators are common building blocks in microwave circuit and filter design. Such elements are distributed resonators and hence are electrically large. However, dimensions can be reduced by narrowing and widening the central and external sections of the particle, respectively [77]. Further size reduction can be achieved by folding the structure, giving rise to the folded SIR (Fig. 3.13). The particle can be driven by a z-oriented magnetic field, inducing a strong magnetic dipole in that direction and an electric dipole in the plane of the particle (y-direction). Therefore, like the SRR, the folded SIR exhibits bianisotropy. In the folded SIR, the inductance of the particle is roughly the inductance of the narrow strip and the capacitance is the edge capacitance between the patches. However, coupled to transmission lines (specifically CPWs), a broadside coupling capacitance between the line and the particle arises, giving rise to very small resonance frequencies. This is of interest for size reduction as will be discussed later (see Section 4.3.2.3).

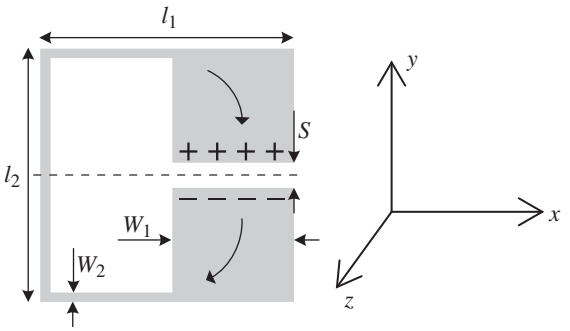

FIGURE 3.13 Topology of the folded SIR and relevant dimensions. The distribution of charges at the fundamental resonance is indicated, the symmetry plane being an electric wall. The depicted topology is square shaped, but it can be rectangular or circular as well.

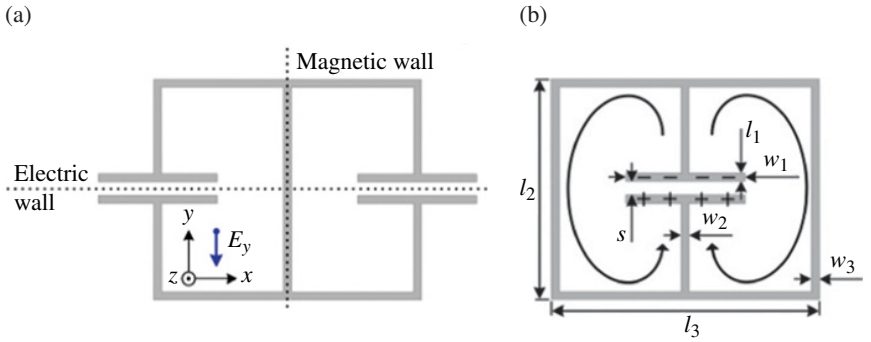

FIGURE 3.14 Topologies of the ELC resonator and relevant dimensions. (a) Loaded with capacitors in the external branches and (b) loaded with a capacitor in the central branch. The distribution of charges and current flow at the fundamental resonance (case b) are indicated.

3.3.1.6 The Electric LC Resonator (ELC) The ELC resonator was proposed in Ref. [78] as an alternative to the metallic wires for the implementation of ENG media with small absolute values of permittivity [4]. This is a bisymmetric resonator consisting of a pair of contacting capacitively loaded metallic loops (Fig. 3.14 depicts the two alternative topologies).[20] The application of a z-oriented time-varying magnetic field may induce a magnetic dipole moment in the particle. However, the induced currents will not flow through the central branch, since this would give opposite (canceling) magnetic dipole moments in each loop. This means that a uniform axial magnetic field is not able to excite the particle at the first (fundamental) resonance.[21] At the

[20] Obviously, circularly shaped ELCs are also possible.

[21] All the considered resonators exhibit higher-order (dynamic) resonances. Such resonances are analyzed in depth in Ref. [79]. However, the electrical size of the particles is large at the second- and higher-order resonances. Therefore, the homogeneity requirement for the implementation of effective media metamaterials is

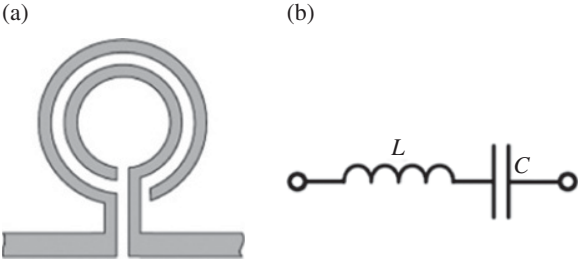

FIGURE 3.15 Topology of the OSRR (a) and equivalent circuit model (b).

fundamental resonance, current flows through the central branch, the horizontal symmetry plane is an electric wall, and an electric dipole in the *y*-direction appears. This means that the particle can be excited at the fundamental resonance by means of a uniform time-varying electric field applied in the *y*-direction, but not by a uniform *z*-oriented magnetic field. However, such electric field is not able to induce a magnetic dipole moment in the *z*-direction, and therefore the ELC resonator is non-bianisotropic. Notice that the vertical symmetry plane is a magnetic wall at the fundamental resonance. The presence of two planes of symmetry (an electric wall and a magnetic wall) is useful for the implementation of microwave components (sensors and bar codes) based on symmetry properties, as will be studied later (see Section 4.3.2.2).

3.3.1.7 The Open Split-Ring Resonator (OSRR) Unlike the previous resonators, the open split-ring resonator (OSRR) is an open resonator that can be driven by a voltage or current source applied to its terminals. The topology of the OSRR, firstly proposed by Martel *et al*. [80], can be derived from the two-turn SR topology by simply opening the metallic strip connecting the inner and outer rings of the spiral and providing access terminals to both rings (Fig. 3.15). This means that the equivalent circuit model of the OSRR can be derived from that of the two-turn SR by simply opening it. Namely, the OSRR can be modeled as an open series resonator where the inductance and capacitance are those of the two-turn SR. Thus, this particle is electrically smaller than the SRR by a factor of two.

3.3.2 Applying Duality: Complementary Resonators

In this subsection, complementary resonators are introduced by applying complementary considerations and duality [81–83] to the previous metallic particles. With the exception of the BC-SRR, the considered metallic resonators have their dual, or complementary, counterparts. The complementary particles are derived from the metallic ones by simply etching the corresponding topologies in a metallic screen. In other

not justified at these frequencies. Although the second resonance may be useful for certain microwave applications, most RF/microwave components based on these resonators or implemented by means of resonant-type metamaterial transmission lines exploit the fundamental resonance. For this reason, the analysis of the higher-order resonances is not included in this book.

words, they are negative images, and their EM behavior is roughly dual. Specifically, a negative effective permittivity can be expected for any medium comprising complementary particles of those exhibiting negative effective permeability. The following analysis is restricted to the complementary split-ring resonator (CSRR), first proposed in Refs. [84, 85], since for the other complementary particles the elements of the circuit model can be derived from those of the metallic particles in a similar way. However, the complementary version of the OSRR is also analyzed since further explanations are required for their full comprehension.

3.3.2.1 Complementary Split-Ring Resonator (CSRR) As it is well known, the complementary of a planar metallic structure is obtained by replacing the metal parts of the original structure with apertures, and the apertures with metal plates [81]. Due to symmetry considerations, it can be demonstrated that if the thickness of the metal plate is zero, and its conductivity is infinity (perfect electric conductor), then the apertures behave as perfect magnetic conductors. In that case, the original structure and its complementary are effectively dual; and if the field $\vec{F} = \left(\vec{E}, \vec{H}\right)$ is a solution for the original structure, its dual $\vec{F}'$ defined by

$$\vec{F}' = \left(\vec{E}', \vec{H}'\right) = \left(-\sqrt{\frac{\mu}{\varepsilon}}\cdot\vec{H}, \sqrt{\frac{\varepsilon}{\mu}}\cdot\vec{E}\right) \tag{3.36}$$

is the solution for the complementary structure. Thus, under these ideal conditions, a perfectly dual behavior is expected for the complementary screen of the SRR. Thus, whereas the SRR can be mainly considered as a resonant magnetic dipole that can be excited by an axial magnetic field, the CSRR (Fig. 3.16) essentially behaves as an electric dipole (with the same frequency of resonance) that can be excited by an axial electric field [82, 83]. The cross-polarization effects present in the SRR, discussed before, are also present in the CSRR. Thus, CSRRs exhibit a resonant magnetic polarizability along the *y*-axis (see Fig. 3.16); and therefore, its fundamental resonance can also be excited by an external magnetic field applied along this direction [10].

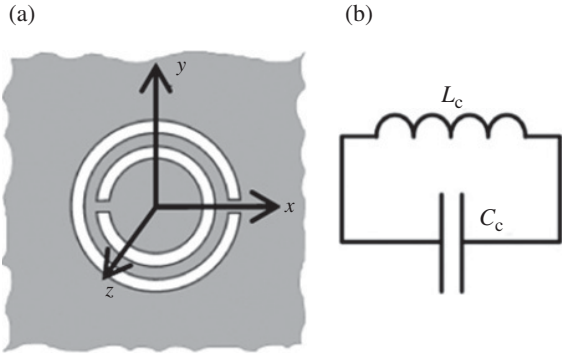

FIGURE 3.16 Topology of the CSRR (a) and equivalent circuit model (b).

Rigorously speaking, due to the continuity of the tangential/normal components of the electric/magnetic fields in the CSRR plane, $\vec{F}'$ in Equation 3.36 is the solution on one side of this plane, and $-\vec{F}'$ is the solution on the other side. With regard to the CSRR polarizabilities, this means that the sign of such polarizabilities changes from one side to another. Therefore, the net electric and magnetic dipoles on the CSRR must vanish, a result that can also be deduced from the fact that electric currents confined in a plane cannot produce any net normal/tangential electric/magnetic polarization. However, when the CSRR is seen from one side, the aforementioned effective polarizabilities arise.

The circuit model of the CSRR is depicted in Figure 3.16b, where L_c and C_c are the inductance and capacitance of the particle, respectively. The sub-index "c" denotes that these reactive elements are those corresponding to the CSRR. Since these parameters are related to the reactive elements of the circuit model of the SRR, let us redefine these elements as L_s and C_s, where the subindex indicates that these parameters are referred to the SRR. Moreover, let us define C_o as $C_o = 2\pi r_o C_{pul}$ (so that the capacitance C of the SRR model of Figure 3.6 is $C = C_o/2$ and the whole capacitance of the SRR is $C_s = C_o/4$). For the CSRR, the capacitance C_c is calculated as the capacitance of a disk of radius $r_o - c/2$ surrounded by a metal plane at a distance c of its edge. The inductance L_c is given by the parallel combination of the two inductances connecting the inner disk to the outer metallic region of the CSRR. Each inductance is given by $L_o/2$, where $L_o = 2\pi r_o L_{pul}$, and L_{pul} is the per-unit length inductance of the CPWs connecting the inner disk to the surrounding metallic region. For infinitely thin perfect conducting screens, and in the absence of any dielectric substrate, it directly follows from duality that the parameters of the circuit models for the SRRs and the CSRRs are related by $C_c = 4(\varepsilon_o/\mu_o)L_s$ and $C_o = 4(\varepsilon_o/\mu_o)L_o$ [4, 10]. Therefore, under such ideal conditions, the resonance frequencies of the SRR and CSRR are identical, as is expected from duality. In practice, the conductor has a finite width (and losses), and a substrate is needed, which means that the resonance frequencies of the metal and complementary particles are "roughly" the same (but not identical). An exhaustive analysis of the effects of substrate thickness and dielectric constant on the divergence between the resonance frequencies of SRRs and CSRRs is reported in Refs. [4, 10]. The formula providing the capacitance C_c of the CSRR when a dielectric substrate is present was derived in Ref. [10], whereas the value of L_o can be inferred from the design formulas giving the per-unit-length inductance of a CPW [70].

The previous analysis can be extended to the complementary version of the aforementioned particles, with exception of the BC-SRR. These complementary particles are designated canonically as non-bianisotropic complementary SRR (NB-CSRR), complementary SR (CSR), double-slit complementary SRR (DS-CSRR), folded complementary SIR (CSIR), and open complementary SRR (OCSRR). The complementary counterpart of the ELC resonator is a magnetically driven resonator (the magnetic field must be applied in the plane of the particle), and for this reason the particle is called magnetic LC (MLC) resonator. The complementary version of the OSRR, that is, the OCSRR, can also be analyzed from duality considerations. However, the fact that the OCSRR is an open particle needs some attention. Moreover, since this particle

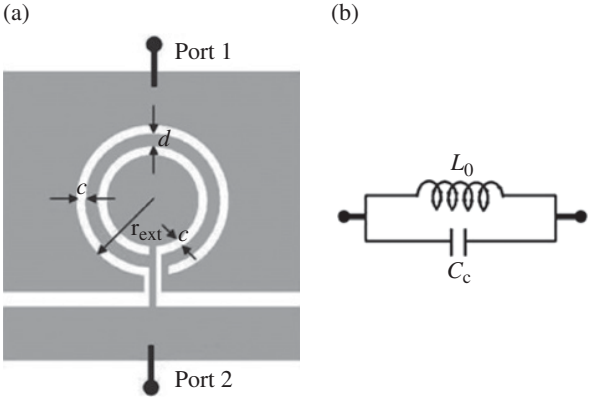

FIGURE 3.17 Topology of the OCSRR (a) and equivalent circuit model (b).

will be part of several circuits discussed later, the OCSRR is briefly analyzed in the next subsection.

3.3.2.2 Open Complementary Split-Ring Resonator (OCSRR) The OCSRR was first proposed in Ref. [86] (Fig. 3.17). This is the complementary version of the OSRR, but it can also be viewed as an open CSRR. However, notice that in the OCSRR, the connecting terminals (or ports) are located at both sides of the central slot. Between these ports, there is an electric short through the metal between the inner and outer slot rings forming the particle, but there is also capacitive connection through the capacitances across the slots. Thus, according to this, the circuit model of the particle is an open parallel resonant tank, as Figure 3.17b illustrates. The inductance of the particle is L_o, whereas the capacitance is identical to the capacitance of the CSRR, C_c. Since the inductance of the CSRR is $L_o/4$, it is expected that the resonance frequency of the OCSRR is one half the resonance frequency of the CSRR. Notice that from duality considerations, it follows that the OSRR and OCSRR have very similar resonance frequencies. As will be seen later, the combination of OSRRs and OCSRRs is very useful for the design of metamaterial transmission lines and many circuits based on them.

3.4 CANONICAL MODELS OF METAMATERIAL TRANSMISSION LINES

In this section, the canonical models for the implementation of metalines are introduced. By canonical model, we refer to the simplest circuit model that mimics an LH metamaterial (i.e., the dual transmission line model), and to a family of circuits that exhibit backward and forward wave propagation, depending on the frequency band, and are useful for microwave circuit design on the basis of dispersion and impedance engineering. Let us begin with the dual transmission line model. The following subsections are dedicated to those models able to exhibit backward and

forward wave behavior, obtained by increasing the number of reactive elements. In these models, losses are not considered.

3.4.1 The Dual Transmission Line Concept

The concept of backward waves in RF/microwave engineering is an old concept [31]. Backward waves can be generated by feeding a ladder network with series-connected capacitors and shunt-connected inductors alternating, as shown in Figure 3.18a. This network is the dual version of the equivalent circuit model of a lossless transmission line (Fig. 3.18b); and for this reason, this ladder network is designated as dual transmission line. The dual transmission line exhibits backward (or LH) wave propagation, and wave propagation characteristics can be controlled by the value of the reactive elements. However, the potential of these lines by themselves is very limited due to the fact that the unit cell (see the T-circuit in Fig. 3.18c) contains only two reactive elements. Nevertheless, let us study the dual transmission line in detail and compare it with the circuit model of an ordinary lossless transmission line. Afterward, the CRLH transmission line concept will be introduced.

The analysis of the propagation characteristics of the dual and conventional transmission line models can be realized by means of the transfer matrix approach (see Chapter 2). Applying expressions (2.23), with A given by (2.28a), and (2.30) to the circuit of Figure 3.18a, the phase constant and characteristic (or Bloch) impedance of the dual transmission line are found to be

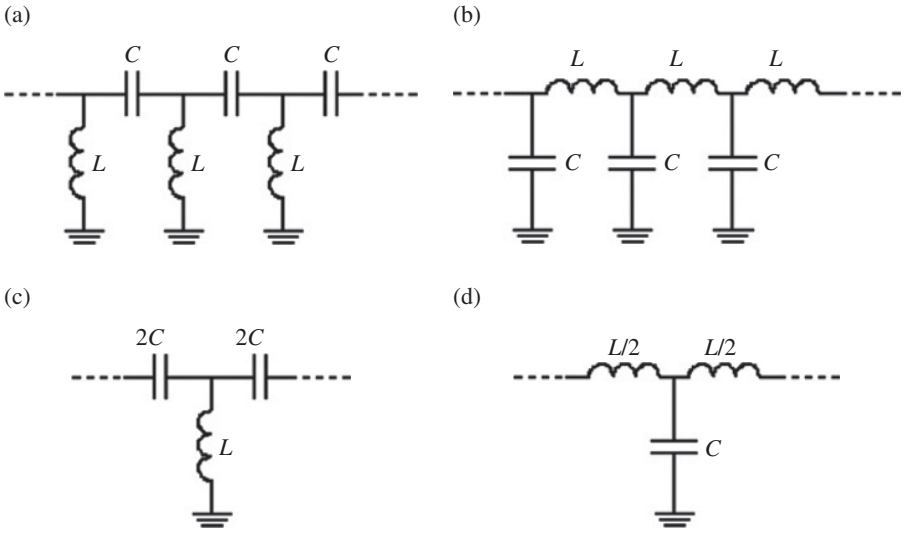

FIGURE 3.18 Equivalent circuit model of a backward (a) and forward (b) transmission line. The T-circuit models of the basic cell structures are also indicated in (c) and (d). Reprinted with permission from Ref. [4]; copyright 2008 John Wiley.

$$\cos\beta_{\mathrm{L}} l = 1 - \frac{1}{2LC\omega^2} \tag{3.37}$$

$$Z_{\mathrm{BL}} = \sqrt{\frac{L}{C}\left(1 - \frac{\omega_{\mathrm{cL}}^2}{\omega^2}\right)} \tag{3.38}$$

where l is the period, $Z_{\mathrm{s}} = -j/\omega C$, $Z_{\mathrm{p}} = j\omega L$, and $\omega_{\mathrm{cL}} = 1/2(LC)^{1/2}$ is an angular cutoff frequency (propagation below ω_{cL} is not allowed since the Bloch impedance is imaginary). In (3.37) and (3.38), the subscript "L" indicates that the phase constant and characteristic impedance are those of the dual, or LH, transmission line. For the model of a conventional (forward) transmission line, application of (2.23) and (2.30) gives

$$\cos\beta_{\mathrm{R}} l = 1 - \frac{LC}{2}\omega^2 \tag{3.39}$$

$$Z_{\mathrm{BR}} = \sqrt{\frac{L}{C}\left(1 - \frac{\omega^2}{\omega_{\mathrm{cR}}^2}\right)} \tag{3.40}$$

where $\omega_{\mathrm{cR}} = 2/(LC)^{1/2}$ is the angular cutoff frequency for the forward transmission line model of Figure 3.18b, and the subscript "R" is indicative of forward or RH wave propagation in the allowed regions of this line.[22]

The dispersion diagram and the dependence of Z_{B} on frequency for the networks of Figure 3.18 are depicted in Figure 3.19. Transmission is limited to those frequency intervals that make the phase constant and the characteristic impedance to be real numbers. It is worth mentioning that frequency dispersion is present in both structures. Even though the circuit of Figure 3.18b models an ideal lossless ordinary (forward) transmission line, where dispersion is absent, actually this circuit is only valid for frequencies satisfying $\omega << \omega_{\mathrm{cR}}$, that is, in the long wavelength limit (corresponding to those frequencies where wavelength for guided waves satisfies, $\lambda_{\mathrm{g}} >> l$). To correctly model an ideal lossless transmission line at higher frequencies, we simply need to reduce the period of the structure, and accordingly the per-section inductance and capacitance of the line, L and C, with the result of a higher cut-off frequency. Thus, the circuit of Figure 3.18b can properly describe ideal transmission lines without dispersion. To this end we simply need to select the period such that the long wavelength limit approximation holds. Under this approximation, expressions (3.39) and (3.40) lead us to expressions (1.6) and (1.9), and the phase and group velocities are given by (1.10) and (1.11), and they are positive and constant, as expected.

Conversely, the backward wave structure of Figure 3.18a is dispersive even in the long wavelength limit. In order to identify this structure as an effective medium (i.e., one-dimensional metamaterial), operation under this approximation is required. However, regardless of the operating frequency within the transmission band, the structure supports backward waves and, for this reason, it is an LH transmission line. In order to

[22] Notice that (3.40) is identical to (2.34).

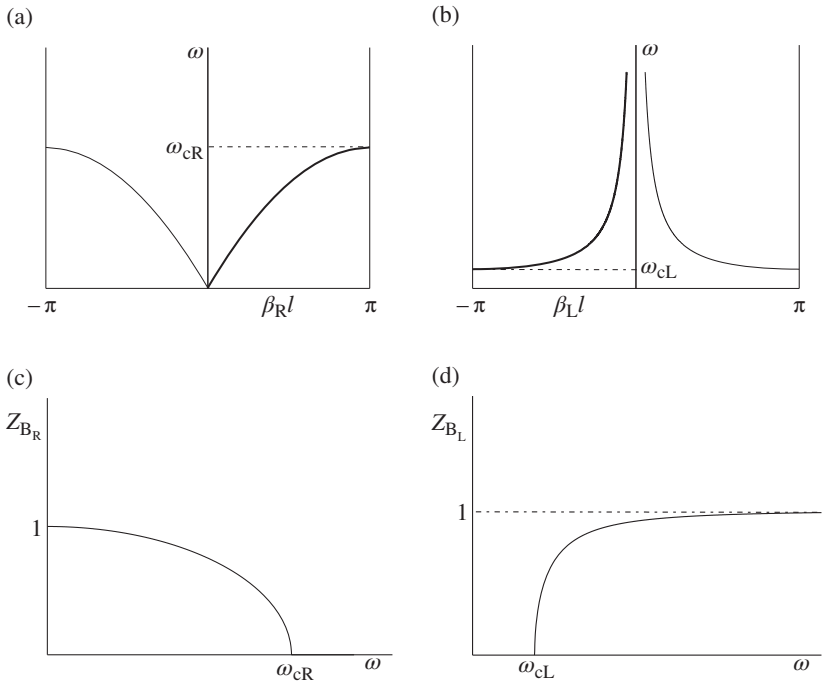

FIGURE 3.19 Typical dispersion diagram of a forward (a) and backward (b) transmission line model. The dependence of the normalized Bloch impedance with frequency is shown in (c) and (d) for the forward and backward lines, respectively. Reprinted with permission from Ref. [4]; copyright 2008 John Wiley.

properly identify effective constitutive parameters, μ_{eff} and ε_{eff}, the long wavelength approximation is necessary. However, as has been previously discussed, operation under this approximation is not a due for microwave circuit design. Nevertheless, for coherence and simplicity, the phase constant, the characteristic impedance, as well as the phase and group velocities are derived under the long wavelength limit ($\omega >> \omega_{\text{cL}}$). The following results are obtained:

$$\beta_{\text{L}} l = -\frac{1}{\omega\sqrt{LC}} \tag{3.41}$$

$$Z_{\text{BL}} = \sqrt{\frac{L}{C}} \equiv Z_{\text{lw}} \tag{3.42}$$

$$v_{\text{pL}} = \frac{\omega}{\beta_{\text{L}}} = -\omega^2 l\sqrt{LC} < 0 \tag{3.43}$$

$$v_{gL} = \left(\frac{\partial \beta_L}{\partial \omega}\right)^{-1} = +\omega^2 l\sqrt{LC} > 0 \tag{3.44}$$

and the phase and group velocities have opposite signs. From a mathematical point of view, in the dispersion diagrams for the forward and backward lines depicted in Figure 3.19, and obtained from expressions (3.37) and (3.39), the sign of β can be either positive or negative. This ambiguity comes from the two possible directions of energy flow, namely from left to right or vice versa. If we adopt the usual convention of energy flow from left to right, then the sign of the phase constant is determined by choosing that portion of the curves that provide a positive group velocity (bold lines in Fig. 3.19a and b), as it was pointed out in Section 2.2. From this, it is clear that for the forward transmission line, β and v_p are both positive, whereas these magnitudes are negative for the backward transmission line. In both cases, v_g is positive as one expects on account of the co-directionality between power flow and group velocity.[23]

In the backward and forward transmission lines depicted in Figure 3.18, it is possible to identify effective constitutive parameters. To this end, we should take into account that TEM wave propagation in planar transmission lines and plane wave propagation in source-free, linear, isotropic, and homogeneous dielectrics are described by identical equations (telegrapher equations) provided the following mapping holds (Appendix A):

$$Z_s'(\omega) = j\omega\mu_{eff} \tag{3.45}$$

$$Y_p'(\omega) = j\omega\varepsilon_{eff} \tag{3.46}$$

where Z_s' and Y_p' are the per-unit length series impedance and shunt admittance of the considered line. Thus, for the forward line the effective permittivity and permeability are constant and given by[24]

$$\varepsilon_{eff} = \frac{C}{l} \tag{3.47}$$

$$\mu_{eff} = \frac{L}{l} \tag{3.48}$$

[23] As pointed out in Section (6.4.2), not always the group velocity is restricted to positive values smaller than c (the speed of light in vacuum). Superluminal (higher than c) and negative group velocities are possible in real structures. However, these abnormal velocities are not in contradiction with Einstein causality since the group velocity is not the velocity of information transfer.

[24] These expressions are equivalent to (A.22a) and (A.22b). Notice that the effective permeability and permittivity depend on the transverse geometry of the considered line and cannot be identified with the permittivity and permeability of the dielectric material of such line. This is true even for purely TEM transmission lines.

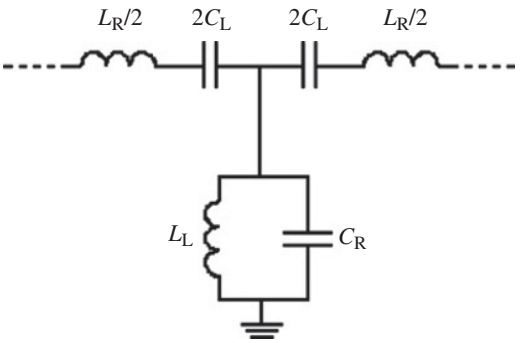

FIGURE 3.20 Equivalent circuit model (basic cell) of the CRLH transmission line.

whereas for the backward transmission line, the constitutive parameters are

$$\varepsilon_{\text{eff}} = -\frac{1}{\omega^2 Ll} \tag{3.49}$$

$$\mu_{\text{eff}} = -\frac{1}{\omega^2 Cl} \tag{3.50}$$

and they are both negative, a sufficient condition to obtain LH wave propagation.

3.4.2 The CRLH Transmission Line

From a practical point of view, in order to implement a dual (or backward) transmission line, a host line (microstrip or CPW, among others) is required. The host line introduces thus parasitic elements that in general may not be negligible, and they should be taken into account to accurately describe the propagation characteristics of the lines.[25] These structures may exhibit LH or RH wave propagation, depending on the frequency interval; and for this reason, they have been termed as CRLH transmission lines [11]. The equivalent circuit model (unit cell) of these structures is depicted in Figure 3.20. For clarity, we have renamed the reactive elements of the dual transmission line as C_L and L_L, while C_R and L_R correspond to the per-section capacitance and inductance of the host line. By using (2.23) and (2.30), the dispersion relation as well as the characteristic impedance of the CRLH transmission line can be inferred, namely

$$\cos\beta l = 1 - \frac{\omega^2}{2\omega_R^2}\left(1 - \frac{\omega_s^2}{\omega^2}\right)\left(1 - \frac{\omega_p^2}{\omega^2}\right) \tag{3.51}$$

[25] The parameters of the host line are parasitics for the synthesis of a purely LH line. However, these reactive elements play a key role in most practical CRLH lines, where they are typically tailored in order to achieve certain line specifications.

$$Z_B = \sqrt{\frac{L_R}{C_R}\frac{\left(1-\left(\omega_s^2/\omega^2\right)\right)}{\left(1-\left(\omega_p^2/\omega^2\right)\right)} - \frac{L_R^2\omega^2}{4}\left(1-\frac{\omega_s^2}{\omega^2}\right)^2} \tag{3.52}$$

where the following variables

$$\omega_R = \frac{1}{\sqrt{L_R C_R}} \tag{3.53}$$

$$\omega_L = \frac{1}{\sqrt{L_L C_L}} \tag{3.54}$$

and the series and shunt resonance frequencies

$$\omega_s = \frac{1}{\sqrt{L_R C_L}} \tag{3.55}$$

$$\omega_p = \frac{1}{\sqrt{L_L C_R}} \tag{3.56}$$

have been introduced to simplify the mathematical formulas. Expressions 3.51 and 3.52 are depicted in Figure 3.21. Two propagating regions, separated by a gap at the spectral origin can be distinguished. In the lowest frequency region, the parameters of the dual transmission line, C_L and L_L, are dominant and wave propagation is backward. This situation is reversed above the stop band, where the parasitic reactances of the host line make the structure to behave as a RH line. Indeed, at high frequencies the CRLH transmission line tends to behave as a purely right handed (PRH) line.

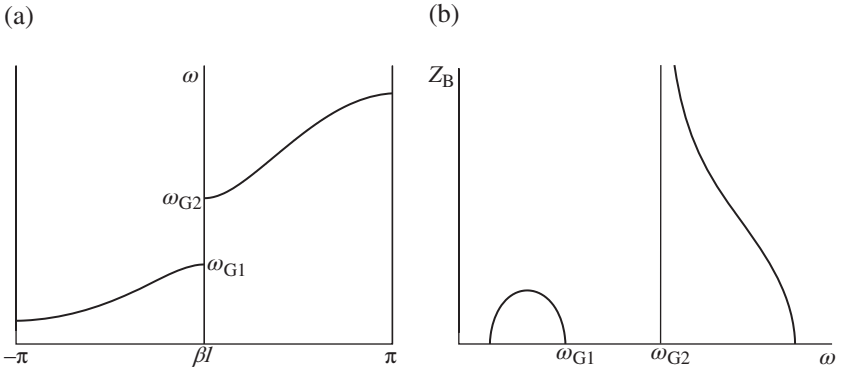

FIGURE 3.21 Typical dispersion diagram (a) and variation of Bloch impedance with frequency (b) in a CRLH transmission line model. In this example, $\omega_s < \omega_p$. Reprinted with permission from Ref. [4]; copyright 2008 John Wiley.

Conversely, in the lower limit of the first allowed band, the CRLH structure exhibits the characteristics of a purely left handed (PLH)—or dual—transmission line. The gap limits are given by the frequencies satisfying.

$$\omega_{G1} = \min\left(\omega_s, \omega_p\right) \tag{3.57}$$

$$\omega_{G2} = \max\left(\omega_s, \omega_p\right) \tag{3.58}$$

In the long wavelength limit, expression (3.51) rewrites as follows:

$$\beta = \frac{s(\omega)}{l}\sqrt{\frac{\omega^2}{\omega_R^2}\left(1-\frac{\omega_s^2}{\omega^2}\right)\left(1-\frac{\omega_p^2}{\omega^2}\right)} \tag{3.59}$$

where $s(\omega)$ is the following sign function:

$$s(\omega) = \begin{cases} -1 & \text{if} \quad \omega < \min\left(\omega_s, \omega_p\right) \\ +1 & \text{if} \quad \omega > \max\left(\omega_s, \omega_p\right) \end{cases} \tag{3.60}$$

From the phase constant (Eq. 3.59), the phase and group velocities can be easily inferred, these velocities being of opposite sign in the LH band and both being positive in the RH band.

With regard to the constitutive parameters for the CRLH transmission line, they can be inferred as previously indicated, that is,

$$\varepsilon_{eff} = \frac{C_R}{l} - \frac{1}{\omega^2 L_L l} \tag{3.61}$$

$$\mu_{eff} = \frac{L_R}{l} - \frac{1}{\omega^2 C_L l} \tag{3.62}$$

and they can be positive or negative, depending on the frequency range.

One particular case of interest is the so-called balanced CRLH line, which corresponds to the situation where the series and shunt resonances are identical, namely $\omega_s = \omega_p = \omega_o$ [3]. In this case, there is not a forbidden band between the LH and RH allowed bands; in other words, the change between backward and forward wave behaviour is continuous. Concerning the characteristic impedance, it reaches its maximum at ω_o (the transition frequency),[26] where

[26] Do not confuse the transition frequency of a balanced CRLH line with the fundamental resonance frequency of the SRR, introduced before and described by the same symbol.

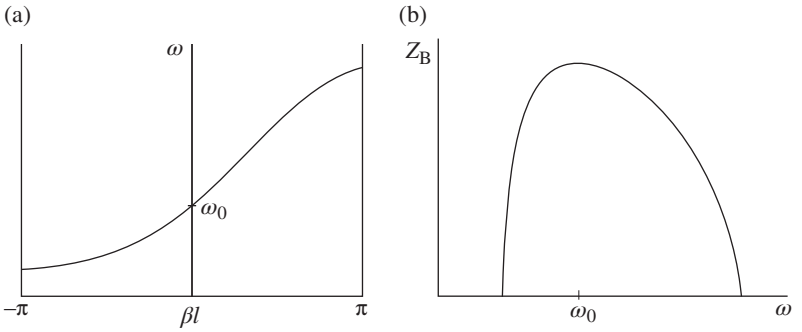

FIGURE 3.22 Typical dispersion diagram (a) and variation of Bloch impedance with frequency (b) in a balanced CRLH transmission line. Reprinted with permission from Ref. [4]; copyright 2008 John Wiley.

$$Z_B = \sqrt{\frac{L_R}{C_R}} = \sqrt{\frac{L_L}{C_L}} \tag{3.63}$$

and the characteristic impedance decreases as frequency increases or decreases from ω_o. At the limits of the allowed propagation interval (which contains both the LH and RH frequency bands), the characteristic impedance nulls, and beyond these limits, it takes imaginary values. Figure 3.22 depicts the dispersion diagram and the variation of line impedance with frequency. By contrast, the characteristic impedance dependence on frequency is more complicated for the unbalanced case (see Fig. 3.21). If we consider that $\omega_s < \omega_p$ (which is the situation considered in Fig. 3.21), the characteristic impedance is zero at the lower limit of the LH interval, it increases as frequency increases, reaches a maximum, and then decreases towards zero, at ω_s, the upper limit of the LH band. In the RH band, the impedance exhibits a pole at ω_p (the lower frequency limit), it decreases as frequency increases, and it nulls at the higher cutoff frequency of the RH band. However, the behavior changes if $\omega_s > \omega_p$; in this case, the impedance goes from zero up to infinity in the LH pass band, and it nulls at the edges of the RH band.

From the point of view of the characteristic impedance, the balanced CRLH transmission line is interesting because in the vicinity of the transition frequency, Z_B is not very dependent on frequency, and it allows for broadband matching, as compared to the unbalanced case, where the characteristic impedance is much more sensitive to frequency. On the other hand, the balanced case exhibits another important difference as compared to the unbalanced CRLH transmission line. Namely, at the transition frequency, where the phase velocity exhibits a pole, the phase shift[27] is zero, and the group velocity is different than zero. In other words, at this frequency, wave propagation is possible ($v_g \neq 0$) with $\beta = 0$. The phase origin of the balanced CRLH line

[27] Notice that by phase shift, we refer to the phase of the transmission coefficient, which is of opposite sign than the phase constant.

takes place thus at ω_o. When frequency is decreased below ω_o, the phase becomes positive (β negative) and it increases progressively; conversely, when frequency increases from ω_o, the phase increases in magnitude but with negative sign (as occurs in conventional transmission lines). Concerning the behaviour of wavelength for guided waves, λ_g, in the balanced CRLH transmission line, this reaches its maximum (infinity) at ω_o, and λ_g decreases as frequency increases or decreases from ω_o. Indeed, for the unbalanced case, the guided wavelength also increases when frequency approaches the spectral gap. However, at the edges of the gap the group velocity is zero, the line impedance takes extreme values and signal propagation is not allowed.

3.4.3 Other CRLH Transmission Lines

A CRLH transmission line can be achieved from various combinations of inductances and capacitances. Let us review the canonical models providing such composite behavior.

3.4.3.1 The Dual CRLH (D-CRLH) Transmission Line The D-CRLH line is obtained by simply interchanging the series LC resonator of the series branch with the parallel LC resonator of the shunt branch in the circuit of Figure 3.20. The result is the T-circuit depicted in Figure 3.23 [87]. This circuit exhibits forward wave propagation at low frequencies, and backward wave propagation at high frequencies, and it is opaque in a certain frequency band even under balanced conditions (i.e., identical series and shunt resonances). The dispersion diagram and the characteristic impedance for this line model, inferred from (2.23) and (2.30), are

$$\cos\beta l = 1 - \frac{\omega_L^2}{2\omega^2}\left(1 - \frac{\omega_s^2}{\omega^2}\right)^{-1}\left(1 - \frac{\omega_p^2}{\omega^2}\right)^{-1} \tag{3.64}$$

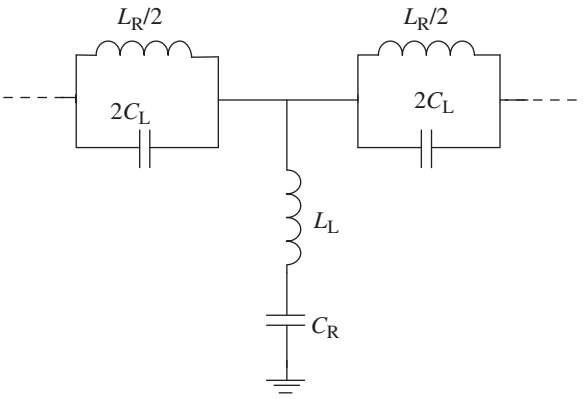

FIGURE 3.23 Equivalent circuit model (basic cell) of the D-CRLH transmission line.

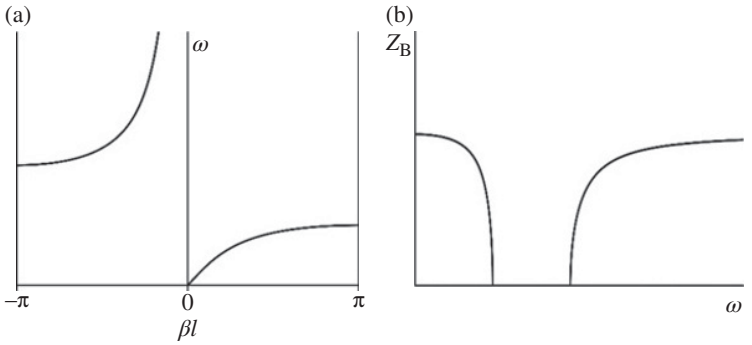

FIGURE 3.24 Typical dispersion diagram (a) and variation of Bloch impedance with frequency (b) in a balanced D-CRLH transmission line.

$$Z_B = \sqrt{\frac{L_L}{C_L}\frac{\left(1-\left(\omega_p^2/\omega^2\right)\right)}{\left(1-\left(\omega_s^2/\omega^2\right)\right)} - \frac{1}{4C_L^2\omega^2}\frac{1}{\left(1-\left(\omega_s^2/\omega^2\right)\right)^2}} \tag{3.65}$$

and typical diagrams are depicted in Figure 3.24. In (3.64) and (3.65), ω_L, ω_s, and ω_p are given by expressions (3.54)–(3.56).

3.4.3.2 Higher-Order CRLH and D-CRLH Transmission Lines Both the CRLH and the D-CRLH line models exhibit an LH band and an RH band. The number of bands can be arbitrarily extended by increasing the number of reactive elements in the series and shunt branches [88–91]. Indeed, the circuits of Figures 3.20 and 3.23 can be considered order-2 models, where the order index indicates the number of reactive elements of the series and shunt branches, and also the number of bands.[28] Figure 3.25 depicts order-3 and order-4 CRLH and D-CRLH transmission line models and the corresponding dispersion diagrams. The LH and RH bands alternate. However, the first transmission band is LH for the CRLH lines, whereas it is forward for the D-CRLH line models. The order-3 D-CRLH model of Figure 3.25 has been designated as double Lorentz metamaterial transmission line since the effective permittivity and permeability exhibit a Lorentz-type behavior [92]. The order-4 CRLH model of Figure 3.25 has been called extended CRLH (E-CRLH) transmission line [88]. As the order increases, the number of possible combinations of inductances and capacitances in the series and shunt branches providing a CRLH or a D-CRLH behavior also increases. In order to achieve a CRLH transmission line behavior, the reactance of the series branch and the susceptance of the shunt branch must be

[28] The order of a CRLH line should not be confused with the order of a filter. Notice that the unit cells of the CRLH (Fig. 3.20) and D-CRLH (Fig. 3.23) lines are third-order bandpass and bandstop filters, respectively. If several unit cells are cascaded, the resulting structure is a higher order periodic filter and an order-2 CRLH (or D-CRLH) line with multiple cells. CRLH lines can be applied to the implementation of bandpass filters, but it is sometimes convenient to sacrifice periodicity to achieve good filter performance.

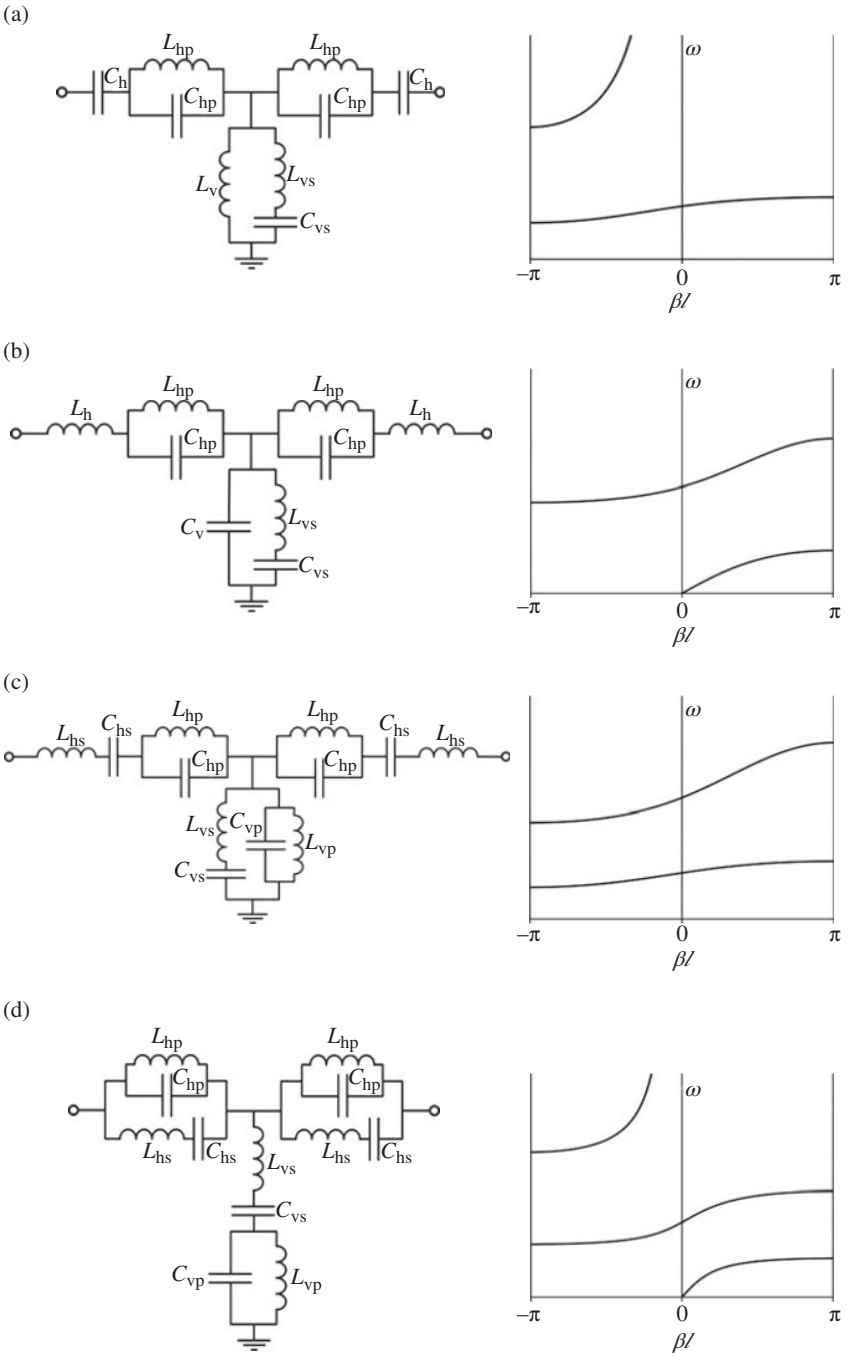

FIGURE 3.25 Order-3 CRLH (a), order-3 D-CRLH (b), order-4 CRLH (c), and order-4 D-CRLH (d) transmission line models (T-circuit) and the corresponding dispersion diagrams.

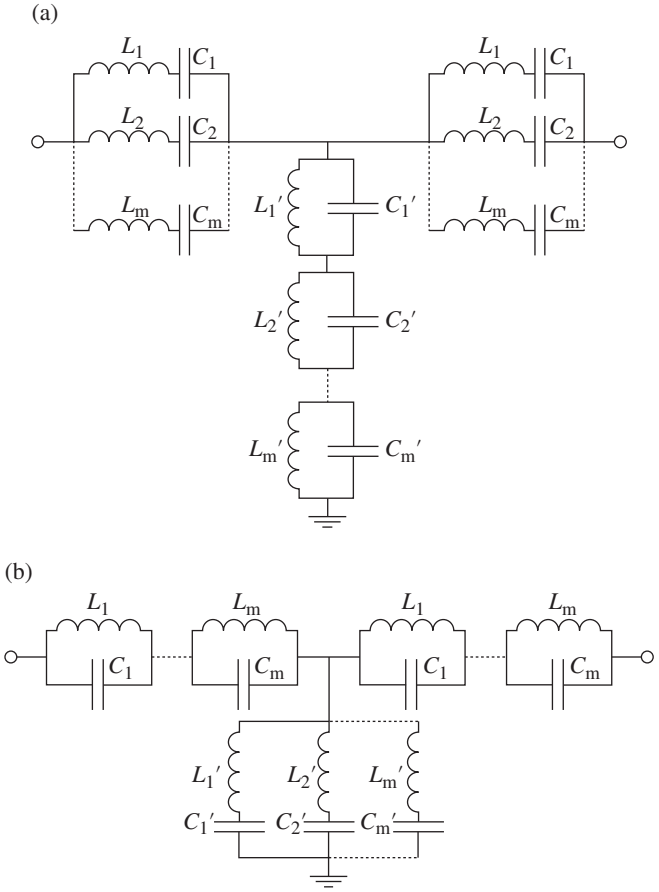

FIGURE 3.26 Generalized CRLH (a) and D-CRLH (b) transmission line models.

both negative in the DC limit (low frequencies). Conversely, the sign must be positive for a D-CRLH line. From the Foster reactance theorem [93], the sign of the reactance or susceptance slope for a network composed of inductances and capacitances is always positive. This means that the poles and zeros alternate. Therefore, to obtain a CRLH or a D-CRLH behavior, it suffices to place the zeros and poles of the reactance (series branch) at the same frequencies than the zeros and poles of the susceptance (shunt branch). It has been demonstrated that any network giving a CRLH behavior of even order, and containing the same number of reactive elements in the series and shunt branches, can be transformed to the generalized network depicted in Figure 3.26a (the generalized D-CRLH line model is depicted in Fig. 3.26b) [90].

In the previous paragraph, it has been considered that the number of reactive elements of the series and shunt branch is identical. However, this condition is not necessary in order to achieve a CRLH behavior with multiple bands. For instance, a CRLH transmission line can be achieved by simply using a series LC resonator in

the series branch, and a complex network of capacitors and inductors in the shunt branch. The necessary (although not sufficient) condition to achieve an LH/RH band is a negative/positive reactance (series branch) and susceptance (shunt branch). Ultimately, the transmission bands and the forward or backward nature of wave propagation in those bands are dictated by the dispersion diagram, derived from (2.23). Examples of metamaterial transmission lines described by T-circuit unit cells with different number of reactive elements in the series and shunt branches will be reported later.

To end this section, let us highlight that there is another class of CRLH or D-CRLH transmission lines: those based on the lattice network and bridged-T topologies. Such transmission line models and their physical realizations are discussed in Chapter 6, focused on advanced topics.

3.5 IMPLEMENTATION OF METAMATERIAL TRANSMISSION LINES AND LUMPED-ELEMENT EQUIVALENT CIRCUIT MODELS

This section is devoted to the physical implementations of order-2 CRLH metamaterial transmission lines. The implementation of higher-order lines will be discussed in Chapter 4 (applications of metalines), specifically in the section focused on the design of multiband components, where quad-band devices based on order-4 CRLH lines are reported. There are two main physical implementations of order-2 CRLH transmission lines: (1) the CL-loaded approach and (2) the resonant-type approach.[29] Let us review them in the next subsections.

3.5.1 CL-Loaded Approach

Order-2 CRLH transmission lines can be implemented by loading a host line with series capacitors and shunt inductors. In the model of the CRLH transmission line of Figure 3.20, the host line is described by the per-section line inductance (L_R) and capacitance (C_R), whereas the loading elements are accounted for by the inductance L_L and the capacitance C_L. The host line can be any type of planar transmission line, such as microstrip, strip line, or CPW transmission line, among others. For the reactive elements (series capacitor and shunt inductor), two possibilities arise, namely the use of lumped (surface mount technology—SMT) elements, or semilumped (i.e., electrically small) planar components. The advantage of lumped elements is their size. However, lumped elements can operate only in a limited frequency range (typically below 5–6 GHz) due to parasitic effects that cause self-resonance to appear. Moreover, it is difficult to achieve the required electrical characteristics by using lumped

[29] Actually, resonant-type CRLH metalines based on SRRs or CSRRs, to be discussed later in this chapter, are described by circuit models (unit cells) with two reactive elements in one branch and three reactive elements in the other branch. Therefore, strictly speaking, these lines cannot be considered to be order-2 CRLH lines. However, these lines exhibit two frequency bands (one forward and the other backward). In this sense, we can include these SRR- and CSRR-based lines among the order-2 CRLH lines.

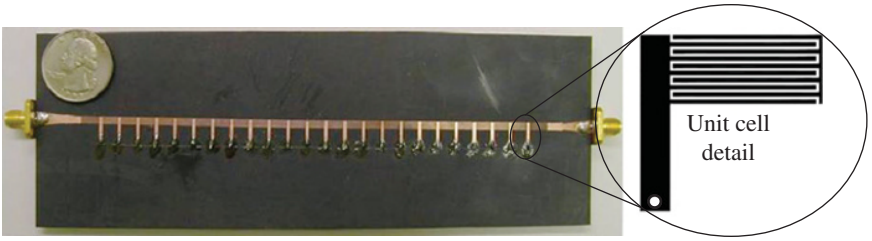

FIGURE 3.27 Microstrip CRLH transmission line implemented by means of shunt-connected grounded stubs and interdigital capacitors. Reprinted with permission from Ref. [3]; copyright 2006 by John Wiley.

elements since their values are restricted to those provided by the manufacturers. Finally, the use of lumped elements is more expensive, soldering is necessary (it causes additional losses), and it goes against the full integration of microwave components. Hence, semilumped elements are preferred.

Two main host lines have been considered for the synthesis of CRLH transmission lines: microstrip lines and CPWs. CL-loaded CRLH microstrip lines were proposed by Caloz *et al*. [94] in 2002, and subsequently used in many applications. The implementation of a CRLH structure by means of a CPW configuration was due to the group of Eleftheriades [15], who used the structure to generate backward leaky waves. The microstrip structure proposed by Caloz *et al*. consists of a periodic arrangement of series interdigital capacitors alternated with grounded (through metallic vias) stubs, which act as shunt connected inductors (Fig. 3.27). The interdigital capacitors are described by the series capacitance C_L in the circuit of Figure 3.20, whereas L_L models the grounded stubs. The other reactive elements C_R and L_R correspond to the line capacitance and inductance, respectively. The synthesis procedure and parameter extraction of these lines is not given in this book (see Ref. [3] for details). Such parameter extraction and synthesis methods will be exhaustively considered for resonant-type CRLH transmission lines, where the author's own experience is provided. Nevertheless, the frequency responses (measured, simulated through EM solvers and by means of circuit simulation) of a nine-cell balanced structure and a seven-cell unbalanced design are depicted in Figure 3.28 [3]. The transition frequency in the balanced structure is $f_o = 3.9$ GHz. This structure does not exhibit a stop band between the LH and the RH band; however, this stop band is present in the unbalanced structure. Alternatively, CRLH microstrip transmission lines can be implemented by replacing the shunt stubs with via holes in a mushroom type configuration similar to the high impedance surfaces proposed by Sievenpiper *et al*. [95] in one dimension. A two-dimensional structure, where caps are used to enhance the capacitive coupling between adjacent patches, was proposed in Ref. [58].

In CPW configuration, the shunt inductors can be implemented by means of connecting strips between the central strip and ground planes. The series capacitors can be implemented through interdigital geometries, or by means of series gaps. The latter are simpler, but the achievable capacitance values are much smaller. The Eleftheriades

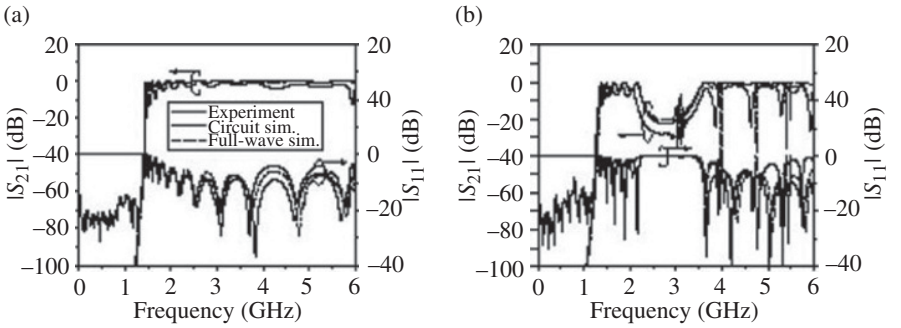

FIGURE 3.28 Typical frequency responses for a nine-cell balanced (a) and seven-cell unbalanced (b) CRLH transmission lines of the type depicted in Figure 3.27. Reprinted with permission from Ref. [3]; copyright 2006 by John Wiley.

Group at the University of Toronto (Canada) presented a realization of a CL-loaded CPW by using series gaps and shunt strips (see Fig. 3.29) [15]. This line was used as a backward leaky wave antenna (LWA), where the operating frequency was set in the fast wave region of the LH band. CRLH-based LWAs will be studied in Chapter 4.

To end this subsection, let us point out that CRLH transmission lines in multilayer vertical architectures have been reported [96], including realizations in low temperature co-fired ceramic (LTCC) technology [97]. The penalty of these vertically stacked CRLH lines is the need of multiple metal and dielectric layers. However, this approach has two inherent advantages: (1) small size and (2) the possibility of bandwidth enhancement, since it is possible to achieve significant series capacitances (C_L) and shunt inductances (L_L). To understand this later aspect, let us consider a balanced CRLH transmission line described by the model of Figure 3.20. From (3.51), considering $\omega_s = \omega_p = \omega_o$, it follows that wave propagation is delimited by the following angular frequencies:

$$\omega_{CL} = \omega_R \left(\sqrt{1 + \frac{\omega_o^2}{\omega_R^2}} - 1 \right) \tag{3.66a}$$

$$\omega_{CR} = \omega_R \left(\sqrt{1 + \frac{\omega_o^2}{\omega_R^2}} + 1 \right) \tag{3.66b}$$

Thus, bandwidth increases by increasing ω_R (i.e., $\Delta\omega = \omega_{CR} - \omega_{CL} = 2\omega_R$). This means that to achieve a wide CRLH band, L_R and C_R must be small, which leads to large values of C_L and L_L in order to set the transition frequency, ω_o, to the required value. From the point of view of filter theory, notice that the model of Figure 3.20 is also the canonical circuit of an order-3 bandpass filter. To achieve a wide filter bandwidth, it is necessary to use wideband series and shunt resonators, and this leads us to

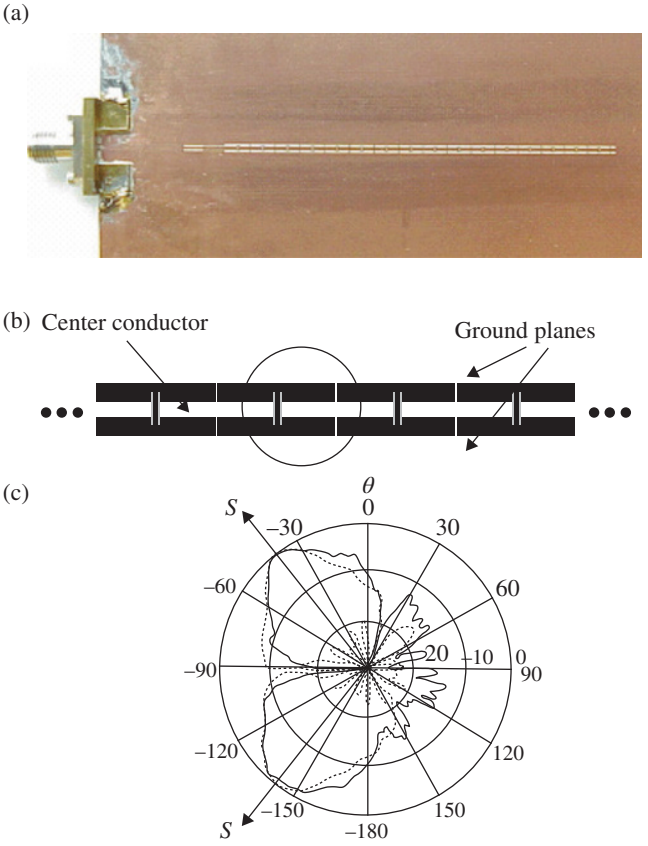

FIGURE 3.29 CPW CRLH transmission line leaky wave antenna (a). The detail of the structure and the radiation diagram are depicted in (b) and (c), respectively. Reprinted with permission from Ref. [15]. Copyright 2002, American Institute of Physics.

the same conclusion with regard to the values of C_L and L_L. The quasibalanced CRLH line reported in Ref. [97] (see Fig. 3.30) exhibits a bandwidth of 136%, whereas the unbalanced structure reported in Ref. [96] exhibits an LH band covering the range 0.2–0.6 GHz, that is, remarkable bandwidths as compared to those achievable with single-layered structures. The contributions of the Group of I. Vendik (St. Petersburg Electrotechnical University) to the design of compact broadband devices using LTCC technology and LH and RH transmission line sections are also remarkable (see, e.g., Ref. [98]).

To summarize, CRLH transmission lines consisting of a host line loaded with series capacitors and shunt inductors are described by the circuit model depicted in Figure 3.20 to a good approximation. In the next subsection, devoted to the resonant-type approach, the models of the reported CRLH lines present some modifications to the canonical model of 3.20, and will be discussed in detail.

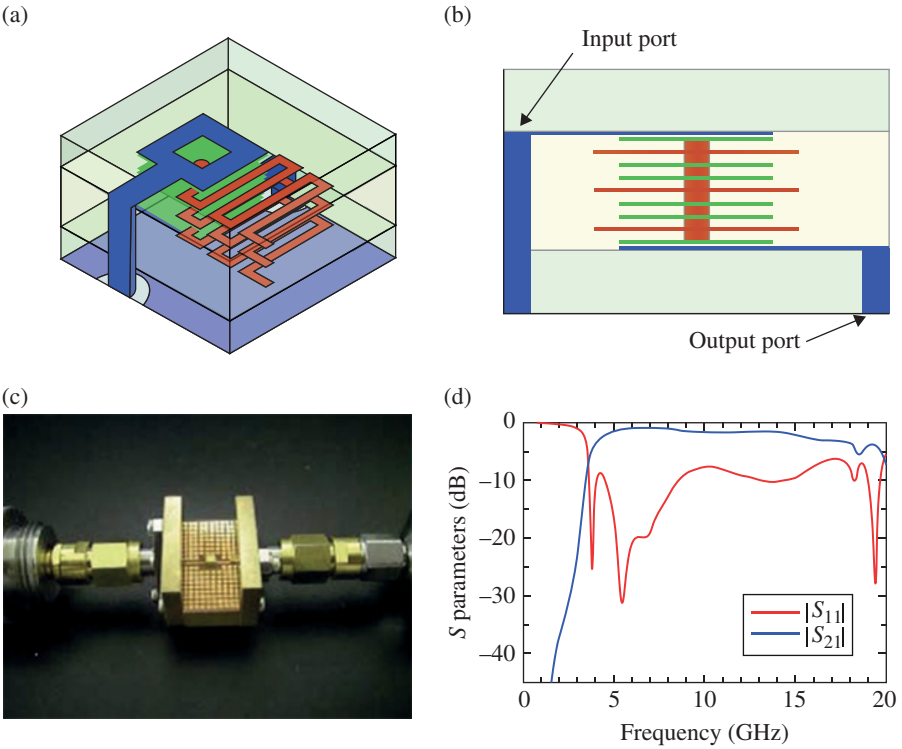

FIGURE 3.30 Three-dimensional view (a), side view (b), fabricated prototype (c), and frequency response (d) of a vertically stacked CRLH transmission line. Reprinted with permission from Ref. [97]. Copyright 2011 European Microwave Association.

3.5.2 Resonant-Type Approach

By resonant-type metamaterial transmission lines, we refer to the set of artificial lines where a host line is loaded with SRRs or other electrically small resonators (CSRRs, OSRRs, OCSRRs, etc.).[30] Notice, however, that the term given to this approach does not mean that the CL-loaded CRLH lines reviewed before are nonresonant (the canonical models of the CRLH lines presented in Section 3.4 clearly include series and parallel LC resonators). It has been argued that metamaterials based on split rings are narrow band and lossy due to the resonant nature of the constitutive elements (SRRs). Certainly, the first metamaterial structures described in Section 3.2, consisting of combinations of SRRs and metallic wires conveniently oriented, exhibit LH wave propagation in a narrow band. However, from this fact we cannot conclude that metamaterial transmission lines based on the resonant-type approach are intrinsically narrow band and lossy. Depending on the realizations, the LH band may be narrow, as

[30] Exception to this are the so-called hybrid lines, which can be considered to be a combination of the CL-loaded and resonant-type approach, and will be introduced in Section 3.5.3.

compared to CL-loaded lines; however, resonant-type balanced CRLH metalines can be designed to exhibit wide bandwidths, as will be shown later. Ultimately, the transmission bandwidths are dictated by the relations between the reactive elements of the circuit models. The achievable L/C ratios in SRR or CSRR based lines are limited, and these lines exhibit typically narrow LH bands. However, by combining open resonant particles (OSRRs and OCSRRs), CRLH lines with very wide bandwidths can be obtained, as will be demonstrated later. Very wideband bandpass filters, or moderate bandwidth bandpass filters with small insertion losses, based on CSRRs, have been reported as well. The applications of resonant-type metamaterial transmission lines will be studied in Chapter 4. Let us now discuss in detail the main approaches for their implementations and the specific circuit models.

3.5.2.1 Transmission Lines based on SRRs The first resonant-type metamaterial transmission line, based on SRRs [8], was designed as an attempt to mimic the first reported LH medium (depicted in Fig. 3.4) in planar technology. The considered host line was a CPW transmission line, loaded with pairs of SRRs (etched on the back substrate side) and shunt connected strips (Fig. 3.31). From the point of view of the effective constitutive parameters, the negative permeability is due to the SRRs, whereas the shunt-connected strips emulate the metallic wires of the wire medium, and therefore are responsible for the negative effective permittivity. In the structure of Figure 3.31, the pairs of SRRs are placed with their centers roughly aligned with the slots of the CPW. With this configuration, the magnetic flow lines generated by the host CPW can mostly "penetrate" the SRRs, and the particles can be magnetically excited. Hence, the CPW loaded only with SRRs behaves as a one-dimensional planar MNG medium in a narrow band just above the first SRR resonance frequency. Notice that in the structure of Figure 3.31, the SRRs are etched with their slits aligned in the direction orthogonal to the line axis and the shunt strips are allocated in the symmetry plane of the SRRs. This configuration avoids interactions between SRRs and strips [4]. Moreover, with this SRR orientation, the electric coupling between the CPW and the SRRs is cancelled, and the circuit model of the unit cell is simplified (the effects of particle rotation on the circuit model of the unit cell will be discussed later). Obviously, to implement an LH line, it is necessary that the cutoff frequency (plasma frequency) of the strip-loaded CPW is higher than the resonance frequency of the SRR, and this can be controlled by the distance between adjacent strips (period), and by the strip width, as discussed in Refs. [4, 8]. Notice that a CPW loaded only with strips can be described by the circuit model depicted in Figure 3.5, where L_s and C_s are the per-section line inductance and capacitance, and L is the inductance of the pair of parallel strips. The cutoff frequency is given by

$$\omega_c = \frac{1}{\sqrt{LC_s}} \tag{3.67}$$

Using the inductance value of the wire medium discussed in subsection 3.2.4.1 (expression 3.18) and $C_s = \varepsilon_o l$, the cutoff frequency (3.67) is identical to the plasma frequency given by (3.21). Therefore, there is a clear link between the one-dimensional wire medium and the strip-loaded CPW.

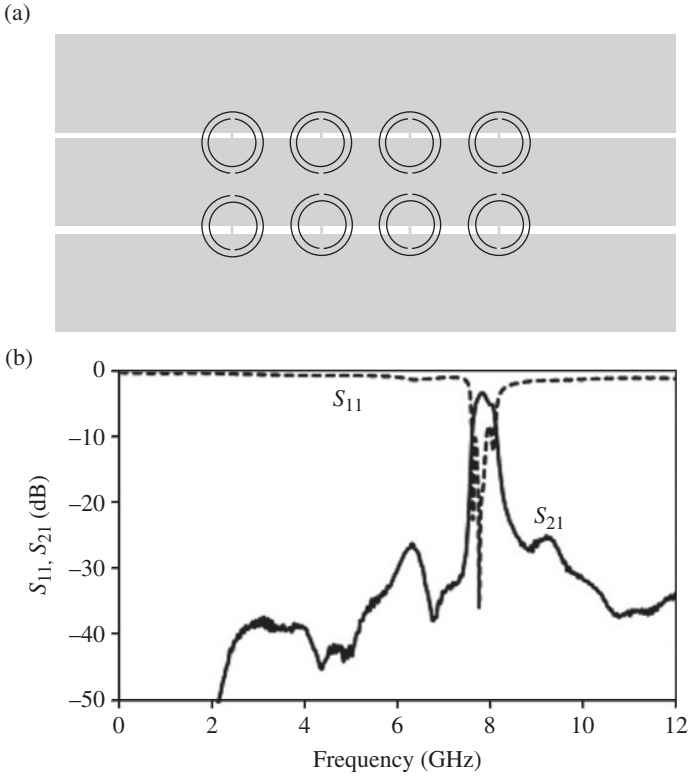

FIGURE 3.31 Layout (a) and measured frequency response (b) of a typical SRR/strip-loaded CPW. SRRs, etched on the back side of the substrate, are depicted in black, whereas the upper metal level is depicted in gray. Ring dimensions were determined following Refs [4, 99] to obtain a resonance frequency of $f_o = 7.7$ GHz, namely rings width and separation are $c = d =$ 0.2 mm, and the radius of the inner ring is $r = 1.3$ mm. The distance l between adjacent rings is 5 mm. Lateral CPW dimensions were calculated to obtain a 50 Ω characteristic impedance. Strip width is 0.2 mm. The considered substrate is the *Arlon 250-LX-0193-43-11* with $\varepsilon_r = 2.43$ and thickness $h = 0.49$ mm. Reprinted with permission from Ref. [8]. Copyright 2003, American Institute of Physics.

The frequency response of the SRR/strip-loaded CPW of Figure 3.31 is depicted in Figure 3.31b. A narrow transmission band, centered at roughly 8 GHz, can be appreciated. This pass band is an LH band as was demonstrated from full-wave EM simulations (not shown), and supported by the dispersion relation of the proposed lumped-element equivalent circuit model of the unit cell [4, 8]. The structure of Figure 3.31 is strongly unbalanced, but the geometry can be modified in order to narrow the gap present between the LH and the RH band (not present in the frequency range shown in Fig. 3.31b). Figure 3.32 depicts the SRR-loaded CPW without shunt strips and its frequency response. A stop band behavior, attributed to the negative effective permeability provided by the SRRs, is obtained in this case. Notice that

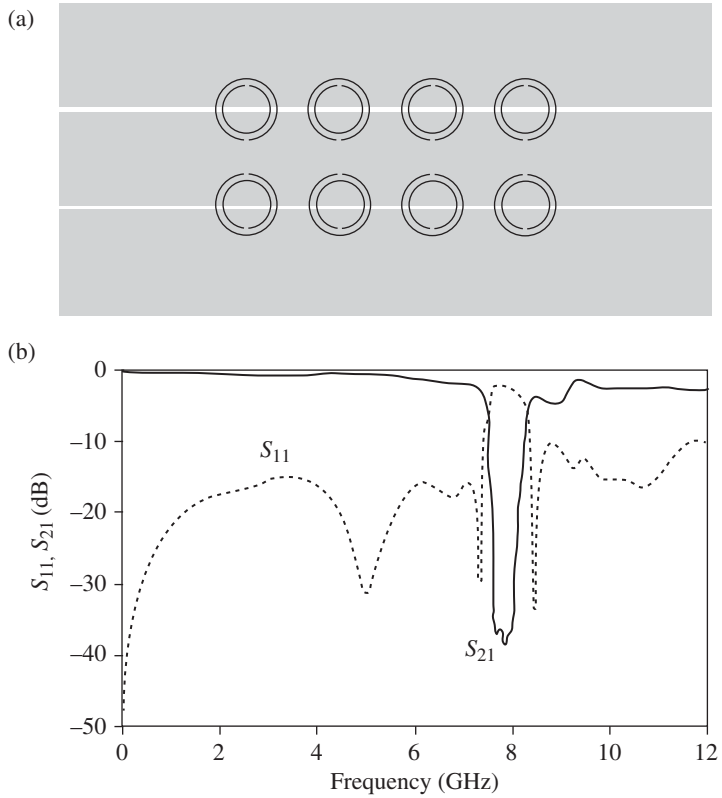

FIGURE 3.32 Layout (a) and measured frequency response (b) of an SRR-loaded CPW. The dimensions and substrate parameters are those of Figure 3.31. Reprinted with permission from Ref. [8]. Copyright 2003, American Institute of Physics.

the results of Figure 3.31b and 3.32b are conceptually similar to those reported in Figure 3.8a, as expected by virtue of the equivalence between the SRR/wire bulk media and SRR/strip-loaded CPWs.

Due to the presence of the SRRs, a transmission zero in the frequency response of both structures (with and without shunt strips) must be present. However, such transmission zero can be obscured by the noise floor level in multiple-cell structures. For this reason, in order to visualize the position of the transmission zero, it is convenient to obtain the frequency response in single-cell structures. Thus, Figure 3.33 depicts the insertion and return loss of a single-cell SRR-loaded CPW and SRR/strip-loaded CPW (both structures are depicted in the insets) [100]. As can be seen, the position of the transmission zeros (indicated in the figures) is different in both structures (the transmission zero frequency, f_z, is lower for the SRR/strip-loaded CPW). This shift in the transmission zero frequency is not obvious, and, indeed, in the first reported equivalent circuit models of the unit cell of the SRR-loaded and SRR/strip-loaded CPWs, such effect was ignored [8]. In other words, the formerly proposed models

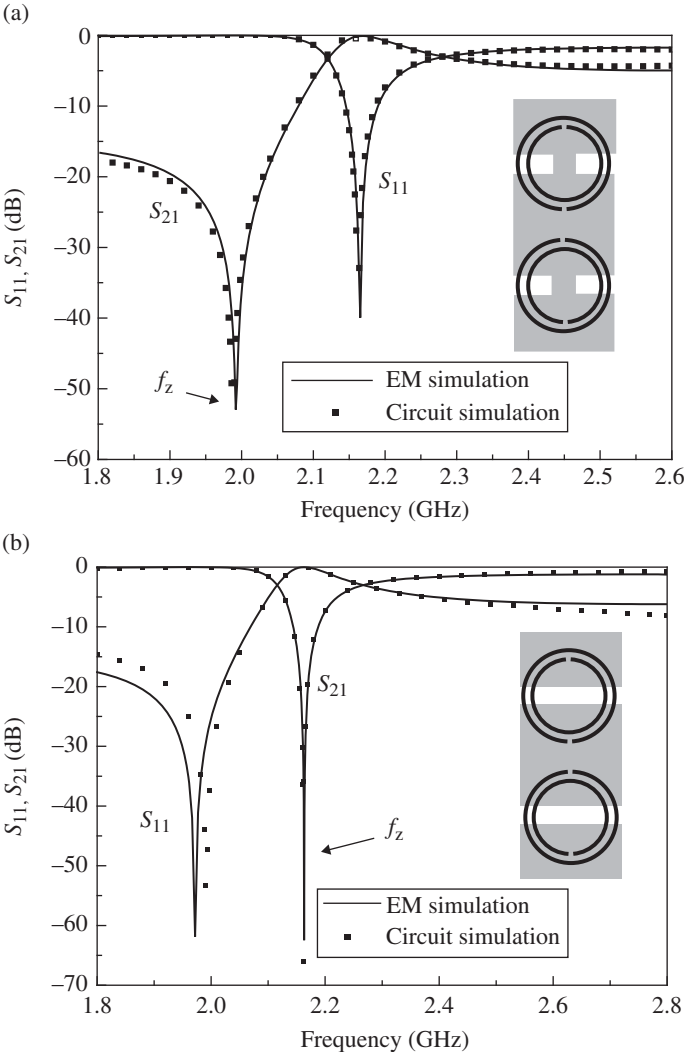

FIGURE 3.33 Simulated (through the *Agilent Momentum* commercial software) frequency responses of the unit cell structures shown in the insets. (a) CPW loaded with SRRs and shunt-connected strips and (b) CPW only loaded with SRRs. The response obtained from circuit simulation of the equivalent circuit model with extracted parameters (see Table 3.1) is also included. Dimensions are: the central strip width $W_c = 8$ mm, the width of the slots $G = 1.43$ mm, length of the line $D = 8$ mm, and the shunt strip width $w_s = 1.8$ mm. In all cases, the dimensions for the SRRs are: outer ring width $c_{out} = 0.364$ mm, inner ring width $c_{inn} = 0.366$ mm, distance between the rings $d = 0.24$ mm, and internal radius $r = 2.691$ mm. The considered substrate is *Rogers RO3010* with dielectric constant $\varepsilon_r = 10.2$ and thickness $h = 1.27$ mm. Reprinted with permission from Ref. [100]; copyright 2008 by Springer.

for these structures were not able to explain this different position of f_z. For this reason, the models were revised and improved in Ref. [101], and these latter models are those that are reported in detail in the next paragraph. Nevertheless, the first models of SRR-loaded and SRR-/strip-loaded CPW transmission lines are depicted in Figure 3.34 for completeness and for better comprehension of their limitations. Notice that the magnetic wall concept was applied to these models. L and C account for the line inductance and capacitance, respectively, C_s and L_s model the SRR, M is the mutual inductive coupling between the line and the SRRs (providing a mutual inductance of $2M$ after application of the magnetic wall—see the caption of Fig. 3.34), and L_p is the inductance of the shunt strips. The π-models of Figure 3.34a and b can be transformed to those depicted in Figure 3.34c and d, through the indicated transformations (see details in Ref. [4, 8]). For the SRR-/strip-loaded CPW, the model (Fig. 3.34c) is very similar to that of the

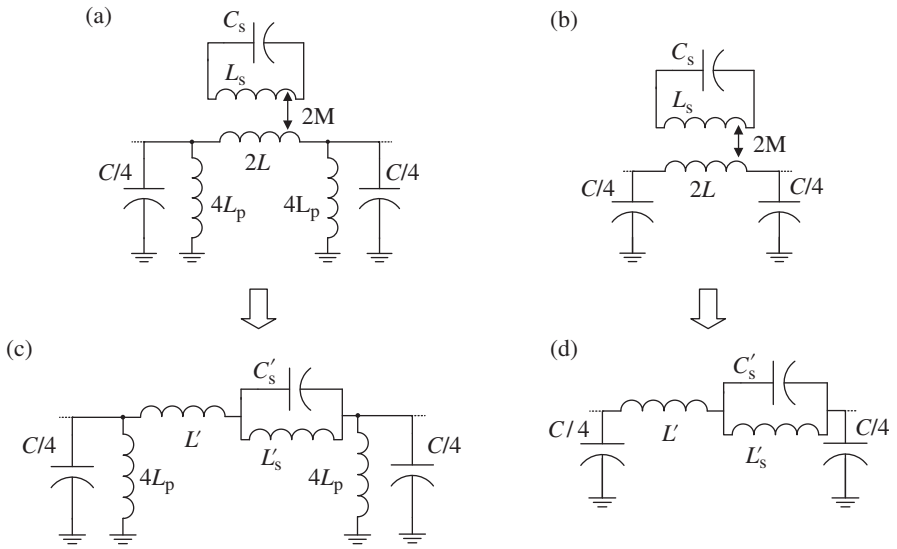

$$C'_s = \frac{L_s}{4M^2\omega_o^2} \qquad L'_s = 4M^2 C_s \omega_o^2$$

$$L' = 2L - L'_s \qquad \omega_o^2 = \frac{1}{L_s C_s} = \frac{1}{L'_s C'_s}$$

FIGURE 3.34 Lumped-element equivalent circuit for the basic cell of the SRR/strip-loaded CPW (a) and SRR-loaded CPW (b). These circuits can be transformed to those depicted in (c) and (d), according to the indicated transformations. In Refs. [4, 8], the inductance L' of the transformed models was approximated by $L' = 2L$, and the mutual inductance between the line and the SRR after application of the magnetic wall was considered to be M. This explains the difference between the indicated transformations and those in Refs. [4, 8]. However, in this book, the mutual inductance in (a) and (b) appears as $2M$ for coherence with the definition of M in the text and with the circuit of Figure 3.35.

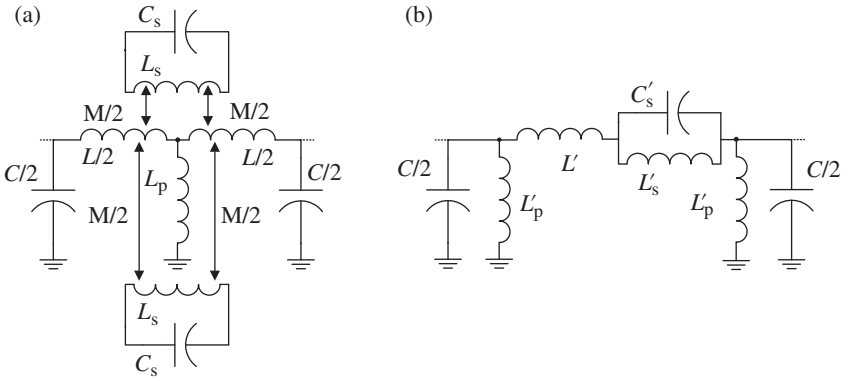

FIGURE 3.35 Improved circuit model for the basic cell of the SRR/strip-loaded CPW structure (a) and transformed model (b).

canonical order-2 CRLH transmission line model (Fig. 3.20).[31] The difference is the presence of the inductance L'_s, which is responsible for the transmission zero (given by the resonance frequency of the LC tank formed by L'_s and C'_s). However, the model of Figure 3.34d, corresponding to the SRR-loaded CPW has exactly the same series branch. Hence, according to these formerly proposed models, the transmission zeros of both structures should be present at the same frequency, which is not the case. Indeed, as will be seen later, the models of Figure 3.34c and d are formally correct. The difference is that the elements of the series branches of these models are different.

The improved model of the SRR-/strip-loaded CPW is depicted in Figure 3.35 [101]. Following Ref. [101], the magnetic wall concept has not been considered since this is not actually necessary. In this model, the reactive parameters have the same interpretation as in the models of Figure 3.34. However, the inductance of the shunt inductive strips, L_p, is now located between the two inductances ($L/2$) that model each line section, to the left and right of the position of the shunt strips. This improved model reflects the location of the inductive strips, as was reported in Ref. [102]. The model is neither a π-circuit nor a T-circuit. Thus the transmission zero frequency cannot be directly obtained from it. Due to symmetry considerations and reciprocity, the admittance matrix of the circuit of Figure 3.35a (which is a two-port) must satisfy $Y_{12} = Y_{21}$ and $Y_{11} = Y_{22}$. From these matrix elements, the equivalent π-circuit model can be obtained according to [103]:

$$Z_s(\omega) = -(Y_{21})^{-1} \tag{3.68a}$$

$$Z_p(\omega) = (Y_{11} + Y_{21})^{-1} \tag{3.68b}$$

[31] Notice that the unit cell of the canonical order-2 CRLH line of Figure 3.20 is a T-circuit. However, this line can also be obtained by cascading π-circuits comprising a series resonator L_R-C_L in the series branch and a parallel resonator $2L_L$-$C_R/2$ in the shunt branches. Such π-circuit is formally identical to the circuit of Figure 3.34(c) with the exception of the inductance L'_s.

Y_{21} is inferred by grounding the port 1 and obtaining the ratio between the current at port 1 and the applied voltage at port 2. Y_{11} is simply the input admittance of the two-port, seen from port 1, with a short-circuit at port 2. After a straightforward but tedious calculation, the elements of the admittance matrix are obtained, and by applying (3.68), we finally obtain

$$Z_s(\omega) = j\omega\left(2 + \frac{L}{2L_p}\right)\left[\frac{L}{2} + M^2\frac{1 + (L/4L_p)}{L_s\left(\left(\omega_o^2/\omega^2\right) - 1\right) - \left(M^2/2L_p\right)}\right] \tag{3.69a}$$

$$Z_p(\omega) = j\omega\left(2L_p + \frac{L}{2}\right) \tag{3.69b}$$

with $\omega_o = (L_s C_s)^{-1/2}$. Expression (3.69a) can be rewritten as follows:

$$Z_s(\omega) = j\omega\left[\left(2 + \frac{L}{2L_p}\right)\frac{L}{2} - L_s' + \frac{L_s'}{1 - L_s' C_s' \omega^2}\right] \tag{3.70}$$

with

$$L_s' = 2M^2 C_s \omega_o^2 \frac{\left(1 + (L/4L_p)\right)^2}{1 + \left(M^2/2L_p L_s\right)} \tag{3.71}$$

$$C_s' = \frac{L_s}{2M^2\omega_o^2}\left(\frac{1 + \left(M^2/2L_p L_s\right)}{1 + (L/4L_p)}\right)^2 \tag{3.72}$$

These results indicate that the improved circuit model of the unit cell of the SRR-/strip-loaded CPW (Fig. 3.35a) can be formally expressed as the π-circuit of Figure 3.34c, but with modified parameters (Fig. 3.35b). These modified parameters are related to the parameters of the circuit of Figure 3.35a, according to (3.71), (3.72) and

$$L' = \left(2 + \frac{L}{2L_p}\right)\frac{L}{2} - L_s' \tag{3.73}$$

$$L_p' = 2L_p + \frac{L}{2} \tag{3.74}$$

The transmission zero angular frequency, ω_z, for the circuit of Figure 3.35 is no longer given by the resonance frequency of the SRRs, ω_o, but it is smaller, that is, $\omega_z \le \omega_o$.

It is interesting to mention that the angular frequency where $\phi = \beta l = 0$, ω_s, obtained by forcing $Z_s(\omega) = 0$, that is,

$$\omega_s = \frac{1}{\sqrt{C_s(L_s - 2(M^2/L))}} \tag{3.75}$$

does not depend on the shunt inductance despite that $Z_s(\omega)$ is a function of L_p. This explains that ω_s is identical for both the SRR-loaded and SRR/strip-loaded CPW structures of Figure 3.33 (see Fig. 3.36; [100]).

According to this analysis, the previous reported circuit model of SRR/strip-loaded CPWs (Fig. 3.34c) is formally correct. The weakness relies on the physical interpretation of the elements of that model. These elements do not have any physical meaning (except C). However, they are related to the elements of the circuit model of Figure 3.35a, which describe the different components of the SRR/strip-loaded CPW.

The parameters of the circuit models for the structures of Figure 3.33 were extracted from the lossless EM simulations of their frequency responses, according to the procedure described in Appendix G [104] (see Table 3.1). The circuit of Figure 3.35b was considered for the SRR/strip-loaded CPW, whereas for the structure without shunt strips, the circuit model that results by forcing $L_p = \infty$ was considered. The circuit simulation of both circuits is also depicted in Figure 3.33 to ease the

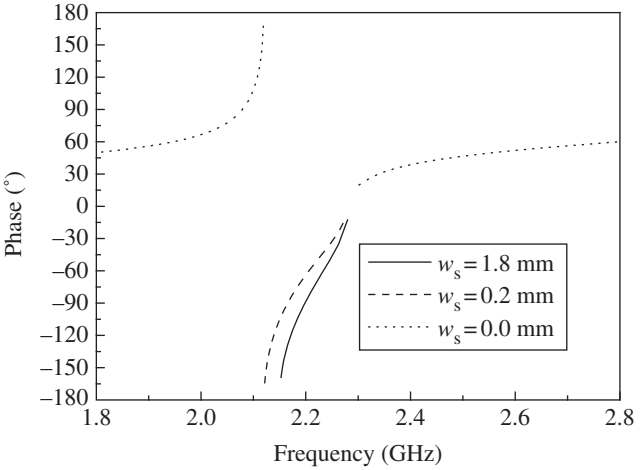

FIGURE 3.36 Phase response of the SRR-loaded ($w_s = 0$) and SRR/strip-loaded ($w_s = 1.8$ mm) CPW structures depicted in Figure 3.33. The phase response of an identical structure with strip widths of $w_s = 0.2$ mm is also included. The phase nulls at identical frequency in all the considered cases. Reprinted with permission from Ref. [100]; copyright 2008 by Springer.

TABLE 3.1 Extracted element parameters for the structures of Figure 3.33

	C (pF)	L' (nH)	L'_p (nH)	C'_s (pF)	L'_s (nH)
With shunt strips	2.07	4.91	1.38	3.90	1.68
Without shunt strips	2.07	1.91	—	23.01	0.24

TABLE 3.2 Parameters for the circuit shown in Figure 3.35a, obtained from Table 3.1

	C (pF)	L (nH)	M (nH)	L_p (nH)	C_s (pF)	L_s (nH)
With shunt strips	2.07	1.94	1.23	0.20	0.31	17.16
Without shunt strips	2.07	2.15	1.45	—	0.31	17.57

comparison with the EM simulation. The agreement is good, thus pointing out the validity of the model.

However, to further validate the proposed circuit model of SRR/strip-loaded CPWs, Equations (3.71)–(3.74) were inverted in order to obtain the parameters of the model of Figure 3.35a (from the results shown in Table 3.1), and these coincide in reasonable agreement with those parameters inferred in the structure without shunt strips (see Table 3.2), and obtained through the transformations indicated in Figure 3.34 (or (3.71)–(3.74) with $L_p = \infty$).[32] This means that the presence of the shunt strips does not affect the parameters of the structure, hence having a clear physical interpretation.

Interestingly, application of (3.45) and (3.46) to the model of Figure 3.35b with the element values given by (3.71)–(3.74) gives an effective permittivity and permeability of the form of expressions (3.22) and (3.34), respectively. Namely, the impedance of the series branch, given by (3.70), can be expressed as follows:

$$Z_s(\omega) = j\omega \left[\left(2 + \frac{L}{2L_p} \right) \frac{L}{2} + \frac{L_s'^2 C_s' \omega^2}{\left(1 - L_s' C_s' \omega^2\right)} \right] \tag{3.76}$$

and it can be simplified to

$$Z_s(\omega) = j\omega \left(2 + \frac{L}{2L_p} \right) \frac{L}{2} \left[1 + \frac{2L_s'}{L\left(2 + \left(L/2L_p\right)\right)} \frac{\omega^2}{\left(\omega_o'^2 - \omega^2\right)} \right] \tag{3.77}$$

where $\omega_o' = \omega_z = \left(L_s'\ C_s'\right)^{-1/2}$ is the transmission zero frequency. Using (3.45), the effective permeability is

$$\mu_{\text{eff}}(\omega) = \left(2 + \frac{L}{2L_p} \right) \frac{L}{2l} \left[1 - \frac{2L_s'}{L\left(2 + \left(L/2L_p\right)\right)} \frac{\omega^2}{\left(\omega^2 - \omega_o'^2\right)} \right] \tag{3.78}$$

[32] It is very easy to demonstrate that if the magnetic wall concept in the circuit of Figure 3.34 is not applied, the resulting transformations are identical to those given by (3.71)–(3.74) with $L_p = \infty$. However, the model of a SRR/strip-loaded CPW of Figure 3.34a is not correct. As discussed in the text, the model of Figure 3.35a must be considered to describe these lines.

and introducing (3.71) in (3.78), we obtain

$$\mu_{\text{eff}}(\omega) = \left(2 + \frac{L}{2L_{\text{p}}}\right)\frac{L}{2l}\left[1 - \frac{2M^2 C_{\text{s}}\omega_{\text{o}}^2\left(1 + \left(L/4L_{\text{p}}\right)\right)}{L\left(1 + \left(M^2/2L_{\text{p}}L_{\text{s}}\right)\right)}\frac{\omega^2}{\left(\omega^2 - \omega_{\text{o}}'^2\right)}\right] \tag{3.79}$$

The mutual inductance is a fraction of the line inductance, that is, $M = L{\cdot}f$. Therefore, (3.79) can be written in the following form:

$$\mu_{\text{eff}}(\omega) = \left(2 + \frac{L}{2L_{\text{p}}}\right)\frac{L}{2l}\left[1 - \frac{2Lf^2}{L_{\text{s}}}\frac{\left(1 + \dfrac{L}{4L_{\text{p}}}\right)}{\left(1 + \dfrac{M^2}{2L_{\text{p}}L_{\text{s}}}\right)}\frac{\omega^2}{\left(\omega^2 - \omega_{\text{o}}'^2\right)}\right] \tag{3.80}$$

which is formally identical to expression (3.34). Indeed, if we neglect the presence of the strips ($L_{\text{p}} \to \infty$), and consider that $L/l = \mu_{\text{eff}}(0)$, the effective permeability can be expressed as follows:

$$\mu_{\text{eff}}(\omega) = \mu_{\text{eff}}(0)\left[1 - 2\frac{\mu_{\text{eff}}(0)lf^2}{L_{\text{s}}}\frac{\omega^2}{\left(\omega^2 - \omega_{\text{o}}'^2\right)}\right] \tag{3.81}$$

Notice that losses have been neglected, and the inductance of the SRR, L_{s}, appears as L in (3.34). Thus, the single difference between (3.81) and (3.34) concerns the factor F and the DC effective permeability, different than μ_{o}. In fact, $\mu_{\text{eff}}(0)$ is the effective permeability of the host line (CPW) without the presence of the SRRs, defined as the per-unit-length inductance of the line, according to (3.45).

Concerning the permittivity, application of (3.46) to the parallel resonator of the shunt branch of the circuit of Figure 3.35b, directly gives a permittivity of the form (3.22), that is,

$$\varepsilon_{\text{eff}} = \frac{C}{l}\left(1 - \frac{\omega_{\text{p}}^2}{\omega^2}\right) \tag{3.82}$$

with $\omega_{\text{p}} = (L_{\text{p}}'\, C/2)^{-1/2}$. In (3.82), C/l is the effective permittivity of the structure at high frequencies ($\omega >> \omega_{\text{p}}$), or the effective permittivity of the CPW host line without the presence of the shunt strips. Thus, the equivalence between the SRR and wire medium of Figure 3.4 and the SRR/strip-loaded CPW has been demonstrated. Indeed, such equivalence was pointed out by Eleftheriades *et al.* [105] and by Solymar and Shamonina in their textbook [21].

Once the circuit model of the SRR/strip-loaded CPW has been expressed as a π-circuit, the dispersion relation and the characteristic impedance can be easily obtained. Application of (2.23) to the circuit of Figure 3.35b gives

$$\cos(\beta l) = 1 - \frac{1}{2} L' C \omega^2 \left(1 - \frac{\omega_p^2}{\omega^2}\right) \left(1 - \frac{1}{L' C_s' \omega^2 \left(1 - \omega_o'^2/\omega^2\right)}\right) \tag{3.83}$$

Notice that (3.83) can be reduced to (3.51) if $L_s' \to \infty$ (or $\omega_o' = 0$).[33] For a symmetric π-circuit, the characteristic impedance can be expressed as follows:

$$Z_B(\omega) = \sqrt{\frac{Z_s(\omega) Z_p(\omega)/2}{1 + \left(Z_s(\omega)/2Z_p(\omega)\right)}} \tag{3.84}$$

where Z_s and Z_p are the series and shunt impedances of the π-circuit, respectively. Therefore, the characteristic impedance is given by

$$Z_B(\omega) = \sqrt{\frac{L'}{C}\left(1 - \frac{\omega_p^2}{\omega^2}\right)^{-1} \left[\left(1 - \frac{1}{L' C_s' \omega^2 \left(1 - \left(\omega_o'^2/\omega^2\right)\right)}\right)^{-1} - \frac{CL'\omega^2}{4}\left(1 - \frac{\omega_p^2}{\omega^2}\right)\right]^{-1}} \tag{3.85}$$

In the limit $L_s' \to \infty$ (or $\omega_o' = 0$), expression (3.85) does not coincide with (3.52). The reason is that the characteristic impedance of a transmission line is different if it is described either by a cascade of symmetric π- or T-circuit unit cells. However, the dispersion relation is identical for both unit cells.

3.5.2.2 Transmission Lines based on CSRRs Since the CSRR is the negative image of the SRR and it can be driven (not exclusively) by an axial time-varying electric field, CSRR-based lines have been mainly implemented in microstrip technology by etching the CSRRs in the ground plane, beneath the conductor strip. In that region, there is a strong vertical electric field generated by the line, and the CSRR can be easily excited. The former artificial lines based on CSRRs were reported in Refs. [84, 85]. In Ref. [84], a microstrip line was loaded only with CSRRs, giving rise to a one-dimensional ENG medium, whereas the line reported in Ref. [85] was loaded with CSRR and series gaps. The series gaps provide the required negative permeability to achieve an LH medium. Figure 3.37 depicts the CSRR/gap-loaded microstrip structure reported in Ref. [85] and its frequency response, where a bandpass behavior in the LH band is obtained. For comparison purposes, the frequency response without the presence of the gaps is included, where a stop band functionality, attributed to the negative effective permittivity in the vicinity of the CSRR resonance frequency, is visible. Actually, the CSRR/gap-loaded lines exhibit a CRLH behavior. However, the RH band is beyond the frequency range shown in Figure 3.37.

[33] The expressions are identical if we identify the elements of the shunt and series branches (except L_s') of the circuit of Figure 3.35b with those of Figure 3.20.

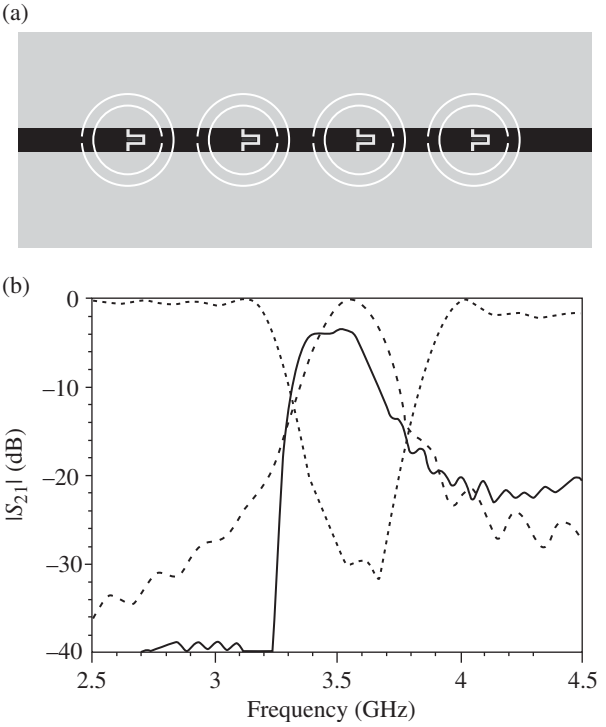

FIGURE 3.37 Layout (a) and insertion loss (b) of a CSRR/gap-loaded microstrip line. The EM simulation of the structure is represented by dashed line, whereas the measured response is represented by solid line. The simulated response without series gaps is also included and represented by dotted line. Substrate parameters are dielectric constant $\varepsilon_r = 10.2$ and thickness $h = 1.27$ mm. CSRR dimensions are $r_{ext} = 2.5$ mm and $c = d = 0.3$ mm. The strip width is $W = 1.2$ mm. Reprinted with permission from Ref. [85]. Copyright 2004, American Physical Society.

The former lumped-element equivalent circuit models of CSRR-loaded and CSRR/gap-loaded microstrip lines (unit cells) were reported in Ref. [10], and are depicted in Figure 3.38. According to Ref. [10], L and C are the per-section inductance and capacitance of the line, L_c and C_c model the CSRR, and C_g accounts for the capacitance of the series gaps. According to this interpretation of the circuit elements, the transmission zero, given by that frequency that nulls the shunt branch, that is,

$$f_z = \frac{1}{2\pi\sqrt{L_c(C + C_c)}} \tag{3.86}$$

should be independent of the characteristics of the series gap. However, it was found that the position of the transmission zero varies with gap dimensions and takes different values in CSRR-loaded microstrip lines with and without gaps (with identical line and CSRR dimensions) [100]. Notice that this behavior is similar to that of

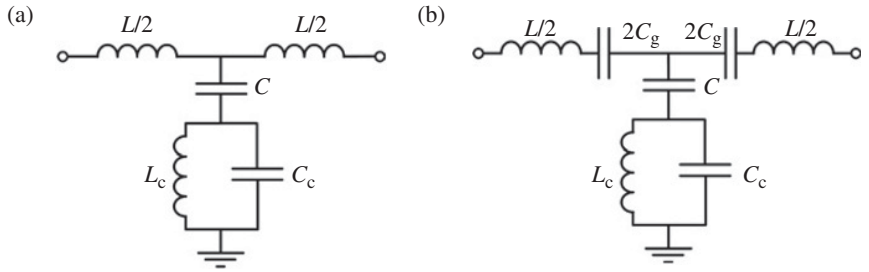

FIGURE 3.38 Formerly reported lumped-element equivalent circuits for the basic cell of the CSRR-loaded microstrip (a) and CSRR/gap-loaded microstrip (b) transmission lines.

SRR-loaded CPWs caused by variations in shunt-connected strip dimensions. Therefore, the models of the CSRR-based lines must be revised to account for the variation of the transmission zero frequency with gap dimensions.

Figure 3.39 depicts the layouts and frequency responses of two CSRR-loaded microstrip lines: one with series gap and the other one without it. The variation experienced by the transmission zero frequency is significant. The parameters of the models of Figure 3.38 were extracted (see Appendix G), and they are depicted in Table 3.3. Notice that the substantial variation in f_z is due to the strong variation of C. However, this cannot be attributed to the effects of the fringing capacitance of the gap.

There is no doubt that the models of Figure 3.38 accurately describe the EM response of the CSRR-based lines. However, the interpretation of the parameters as formerly reported in Ref. [10] is not correct. Neither C_g is actually the capacitance of the series gap, nor C is the line capacitance. A more realistic model of the structure is that depicted in Figure 3.40, where C_L is the line capacitance, C_f is the fringing capacitance of the gap and C_s is the series capacitance of the gap [106]. Obviously, from π-T transformation, the circuit model of Figure 3.38b, which is the previously reported model of microstrip lines loaded with CSRRs and series gaps, is obtained; but the values of C_g and C do not actually have a physical interpretation. Indeed, C_g and C can be expressed in terms of C_s and $C_{par} = C_f + C_L$ according to

$$C_g = 2C_s + C_{par} \tag{3.87}$$

$$C = \frac{C_{par}\left(2C_s + C_{par}\right)}{C_s} \tag{3.88}$$

Inspection of (3.88) indicates that as C_s decreases (gap distance increases), C increases. Indeed C can be made very large if C_s is sufficiently small. It is also apparent from (3.87) that despite the fact that the gap distance is increased, it is not expected that C_g experiences a significant reduction. The reason is that for small values of C_s, C_g is dominated by the line capacitance and the fringing capacitance (C_{par}). Such behavior of C and C_g was corroborated by considering several CSRR-loaded structures with identical geometry except in the gap distance [107]. This analysis reveals

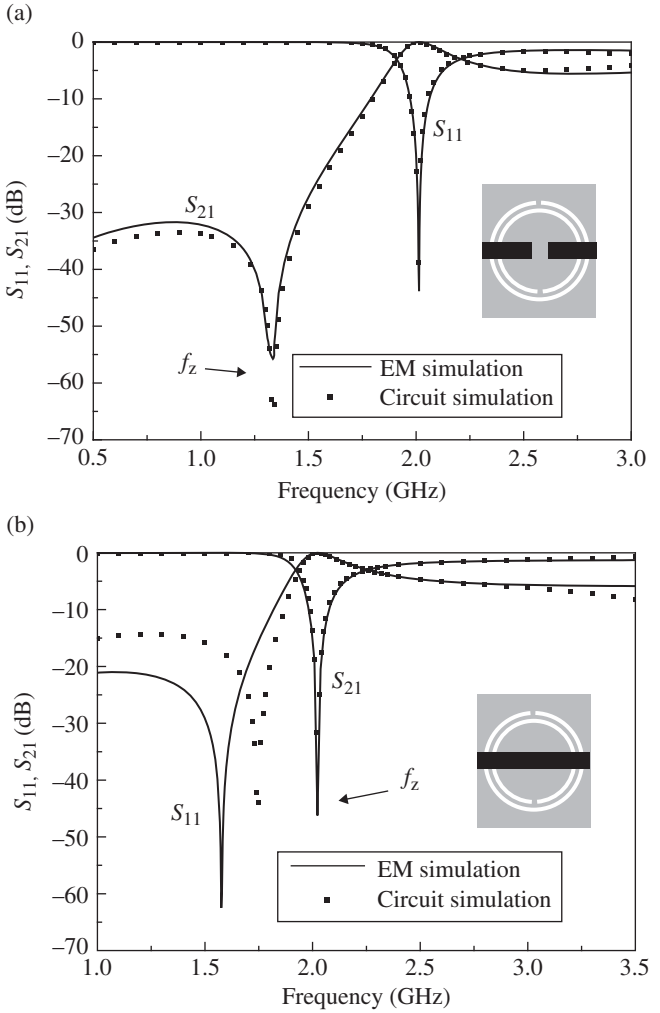

FIGURE 3.39 Simulated (through the *Agilent Momentum* commercial software) frequency responses of the unit cell structures shown in the insets. (a) Microstrip line loaded with CSRRs and series gaps and (b) microstrip line only loaded with CSRRs. The response obtained from circuit simulation of the equivalent model with extracted parameters is also included. Dimensions are: the strip line width $W_m = 1.15$ mm, the length $D = 8$ mm, and the gap width $w_g = 0.16$ mm. CSRRs dimensions: are outer ring width $c_{out} = 0.364$ mm, inner ring width $c_{inn} = 0.366$ mm, distance between the rings $d = 0.24$ mm, and internal radius $r = 2.691$ mm. The considered substrate is *Rogers RO3010* with dielectric constant $\varepsilon_r = 10.2$ and thickness $h = 1.27$ mm. Reprinted with permission from Ref. [100]; copyright 2008 by Springer.

TABLE 3.3 Extracted element parameters for the structures of Figure 3.39

	C (pF)	L (nH)	C_g (pF)	C_c (pF)	L_c (nH)
With series gap	6.43	5.78	0.31	3.10	1.49
Without series gap	0.95	5.78	—	2.81	1.65

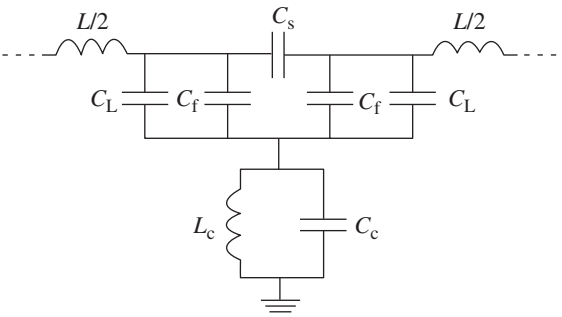

FIGURE 3.40 Improved circuit model for the basic cell of the CSRR/gap-loaded microstrip line.

that C can be enhanced by merely increasing the gap distance, without the penalty of a small C_g value (since C_f and C_L do also contribute to this capacitance—see expression (3.87)). These results are of interest because they reveal that it is possible to obtain high values of C (by decreasing C_s), regardless of the substrate thickness. These high values of C are typically necessary to drive the transmission zero frequency to small values.[34] Notice that in the limit $C \to \infty$, the model of Figure 3.38b is identical to the model of an order-2 CRLH transmission line.

The dispersion relation and the characteristic impedance of CSRR/gap-loaded lines is given by (2.33) and (2.30), that is,

$$\cos\beta l = 1 + \frac{\left(C/2C_g\right)\left(1-\left(\omega^2/\omega_s^2\right)\right)\left(1-\left(\omega^2/\omega_p^2\right)\right)}{\left(1-\left(\omega^2/\omega_p^2\right)-CL_c\omega^2\right)} \tag{3.89}$$

$$Z_B = \sqrt{\frac{L}{C_c}\frac{\left(1-\left(\omega_s^2/\omega^2\right)\right)}{\left(1-\left(\omega_p^2/\omega^2\right)\right)}-\frac{L^2\omega^2}{4}\left(1-\frac{\omega_s^2}{\omega^2}\right)^2+\frac{L}{C}\left(1-\frac{\omega_s^2}{\omega^2}\right)} \tag{3.90}$$

Notice that the characteristic impedance is similar to that corresponding to the order-2 CRLH transmission line model (expression 3.52). The difference is the presence of the third term in the square root of (3.90). However, this term vanishes if $C \to \infty$, since in

[34] Nevertheless, in certain applications, it might be convenient to allocate the transmission zero close to the first (LH) band, in order to reject undesired frequencies.

this case the models of Figures 3.20 and 3.38b are identical. In the limit $C \to \infty$, (3.89) coincides with (3.51).

Both SRR/strip-loaded CPW and CSRR/gap-loaded microstrip lines exhibit a CRLH behavior. These lines can be balanced by merely forcing the series and shunt resonance frequencies to be identical. In particular, for CSRR/gap-loaded lines, the balanced condition is expressed as follows:

$$\omega_{\mathrm{s}} = \frac{1}{\sqrt{LC_{\mathrm{g}}}} = \frac{1}{\sqrt{L_{\mathrm{c}}C_{\mathrm{c}}}} = \omega_{\mathrm{p}} = \omega_{\mathrm{o}} \tag{3.91}$$

where ω_{o} is the transition frequency.[35] Under the balance condition, the characteristic impedance is given by

$$Z_{\mathrm{B}} = \sqrt{\frac{L}{C_{\mathrm{c}}} - \frac{L^2\omega^2}{4}\left(1 - \frac{\omega_{\mathrm{o}}^2}{\omega^2}\right)^2 + \frac{L}{C}\left(1 - \frac{\omega_{\mathrm{o}}^2}{\omega^2}\right)} \tag{3.92}$$

The frequency dependence of the characteristic impedance in a balanced CSRR/gap-loaded microstrip line is similar to that of a canonical order-2 CRLH line (Fig. 3.22b). Namely, the characteristic impedance is real in the allowed band (including the LH and the RH bands), it goes to zero at the extremes of the band, and it is imaginary in the forbidden bands. However, the maximum value of the characteristic impedance in CSRR/gap-loaded microstrip lines appears at a frequency slightly above the transition frequency, as can be appreciated in Figure 3.41.

In order to balance a CSRR-based line, relatively large values of C_{g}, or C_{s}, are typically necessary. Interdigital capacitors are thus an alternative to series gaps to implement the series capacitances. Figure 3.42 depicts the layout of a balanced unit cell, as well as the dispersion diagram and frequency response [108]. Actually, the structure is slightly unbalanced (see the dispersion diagram inferred from measurement), but the frequency response does not exhibit an appreciable gap between the LH and the RH bands (i.e., the transition between both bands is continuous). The agreement between the EM simulation (or measurement) and the circuit (electrical) simulation is good up to frequencies above the CSRR resonance (transition frequency). At sufficiently high frequencies (above 2 GHz), the discrepancy between the circuit and EM simulation is due to the fact that the circuit model (Fig. 3.38b) is no longer valid.

It is interesting to mention that there are clear similarities between the CSRR-based microstrip lines and SRR-based CPWs. Both lines exhibit a CRLH behavior, and the transmission zero frequency depends on the gap (for CSRR-based lines) or shunt strip (for SRR-based lines) geometry. With regard to the effective constitutive parameters, the permeability and permittivity follow the Lorentz and Drude models, respectively, for SRR-based lines, and the opposite models for CSRR-based lines. Indeed, the models of Figures 3.35b and 3.38b are circuit duals, in the sense that the series impedance

[35] Notice that in Section 3.5.2.1, ω_{o} was used to designate the intrinsic resonance frequency of the SRR.

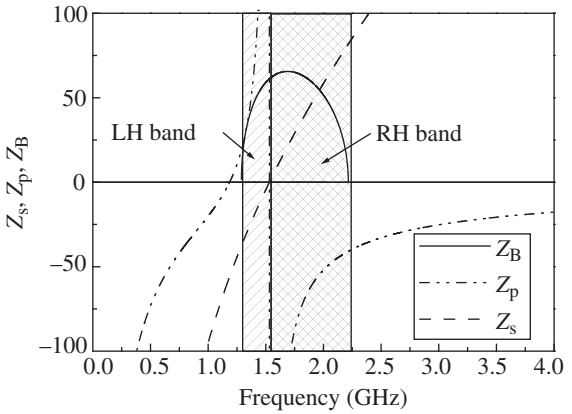

FIGURE 3.41 Representation of the series, Z_s, shunt, Z_p and characteristic impedance, Z_B, for a CRLH transmission line corresponding to the model of a balanced CSRR-based structure. The depicted values of Z_s and Z_p are actually the reactances. The transition frequency was set to roughly $f_o = 1.5$ GHz. Reprinted with permission from Ref. [108]; copyright 2007 IEEE.

of one circuit is inversely proportional to the shunt impedance of the other, as occurs in physical dual structures [83].[36] Although SRR-based CPWs and CSRR-based microstrip lines are not dual structures, they can be considered roughly duals [109].

3.5.2.3 Inter-Resonator Coupling: Effects and Modeling In the circuit models of the SRR- and CSRR-based lines of the preceding subsections the coupling between adjacent resonators has been neglected. This approximation can be made as long as the resonators are sufficiently separated and circular geometries are used. However, in SRR- or CSRR-based lines with closely located square or rectangular-shaped resonators, the effects of coupling cannot be neglected, and the models must be modified to account for inter-resonator coupling. As will be shown, inter-resonator coupling broadens the stop band (in single negative structures) or the pass band (in CRLH lines). Let us see in the next paragraphs the reason for such bandwidth enhancement, and the rich phenomenology associated to the lines with inter-resonator coupling, where multimode propagation, including the presence of complex modes,[37] arises [116]. The study is focused on CSRR-loaded microstrip lines only (the analysis of SRR-loaded CPWs is similar and is reported in Ref. [117]).

[36] According to Ref. [83], an impedance Z_1 representing an element in a planar circuit is inversely proportional to the impedance Z_2 of the corresponding element in its physical dual.

[37] Complex waves are modes that may appear in lossless structures that have complex propagation constants (despite the absence of losses) [110]. These modes appear as conjugate pairs in reciprocal lossless structures, and they carry power in opposite directions so that if the two modes are excited with the same amplitude, they do not carry net power [111]. Complex waves have been found in several structures, such as dielectrically loaded waveguides [112], finlines [113], shielded microstrip structures [114], and, more recently, in shielded mushroom-type Sievenpiper structures [115], among others.

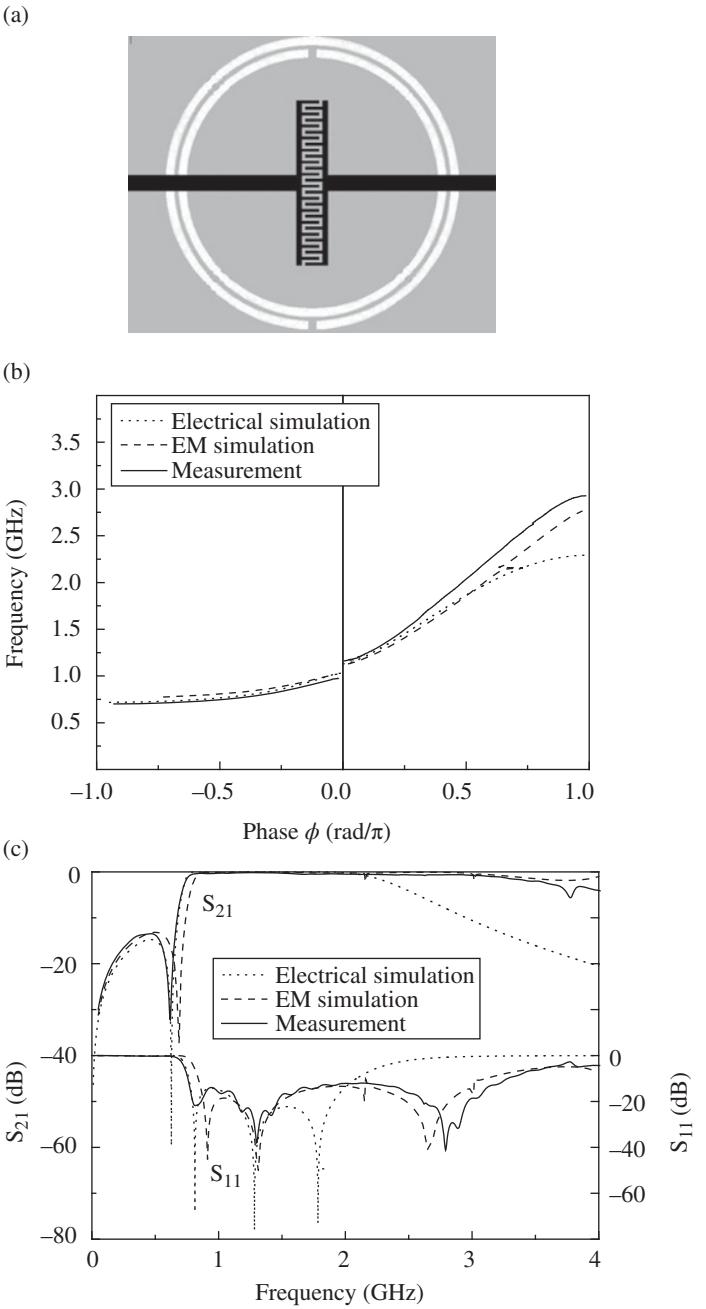

FIGURE 3.42 Balanced CRLH cell based on a microstrip line loaded with a CSRR and an interdigital capacitor (a), dispersion diagram (b), and frequency response (c). The structure was implemented in the *Rogers RO3010* substrate with dielectric constant $\varepsilon_r = 10.2$ and thickness $h = 1.27$ mm. Dimensions are: line width $W = 0.8$ mm, external radius of the outer ring $r = 7.3$ mm, rings width $c = 0.4$ mm, and ring separation $d = 0.2$ mm; the interdigital capacitor, formed by 28 fingers separated 0.16 mm, was used to achieve the required capacitance value. Reprinted with permission from Ref. [108]; copyright 2007 IEEE.

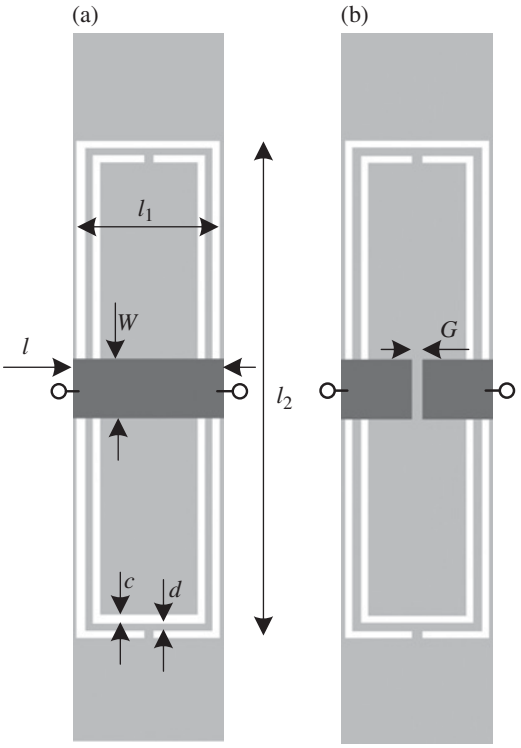

FIGURE 3.43 Unit cells of a CSRR-loaded (a) and CSRR/gap-loaded (b) microstrip line with rectangular-shaped resonators. The ground plane is depicted in light gray. Dimensions are: $W = 1.17$ mm, $l = 3$ mm, $c = d = 0.15$ mm, $l_1 = 2.8$ mm, $l_2 = 9.8$ mm, and $G = 0.2$ mm. The considered substrate is the Rogers *RO3010* with thickness $h = 1.27$ mm, dielectric constant $\varepsilon_r = 10.2$, and loss tangent tan $\delta = 0.0023$.

Let us consider CSRR-loaded microstrip lines with rectangular CSRRs. To favor inter-resonator coupling the longer side of the CSRR is orthogonal to the line axis, as depicted in Figure 3.43. The lumped-element circuit models of these structures, including electric coupling between adjacent resonators, are depicted in Figure 3.44 (the first neighbor approximation for inter-resonator coupling is considered and losses are neglected). Notice that the circuit models of these CSRR- and CSRR/gap-loaded lines are derived from those depicted in Figure 3.38 by simply adding the coupling capacitances C_R. The resulting models are thus four-port networks that can be cascaded to describe multi-section CSRR- or CSRR/gap-loaded lines.

The dispersion characteristics of these CSRR-loaded lines can be inferred from Bloch mode theory applied to the circuits of Figure 3.44. These circuits are multiport networks, and thus we can appeal to multiconductor line theory [118] in order to

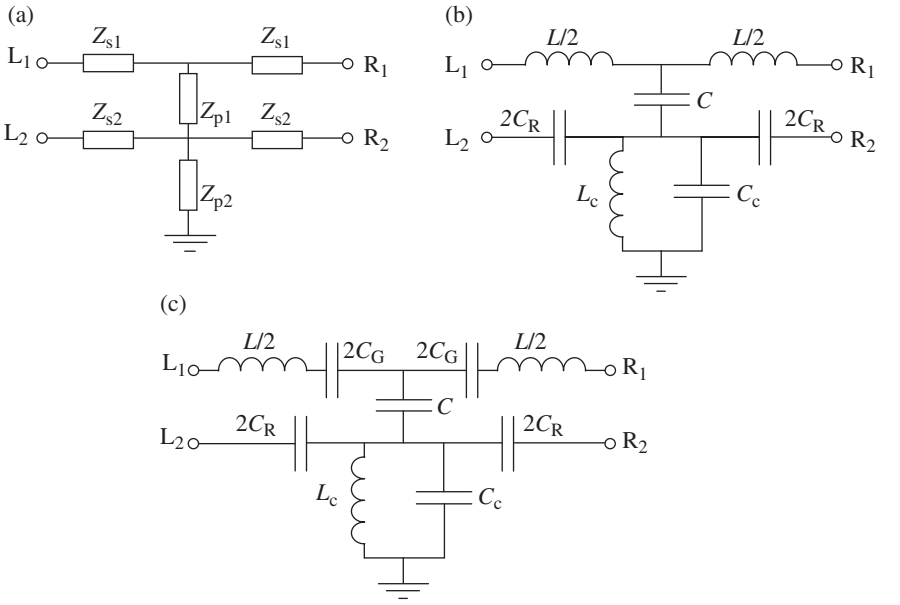

FIGURE 3.44 Equivalent circuit model of the structures of Figure 3.43, including inter-resonator coupling. (a) Generalized impedance model, (b) CSRR-loaded microstrip line model, and (c) CSRR/gap-loaded microstrip line model.

obtain the eigenmodes of the structure, and hence the propagation constants. Let us denote V_{L1}, V_{L2}, I_{L1}, and I_{L2} as the voltages and currents at the ports (1 and 2) of the left-hand side (subscript L) of the unit cell, and V_{R1}, V_{R2}, I_{R1}, and I_{R2} the variables at the right-hand side ports. The variables at both sides of the network are linked through a generalized order-4 transfer matrix, according to

$$\begin{pmatrix} \boldsymbol{V}_{\mathrm{L}} \\ \boldsymbol{I}_{\mathrm{L}} \end{pmatrix} = \begin{pmatrix} \boldsymbol{A} & \boldsymbol{B} \\ \boldsymbol{C} & \boldsymbol{D} \end{pmatrix} \begin{pmatrix} \boldsymbol{V}_{\mathrm{R}} \\ \boldsymbol{I}_{\mathrm{R}} \end{pmatrix} \tag{3.93}$$

where $\boldsymbol{V_L}$, $\boldsymbol{I_L}$, $\boldsymbol{V_R}$, and $\boldsymbol{I_R}$ are column vectors composed of the pair of port variables, and $\boldsymbol{A}$, $\boldsymbol{B}$, $\boldsymbol{C}$, and $\boldsymbol{D}$ are order-2 matrices. The dispersion relation is obtained from the eigenmodes of the system (3.93), that is

$$\det \begin{pmatrix} \boldsymbol{A} - e^{\gamma l} \cdot \boldsymbol{I} & \boldsymbol{B} \\ \boldsymbol{C} & \boldsymbol{D} - e^{\gamma l} \cdot \boldsymbol{I} \end{pmatrix} = 0 \tag{3.94}$$

where $\boldsymbol{I}$ is the identity matrix, the phase-shift factor $\mathrm{e}^{\gamma l}$ is the eigenvalue, $\gamma = \alpha + j\beta$ is the complex propagation constant, and l is the unit cell length. For reciprocal,

lossless and symmetric networks, the eigenvalues can be simplified to the solutions of [119, 120]:

$$\det(\boldsymbol{A} - \cosh(\gamma l)\cdot\boldsymbol{I}) = 0 \tag{3.95}$$

which gives

$$\cosh(\gamma l) = \frac{1}{2}\left(A_{11} + A_{22} \pm \sqrt{(A_{11} - A_{22})^2 + 4A_{12}A_{21}}\right) \tag{3.96}$$

where the elements of the $\boldsymbol{A}$ matrix (inferred from the network of Fig. 3.44a) are

$$\mathbf{A} = \mathbf{D}^t = \begin{pmatrix} 1 + \dfrac{Z_{s1}}{Z_{p1}} & -\dfrac{Z_{s1}}{Z_{p1}} \\ -\dfrac{Z_{s2}}{Z_{p1}} & 1 + \dfrac{Z_{s2}}{Z_{p1}} + \dfrac{Z_{s2}}{Z_{p2}} \end{pmatrix} \tag{3.97}$$

Since the network is lossless, the elements of $\boldsymbol{A}$ (A_{ij}) are real numbers. Hence, if the radicand of the square root in (3.96) is positive, the propagation constant is either purely real ($\alpha \neq 0, \beta = 0$) or purely imaginary ($\alpha = 0, \beta \neq 0$), corresponding to evanescent or propagating modes, respectively. However, if the radicand in (3.96) is negative, the two solutions are of the form $\gamma = \alpha \pm j\beta$, corresponding to complex modes. In order to obtain the frequency band that supports complex modes, the radicand in (3.96) is forced to be negative, that is:

$$\left(\frac{Z_{s1} - Z_{s2}}{Z_{p1}} - \frac{Z_{s2}}{Z_{p2}}\right)^2 + 4\frac{Z_{s1}Z_{s2}}{Z_{p1}^2} < 0 \tag{3.98}$$

According to (3.98) a necessary (although not sufficient) condition to have complex modes is an opposite sign for the reactances of Z_{s1} and Z_{s2}.

Let us first evaluate the dispersion relation of the CSRR-loaded line of Figure 3.43a, for which the pair of modal propagation constants given by expression (3.96) is depicted in Figure 3.45. In the first allowed band, there is a region with bivalued propagation constant; one (forward) corresponding to transmission-line type propagation, and the other (backward) related to electroinductive waves[38] [121]. Then, a region with conjugate modes (complex modes) appears, followed by a region with $\beta = 0$ and $\alpha \neq 0$ for both modes (evanescent waves). Finally, a forward wave

[38] Electroinductive waves (EIWs) may appear in chains of coupled CSRRs and are backward waves. They are similar to the magnetoinductive waves (MIWs) that may arise in chains of magnetically coupled coplanar SRRs [21]. EIW and MIW transmission lines will be studied in detail in Chapter 6.

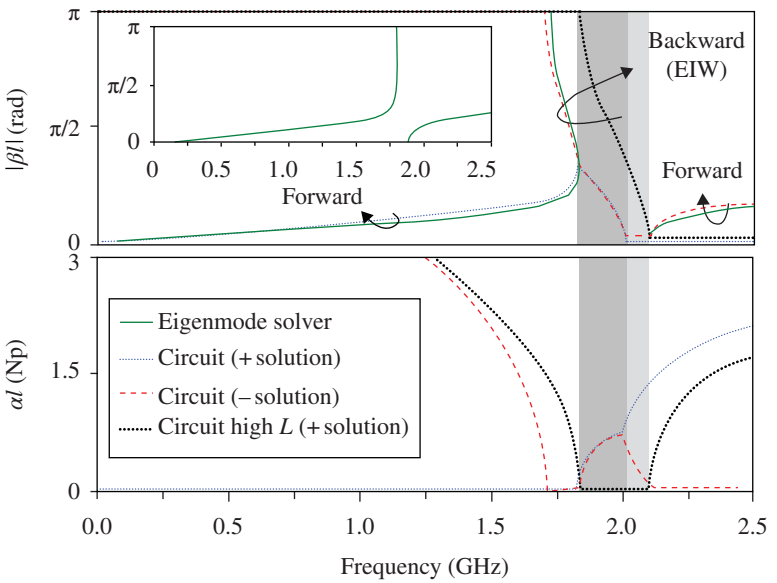

FIGURE 3.45 Dispersion relation for the structure of Figure 3.43a and for its equivalent circuit model of Figure 3.44b. The circuit parameters are: $L = 3.05$ nH, $C = 0.55$ pF, $L_c = 2.03$ nH, $C_c = 2.84$ pF, and $C_R = 0.21$ pF. The dispersion relation for the structure of Figure 3.43a with $l = 4.8$ mm is depicted in the inset. Notice that the eigenmode solver is not able to provide the complex modes (dark gray region) since these modes do not carry net power. The evanescent modes region is indicated in light gray. Reprinted with permission from Ref. [116]; copyright 2012 IEEE.

transmission band emerges again. It is apparent that the stop band characteristics in the complex wave region can be interpreted as a result of the antiparallelism between the transmission-line type (forward) and the electroinductive (backward) modes. To demonstrate the electroinductive nature of one of the modes in the upper region of the first allowed band, a large value of series inductance ($L \to \infty$, corresponding to an extremely narrow line) was considered, and the corresponding dispersion relation was inferred and depicted in Figure 3.45. According to this result, the nature of the aforementioned electroinductive waves is clear (the frequency shift is simply due to the fact that for the high-L case, the electroinductive waves propagate entirely through the inter-resonator capacitances).

The dispersion relation of a periodic structure composed of the cascaded unit cells of Figure 3.43a obtained by means of the eigenmode solver of *CST Microwave Studio* is also plotted in Figure 3.45. The agreement with the dispersion relation inferred from the circuit model is very good. The eigenmode solver was also used to obtain the dispersion relation that results after increasing the unit cell size to $l = 4.8$ mm (which corresponds to an increase in inter-resonator distance from 0.2 to 2 mm). For this inter-resonator distance (see the inset of Fig. 3.45), the electroinductive and complex modes are not present, and the fractional bandwidth of the stop band

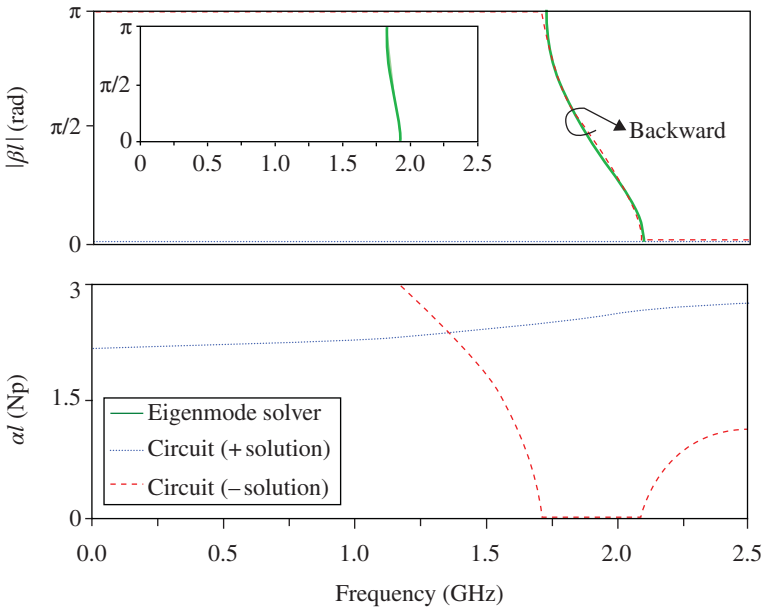

FIGURE 3.46 Dispersion relation for the structure of Figure 3.43b and for its equivalent circuit model of Figure 3.44c. The circuit parameters are: $L = 3.05$ nH, $C = 1.4$ pF, $L_c = 2.02$ nH, $C_c = 2.83$ pF, $C_G = 0.2$ pF, and $C_R = 0.23$ pF. The dispersion relation for the structure of Figure 3.43b with $l = 4.8$ mm is depicted in the inset. Reprinted with permission from Ref. [116]; copyright 2012 IEEE.

is reduced from 13.3 to 5.5%. These results indicate that, by reducing the distance between adjacent resonators, the forbidden band is enhanced due to the presence of complex modes, which do not carry net power and expand the stop band beyond the evanescent modes region.

The dispersion diagram for the structure of Figure 3.43b is depicted in Figure 3.46. As expected, a backward wave transmission band is obtained (the structure is unbalanced and the forward wave transmission band is above the depicted frequency range). The bandwidth in the first LH band broadens as inter-resonator coupling increases since electroinductive waves aid backward wave propagation.

The effects of inter-resonator coupling on bandwidth broadening are illustrated by comparing the frequency response of two order-9 CSRR-loaded stop band structures. One of them was fabricated by cascading the unit cells of Figure 3.43a, whereas the other one was fabricated with a larger unit cell size ($l = 4.8$ mm) in order to minimize inter-resonator coupling. The fabricated structures as well as their frequency responses are depicted in Figure 3.47. The agreement with the responses that result from the circuit models with the indicated parameters is good, and it is clear that bandwidth is enhanced by reducing the distance between adjacent resonators. Obviously, the stop band for the structure of Figure 3.47a coincides with the stop band predicted by the eigenmode analysis to a good approximation.

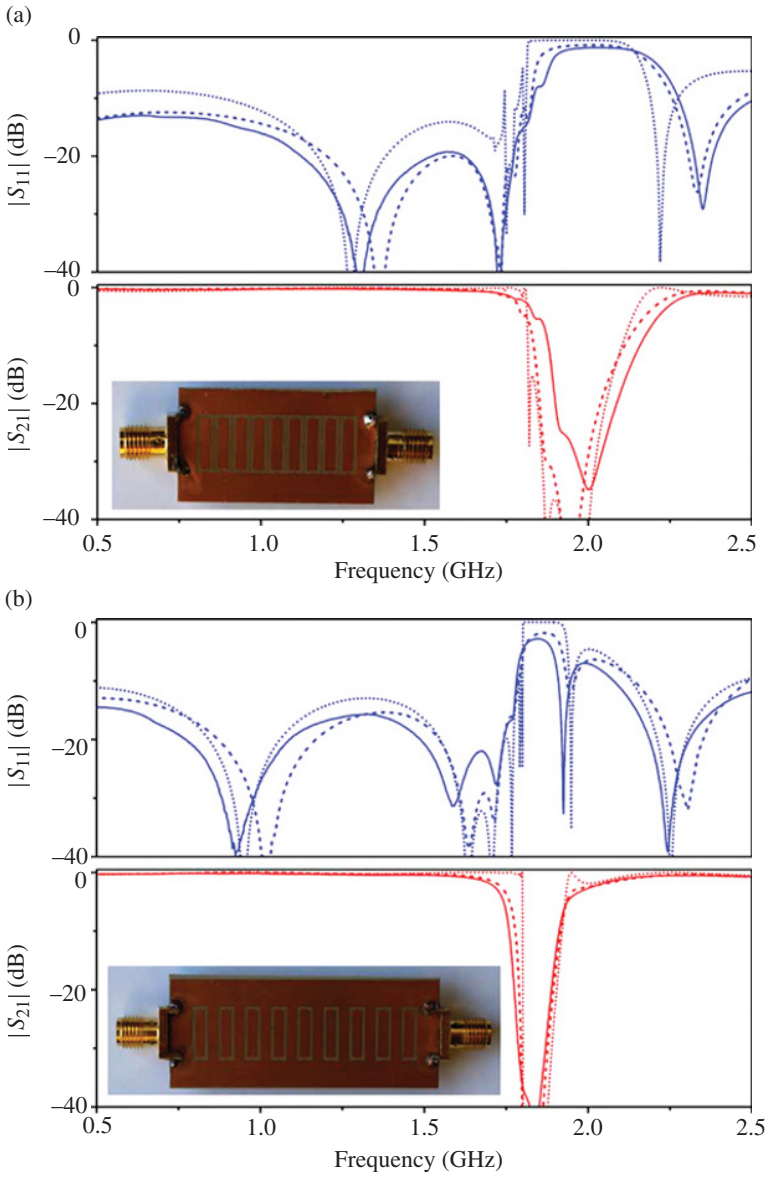

FIGURE 3.47 Measurement (solid line), lossy EM simulation (dashed line), and circuit simulation (dotted line) of the transmission and reflection coefficients of the CSRR-loaded structures shown in the insets (only the bottom face is shown). (a) $l = 3$ mm, the circuit parameters being those indicated in Figure 3.45; (b) $l = 4.8$ mm, the circuit parameters being those indicated in Figure 3.45, except $C_R = 0.017$ pF and $C_c = 3.2$ pF. To better fit the measurement in (b), a transmission line section of length 1.8 mm was cascaded between consecutive Z_{s1} in the circuit model. Reprinted with permission from Ref. [116]; copyright 2012 IEEE.

3.5.2.4 Effects of SRR and CSRR Orientation: Mixed Coupling The lumped-element equivalent circuit models of the SRR- and CSRR-based lines reported in the previous subsections are symmetric, that is, they are identical seen from both ports. Therefore, they must describe symmetric structures. Actually, the models of Figures 3.34, 3.35, 3.38, 3.40, and 3.44 are not valid for arbitrary orientation of the SRRs or CSRRs.[39] These models accurately describe the unit cells for SRRs or CSRRs oriented with the slits etched in a plane orthogonal to the line axis, corresponding to symmetric unit cells ($\phi = 0^\circ$ orientation). Under this SRR/CSRR orientation, the coupling between the line and the resonator is purely magnetic/electric. Though SRRs/CSRRs exhibit cross-coupling effects, they cannot be electrically/magnetically excited for this orientation since there is not a net component of the electric/magnetic field generated by the line in the direction orthogonal to the slits plane. However, if the SRRs/CSRRs are rotated ($\phi \neq 0^\circ$), the structures are no longer symmetric, and mixed coupling (electric and magnetic) between the line and the resonators arises. Such mixed coupling must be included in the circuit models for an accurate description of the SRR- or CSRR-based lines under arbitrary particle orientation [122].

Figure 3.48 depicts the frequency response of an SRR-loaded CPW with the SRRs oriented with an angle of $\phi = 90^\circ$ (i.e., with the symmetry planes of the SRRs parallel to the symmetry plane of the line). Notice that the asymmetry leads to substantially different phase of the reflection coefficients S_{11} and S_{22} (even though $|S_{11}| = |S_{22}|$ and the transmission coefficients satisfy $S_{12} = S_{21}$, as results from unitarity and reciprocity). The same phenomenology applies to a CSRR-loaded microstrip line (see Fig. 3.49). To gain insight on the effects of SRR or CSRR rotation on the frequency response of the structures, let us consider the non-bianisotropic SRR (NB-SRR) and the non-bianisotropic CSRR (NB-CSRR). These particles do not exhibit cross polarization since they have inversion symmetry with regard to their center, and this prevents the appearance of the electric and magnetic dipole for the SRR and CSRR, respectively, in the plane of the particles. According to this, it is expected that CPW and microstrip lines loaded with NB-SRRs and NB-CSRRs, respectively, are insensitive to particle rotation. This was verified from EM simulation by considering two different rotation angles (Figs. 3.50 and 3.51). As can be seen, the frequency response does not change appreciably by rotating the NB-SRRs and NB-CSRRs. Moreover, the responses of the SRR- and CSRR-loaded lines for $\phi = 0^\circ$ present the same pattern (unlike for $\phi = 90^\circ$) as those of the lines loaded with NB-SRRs and NB-CSRRs.

The previous results support the hypothesis that the dependence of the EM behavior of the SRR- and CSRR-loaded lines on particle orientation is related to cross-polarization effects. Therefore, in order to accurately describe the lines with arbitrarily oriented SRRs or CSRRs, it is necessary to include both electric and magnetic coupling in the models. Thus, the circuit model for SRR-loaded CPWs is shown in

[39] Notice that in the CSRR/gap-loaded microstrip line of Figure 3.37, the slits are aligned with the line axis. Strictly speaking, the model of Figure 3.38b is not valid for this CSRR orientation since mixed coupling is not considered in that model. However, the electric coupling is dominant, and the structure can be modeled by the circuit of Figure 3.38b to a first-order approximation.

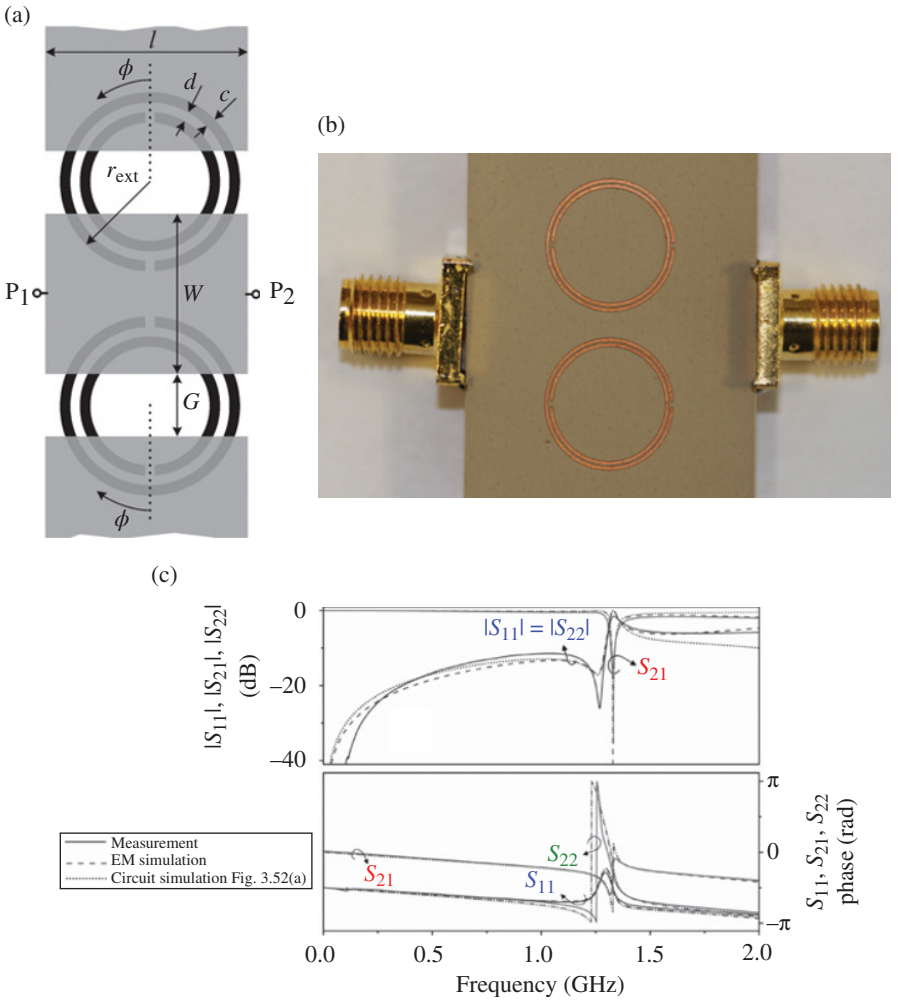

FIGURE 3.48 SRR-loaded CPW with arbitrary SRR orientation (a), fabricated SRR-loaded CPW structure with SRRs rotated $\phi = 90°$ (b), and frequency response (c). The substrate is the *Rogers RO3010* with dielectric constant $\varepsilon_r = 11.2$ and thickness $h = 1.27$ mm. Dimensions are: $W = 10.4$ mm, $G = 1.6$ mm, $l = 10.4$ mm, $r_{ext} = 5$ mm, and $c = d = 0.2$ mm. Reprinted with permission from Ref. [122]; copyright 2013 IEEE.

Figure 3.52a [122]. The circuit parameters are those in reference to Figure 3.34b, plus the coupling capacitance, C_a, that takes into account the electric coupling between the line and the SRRs (it is assumed that C_a depends on ϕ, being $C_a = 0$ if $\phi = 0°$). Notice that the asymmetry in the circuit model (necessary to explain that $S_{11} \neq S_{22}$) comes from the magnetic coupling (the dot convention for the mutual inductance is used, where the currents entering dot-marked terminals produce additive magnetic fluxes), although this is not manifested if electric coupling is not present.

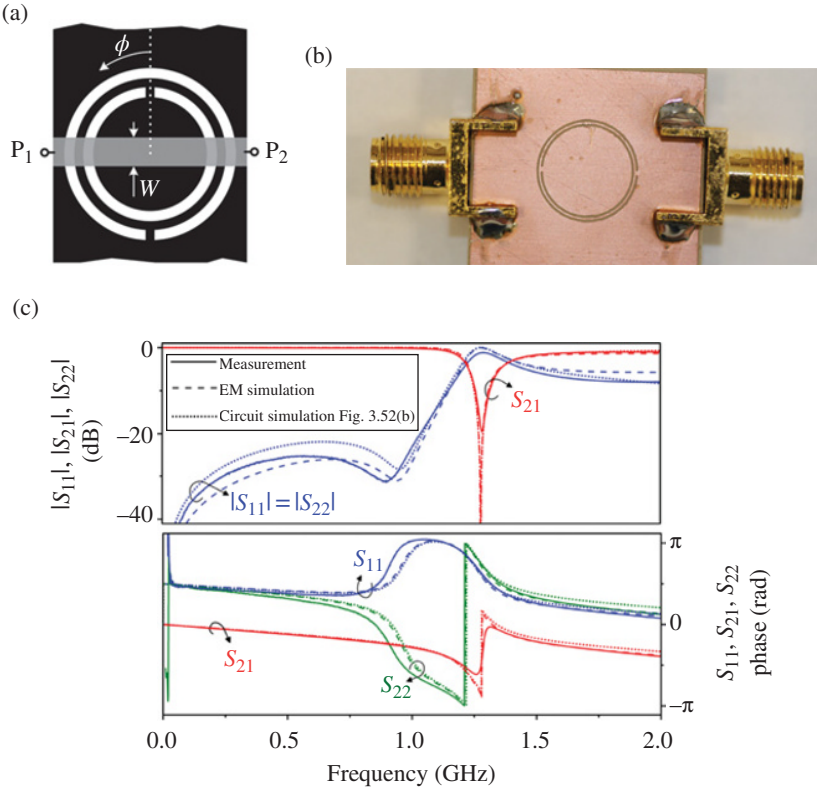

FIGURE 3.49 CSRR-loaded microstrip line with arbitrary CSRR orientation (a), fabricated CSRR-loaded microstrip line structure with the CSRR rotated $\phi = 90°$ (b), and frequency response (c). The substrate is the *Rogers RO3010* with dielectric constant $\varepsilon_r = 11.2$ and thickness $h = 1.27$ mm. Dimensions are: $W = 1.15$ mm, $l = 10.4$ mm, $r_{ext} = 5$ mm, and $c = d = 0.2$ mm. Reprinted with permission from Ref. [122]; copyright 2013 IEEE.

The parameters of the circuit model corresponding to the SRR-loaded line of Figure 3.48 were extracted. To this end, it was first considered the structure with SRRs oriented with $\phi = 0°$. By these means, the circuit parameters were inferred according to the procedure explained in Appendix G ($L' = 2.5$ nH, $C = 6$ pF, $L'_s = 0.4$ nH, $C'_s = 38.8$ pF, and $L = 1.45$ nH). Then, $L_s - C_s$, M, and C_a were adjusted by curve fitting the circuit simulation to the EM response, such that the resulting $L_s - C_s$ values were similar to the analytical SRR parameters given by Refs. [4, 69] ($L_s = 27.8$ nH and $C_s = 0.6$ pF). The resulting circuit parameters were found to be $L = 1.5$ nH, $C = 6.1$ pF, $L_s = 28.2$ nH, $C_s = 0.43$ pF, $M = 1.35$ nH, and $C_a = 0.08$ pF. The agreement between the circuit, EM simulation and measured response is good (see Fig. 3.48).

Figure 3.52b depicts the equivalent circuit model of CSRR-loaded microstrip lines that includes electric and magnetic coupling [122]. The circuit parameters are the same as in Figure 3.38a, plus the mutual inductance, M, that depends on ϕ ($M = 0$ if $\phi = 0°$),

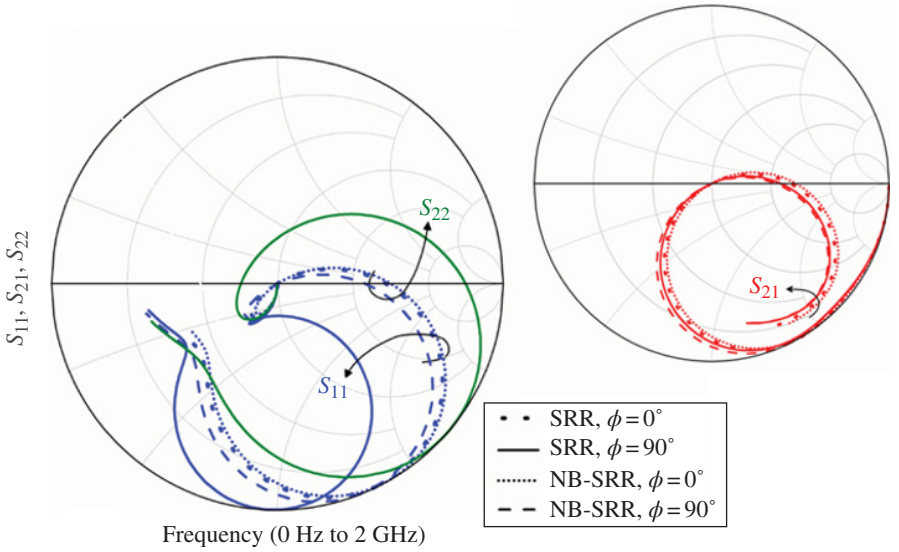

FIGURE 3.50 Frequency response in Smith chart of a CPW loaded with a pair of SRRs or NB-SRRs for two different rotation angles. The considered substrate and dimensions are those of Figure 3.48. Reprinted with permission from Ref. [122]; copyright 2013 IEEE.

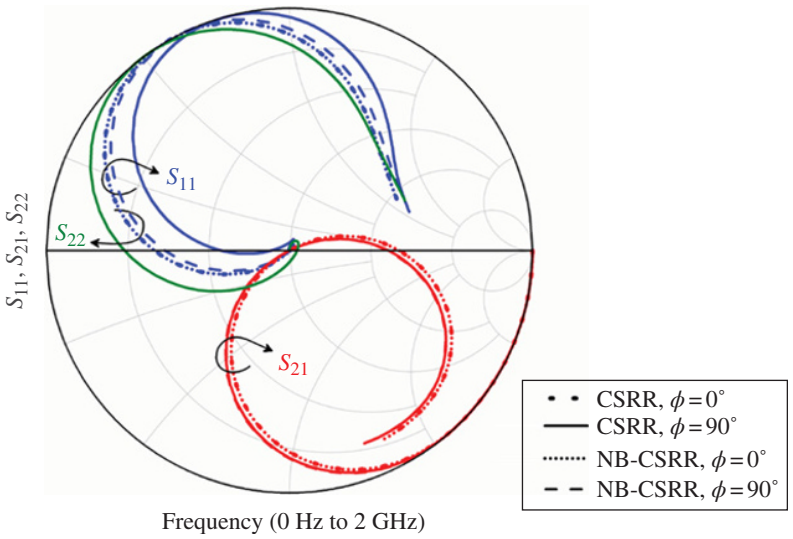

FIGURE 3.51 Frequency response in Smith chart of a microstrip line loaded with a CSRR or an NB-CSRR for two different rotation angles. The considered substrate and dimensions are those of Figure 3.49. Reprinted with permission from Ref. [122]; copyright 2013 IEEE.

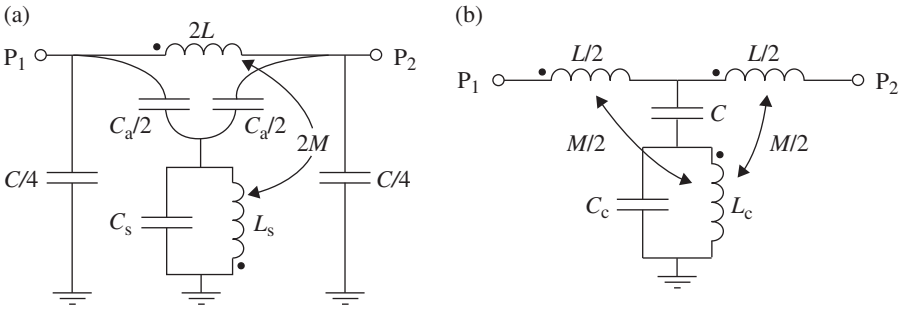

FIGURE 3.52 Equivalent circuit model (unit cell) of (a) a CPW loaded with arbitrarily oriented SRRs and (b) a microstrip line loaded with arbitrarily oriented CSRRs. The magnetic wall concept is applied in (a).

and accounts for the magnetic coupling between the line and the CSRR. The parameters of the circuit model corresponding to the CSRR-loaded line of Figure 3.49 were extracted. Similar to the SRR-loaded CPW, the parameters for $\phi = 0^\circ$ (all except M) were first extracted according to the method reported in Appendix G ($L = 7.87$ nH, $C = 1.62$ pF, $L_c = 2.94$ nH, and $C_c = 3.9$ pF). Finally, M was obtained by curve fitting, where a slight optimization of the other parameters was required. The resulting circuit elements were found to be $L = 7$ nH, $C = 1.7$ pF, $L_c = 2.74$ nH, $C_c = 3.95$ pF, and $M = 0.27$ nH. As Figure 3.49 reveals, the circuit simulation accurately describes the EM simulation and measured response.

Notice that the structures of Figures 3.48 and 3.49 are single negative structures; that is, they do not include shunt strips (for the SRR-loaded CPWs) or series gaps (for the CSRR-loaded microstrip line). The models for SRR/strip-loaded CPWs and CSRR/gap-loaded microstrip lines with arbitrarily oriented SRRs or CSRRs are out of the scope of this book since these models are too complicated for design purposes. Thus, in general, the SRR- or CSRR-based lines of interest for circuit design are those with the symmetry plane of the resonator orthogonal to the line axis, where mixed coupling can be neglected. Exceptions to this are microwave sensors based on the symmetry properties of SRR- or CSRR-loaded lines, or differential lines with common mode suppression, as will be shown later. Nevertheless, structures with the symmetry plane of the SRRs, or CSRRs, parallel to the line axis can be described to a first-order approximation by neglecting mixed coupling, since this simplifies the design process [123].

3.5.2.5 Transmission Lines based on OSRRs and OCSRRs According to the circuit models of the OSRR and OCSRR, reported in Section 3.3, it follows that by cascading series connected OSRRs and shunt connected OCSRRs alternating, CRLH lines described by the canonical circuit model of Figure 3.20 can potentially be implemented. The combination of OSRRs and OCSRRs has been demonstrated to be a powerful approach for the implementation of resonant type CRLH transmission lines [124, 125]. As will be seen, these artificial lines can be designed to exhibit very broad bands,

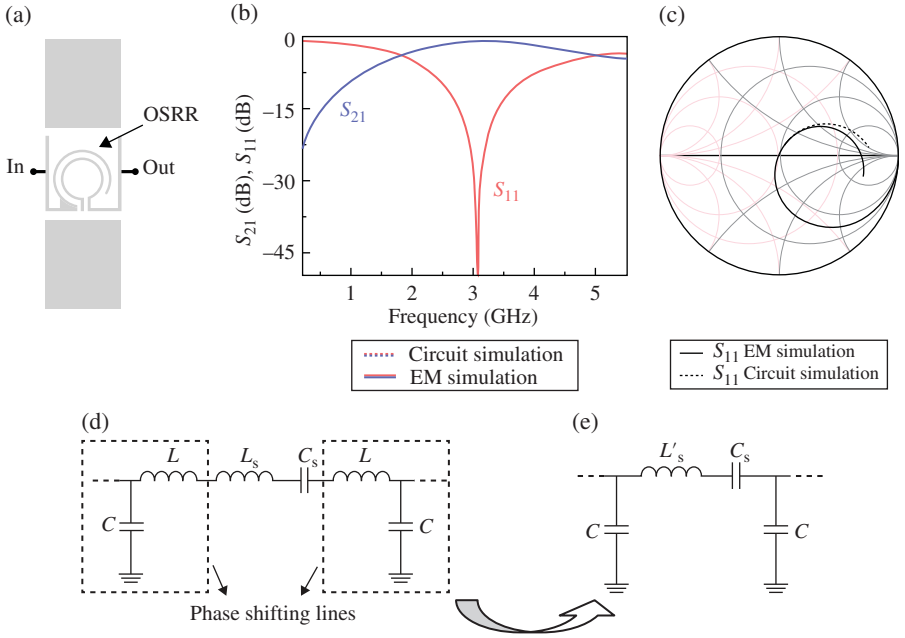

FIGURE 3.53 Topology (a), frequency response (magnitude) (b), representation of the reflection coefficient in the Smith Chart (c), and circuit model (d) and (e) of a typical OSRR-loaded CPW. This structure was implemented on the *Rogers RO3010* substrate with thickness $h = 0.254$ mm and measured dielectric constant $\varepsilon_r = 11.2$. Dimensions are $W = 5$ mm, $G = 0.55$ mm, $r_{ext} = 1.6$ mm, and $c = d = 0.2$ mm. The element values of the equivalent circuit inferred by parameter extraction are $C = 0.189$ pF, $L'_s = 5.55$ nH and $C_s = 0.58$ pF. This figure has been reproduced from Ref. [125] with permission from the author.

and the lumped-element equivalent circuit model is able to accurately describe the structures up to frequencies beyond the second (forward) transmission band.[40] The implementation of OSRR/OCSRR CRLH lines requires a host line, typically a CPW or a microstrip transmission line. The presence of the host line introduces parasitics in the circuit models of the particles. Therefore, the circuit model of CRLH lines based on the combination of OSRRs and OCSRR is not exactly the one of Figure 3.20. Let us now present these models for OSRRs and OCSRRs in CPW technology.

Figure 3.53 shows a typical topology of a series-connected OSRR in CPW technology, as well as the frequency response and the reflection coefficient, S_{11}, in the Smith chart. The fact that S_{11} does not lie in the unit resistance circle indicates that the model of the structure cannot merely be a series resonant tank. The presence of the host line introduces some phase shift that must be taken into account for an

[40] By contrast, the models of the SRR- or CSRR-based CRLH lines provide an accurate description of the lines in the first (LH) transmission band, but they tend to fail in the second (RH) transmission band, as Figure 3.42 illustrates.

accurate description of the OSRR-loaded CPW. Thus, in order to properly model the structure, additional elements to account for the phase shift must be introduced at both sides of the resonant tank describing the OSRR, that is, phase shifting lines. However, such phase shifting lines can be modeled through series inductances and shunt capacitances, as depicted in Figure 3.53. Notice that the model can be simplified as depicted in the figure, where C is a parasitic capacitance of the model. The circuit simulation of the model, also depicted in Figure 3.53, reveals that the agreement with the EM simulation is very good.

Figure 3.54 shows the topology of an arbitrary shunt connected-OCSRR pair in CPW technology. In order to prevent the slot mode, the different ground plane regions are connected through strips (etched in the ground plane) and vias. The strip that connects the ground planes at both sides of the central strip is optional and can be useful to enhance the shunt capacitance to ground, providing more degrees of freedom. The frequency response and S_{11} represented in the Smith chart are also included

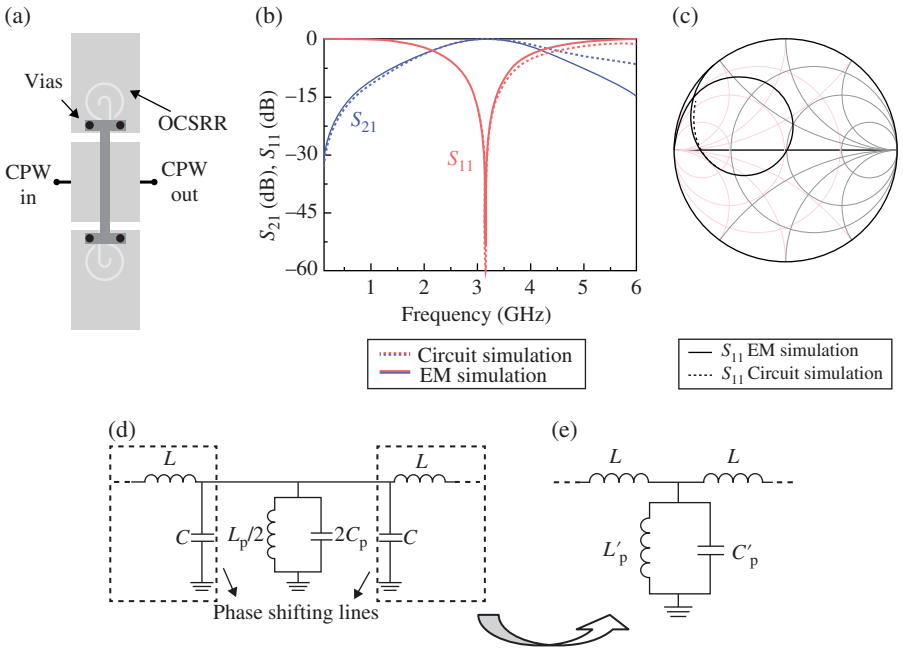

FIGURE 3.54 Topology (a), frequency response (magnitude) (b), representation of the reflection coefficient in the Smith Chart (c), and circuit model (d) and (e) corresponding to typical CPW transmission line loaded with a pair of shunt connected OCSRRs. Dimensions are $r_{ext} = 1.2$ mm, $c = 0.2$ mm, $d = 0.6$ mm, $W = 5$ mm, and $G = 0.55$ mm. The width of the strip connecting the different ground planes is 0.55 mm. The structure was implemented on the *Rogers RO3010* substrate with thickness $h = 0.254$ mm and measured dielectric constant $\varepsilon_r = 11.2$. The element values inferred by parameter extraction are $L = 0.32$ pF, $L'_p = 0.983$ nH and $C'_p = 2.85$ pF. This figure has been reproduced from Ref. [125] with permission from the author.

in Figure 3.54. The phenomenology is similar to that of the OSRR-loaded CPW. In this case, the trace of S_{11} deviates from the unit conductance circle, indicating that some phase shift is introduced by the host line, and preventing that the whole structure can be described by means of a shunt connected parallel resonant tank. The circuit model, and the simplified circuit model, are both depicted in Figure 3.54, where the parasitic element of the model is in this case the inductance L. The comparison between the circuit and EM simulation (Fig. 3.54) is also good, although some discrepancy in the insertion loss above 4 GHz can be appreciated. Interestingly, the broadband EM response of the structure of the OCSRR-loaded CPW of Figure 3.54 exhibits a transmission zero in the vicinity of 7.5 GHz. This transmission zero is caused by the inductance associated to the strip present between the central strip of the CPW and the inner metallic region of the OCSRRs. By taking into account this inductance (L_{sh}) in the model (see Fig. 3.55) [126], the agreement between the

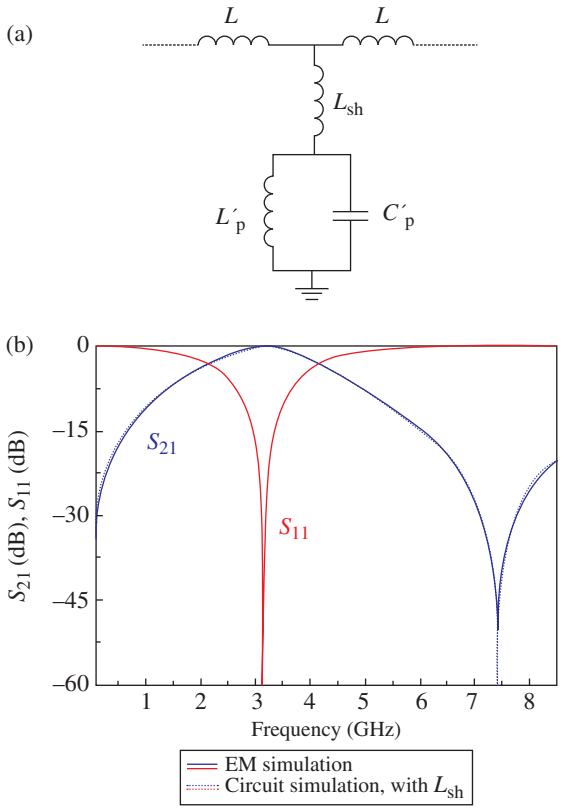

FIGURE 3.55 Wideband circuit model (a) and frequency response (magnitude) (b) of the pair of shunt connected OCSRRs shown in Figure 3.54a. The element values inferred by parameter extraction are $L = 0.345$ pF, $L'_p = 0.94$ nH, $C'_p = 2.98$ pF, and $L_{sh} = 0.185$ nH. Reprinted with permission from Ref. [126]; copyright 2011 IEEE.

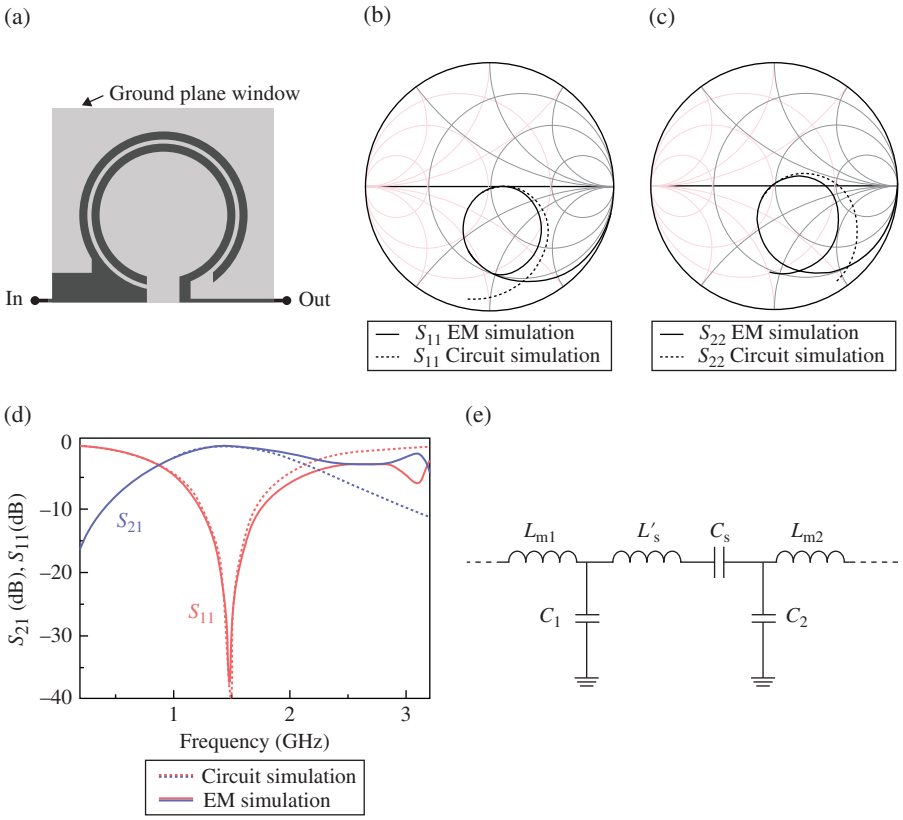

FIGURE 3.56 Topology (a), representation of S_{11} (b) and S_{22} (c) in the Smith chart, frequency response (magnitude) (d) and circuit model (e) of a typical series connected OSRR in microstrip technology with $r_{ext} = 4$ mm, $c = 0.4$ mm, and $d = 0.2$ mm. The considered substrate is the *Rogers RO3010* with thickness $h = 0.254$ mm and dielectric constant $\varepsilon_r = 10.2$. The element values are $L'_s = 12.93$ nH, $C_s = 1.33$ pF, $C_1 = 1.38$ pF, $C_2 = 0.98$ pF, $L_{m1} = 0.8$ nH, and $L_{m2} = 0$ nH. This figure has been reproduced from Ref. [125] with permission from the author.

frequency responses (circuit and EM simulation) is excellent, as Figure 3.55 reveals.[41] The model of Figure 3.55 is useful to accurately describe the frequency response of broadband filters (as will be seen in Chapter 4). However, in many applications the model of Figure 3.54 suffices.

In microstrip technology, series-connected OSRRs and shunt-connected OCSRRs exhibit different behavior. It has been found that OSRR-loaded microstrip lines (Fig. 3.56) cannot be properly described by the model of Figure 3.53. Indeed, the reflection coefficients, S_{11} and S_{22}, are quite different, as Figure 3.56 illustrates. This

[41] Depending on the distance between the two arms of the OSRR hooks, a capacitive effect may appear in the structure of Figure 3.53. This capacitance is the dual counterpart of the inductance L_{sh}, and to account for its effects in the model of Figure 3.53 it should be placed in parallel to the tank formed by L'_s and C_s.

suggests that the model must be asymmetric, and it has been found that the circuit model of Figure 3.56 provides a reasonable (although not very accurate) description of the OSRR-loaded microstrip line (look at the comparisons between the circuit and EM simulations depicted in Fig. 3.56).[42] However, the fact that the model is more complex does not mean that OSRR-loaded microstrip line sections cannot be used as part of CRLH lines or circuits based on them. Conversely, shunt-connected OCSRRs in microstrip technology (Fig. 3.57) behave as purely parallel LC resonators (the trace of S_{11} lies in the unit conductance circle), and the agreement between the circuit and EM simulation is excellent.

According to the models of OSRR- and OCSRR-loaded CPWs, the circuit models of the T-type or π-type CRLH lines based on OSRRs and OCSRRs are depicted in Figure 3.58 (the inductance L_{sh} has been omitted for simplicity). Notice that if the values of the parasitic elements L and C are close to zero, the models can be approximated by the canonical T- or π-type circuit models of a CRLH line (see Fig. 3.20). Indeed, the parasitic effects can be minimized by choosing appropriate geometries for the resonators. Thus, if the terminals of the OCSRR section are shortened in the topology of Figure 3.58b, L vanishes, and the structure can be described by the canonical π-type circuit model of the CRLH line since the parasitic capacitance C of the OSRR is added to the shunt capacitance of the OCSRR [125]. Similarly, for the structure of Figure 3.58a, if the slots of the CPW line are expanded, C is very small, and the parasitic inductance L of the OCSRR is absorbed by the inductance of the OSRR, resulting in the canonical T-type circuit model of the CRLH transmission line. The structure of Figure 3.58b is a quasibalanced CRLH line, where the effects of the parasitic elements are very small. The dispersion diagram and the frequency response of this structure are depicted in Figure 3.59. Notice that the series and shunt resonance frequencies (look at the element values in the caption of Fig. 3.59) of the structure of Figure 3.58b are not identical. The reason is that in order to balance the structures described by the models of Figure 3.58 (with the presence of parasitics) the condition of equal resonance frequencies for the series and shunt branch no longer holds. To balance the structures described by the models of Figure 3.58, it is necessary to force the series reactance and shunt susceptance of the equivalent T or π circuit model to zero at the desired transition frequency. For the circuit of Figure 3.58c, corresponding to the structure of 3.58a, the series and shunt impedances of the equivalent T-circuit model are given by [125]:

$$Z_s(\omega) = -j\frac{\left[\left(1-\omega^2 L'_s C_s\right) + L\omega^2\left(CL'_s C_s\omega^2 - C - C_s\right)\right]}{\omega\left[C_s + C\omega^2\left(CL\left(\omega^2 L'_s C_s - 1\right) - 2C_s L - L'_s C_s + \frac{1}{\omega^2}\right)\right]} \tag{3.99a}$$

$$Z_p(\omega) = -j\frac{\omega L'_p C_s^2}{\left(1-\omega^2 L'_p C'_p\right)C_1^2 + CC_2\omega^2(CC_2 LL_2\omega^2 - 2C_1 L_1)} \tag{3.99b}$$

[42] Since the number of reactive elements of the OSRR-loaded microstrip line model is too high, such elements have been determined by curve fitting, rather than by parameter extraction.

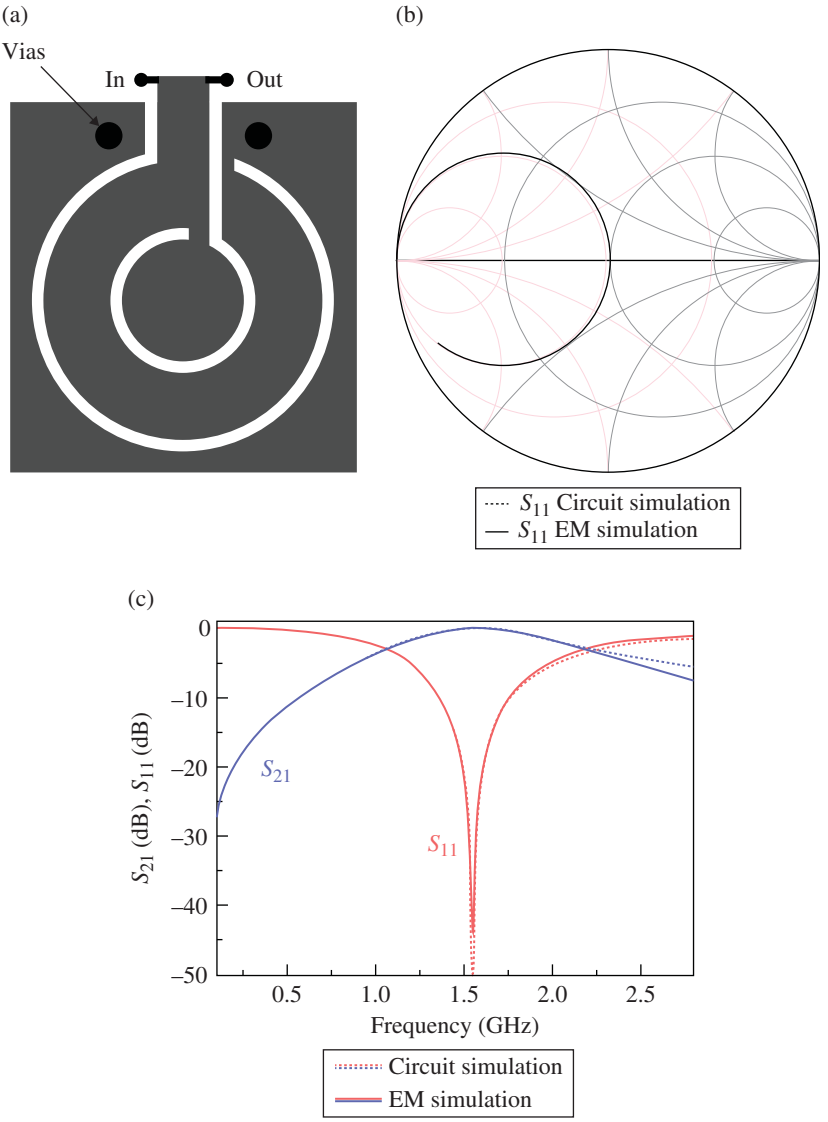

FIGURE 3.57 Topology (a), representation of S_{11} in the Smith Chart (b) and frequency response (magnitude) (c) of a typical shunt-connected OCSRR in microstrip technology with $r_{ext} = 2.7$ mm, $c = 0.2$ mm, and $d = 1.2$ mm. The considered substrate is the *Rogers RO3010* with thickness $h = 0.254$ mm and dielectric constant $\varepsilon_r = 10.2$. The element values of the shunt resonator in reference of Figure 3.17b are $L_o = 2.02$ nH and $C_c = 5.25$ pF. This figure has been reproduced from Ref. [125] with permission from the author.

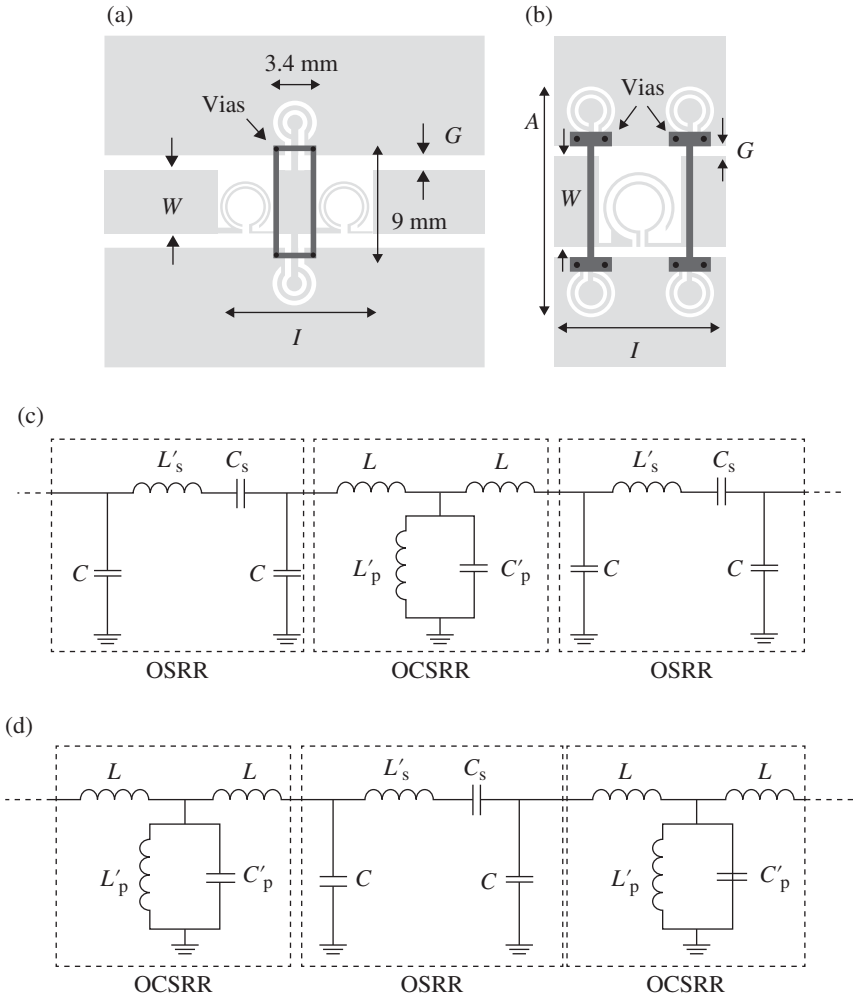

FIGURE 3.58 Typical CPW topologies to implement the *T*- (a) or π- (b) circuit model (unit cell) of a CRLH transmission line based on a combination of OSRRs and OCSRRs. The corresponding circuit models of the structures of (a) and (b) are depicted in (c) and (d), respectively. This figure has been reproduced from Ref. [125] with permission from the author.

with

$$C_1 = C_s + C\left(1 - \frac{\omega^2}{\omega_s^2}\right) \tag{3.100a}$$

$$C_2 = 2C_s + C\left(1 - \frac{\omega^2}{\omega_s^2}\right) \tag{3.100b}$$

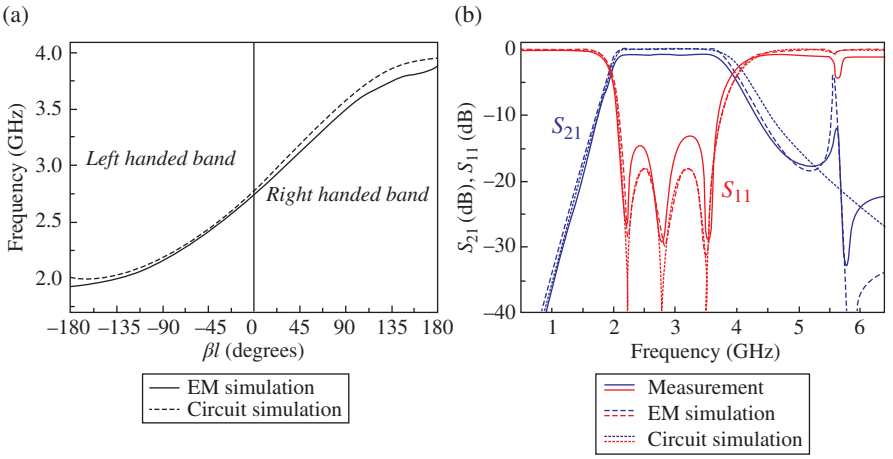

FIGURE 3.59 Dispersion diagram (a) and frequency response (b) of the CPW quasibalanced CRLH line based on open resonators shown in Figure 3.58b. The considered substrate is the *Rogers RO3010* with thickness $h = 0.254$ mm and measured dielectric constant $\varepsilon_r = 11.2$. Dimensions (in reference to Fig. 3.58b) are $l = 7.4$ mm, $A = 11.5$ mm, $W = 4.5$ mm, and $G = 0.52$ mm; for the OCSRRs, $r_{ext} = 1.2$ mm, $c = 0.2$ mm, and $d = 0.2$ mm. For the OSRRs, $r_{ext} = 1.8$ mm, $c = 0.2$ mm, and $d = 0.3$ mm. The values of the equivalent circuit in reference to Figure 3.58d are $C = 0.19$ pF, $L = 0.05$ nH, $C_s = 0.515$ pF, $L'_s = 6.16$ nH, $C'_p = 1.91$ pF, and $L'_p = 1.55$ nH. This figure has been reproduced from Ref. [125] with permission from the author.

$$L_1 = L'_p + L\left(1 - \frac{\omega^2}{\omega_p^2}\right) \tag{3.100c}$$

$$L_2 = 2L'_p + L\left(1 - \frac{\omega^2}{\omega_p^2}\right) \tag{3.100d}$$

$$\omega_s = \frac{1}{\sqrt{L'_s C_s}} \tag{3.100e}$$

$$\omega_p = \frac{1}{\sqrt{L'_p C'_p}} \tag{3.100f}$$

Thus, (3.99) can be used for design purposes, including the synthesis of balanced lines. As will be seen in Chapter 4, CRLH lines based on OSRRs and OCSRRs are useful for the design of dual-band components and broadband bandpass filters.

3.5.2.6 Synthesis Techniques This section has been focused on the resonant type approach of metamaterial transmission lines, where the main topologies and circuit

models have been presented and discussed. The author and his research group have dedicated a significant effort in recent years to the automated synthesis of these artificial lines on the basis of the so-called aggressive space mapping (ASM) optimization. This synthesis technique, based on quasi-Newton type iteration, is applied to automatically find the layout of the structure (unit cell) from the elements of the equivalent circuit model (which are assumed to be determined from circuit specifications). ASM optimization is important for the design of microwave circuits based on these artificial lines. However, the general formulation of ASM, as well as its application to the implementation of practical synthesis tools is very specific and requires significant effort for understanding. Therefore, this part is left for Appendix H (recommended to those readers willing to design microwave circuits based on resonant type metamaterial transmission lines).

3.5.3 The Hybrid Approach

In 2006, metamaterial transmission lines based on a combination of CSRRs, series gaps, and shunt-connected stubs were presented for the first time [127]. These artificial lines were called hybrid lines [128] because they are implemented by using the reactive elements of the CL-loaded approach (series gaps and shunt connected stubs) and the resonant type approach (CSRRs). Since they include more reactive elements than CL-loaded lines and resonant type metalines, hybrid lines exhibit a richer phenomenology. Indeed, these lines were proposed for the implementation of narrow (and moderate) band bandpass filters exhibiting backward wave propagation in the transmission band and a transmission zero above it (with the intention of improving the stop band response of the filters) [127]. The typical topology and circuit model of the unit cell of a hybrid line are depicted in Figure 3.60. The interpretation of the

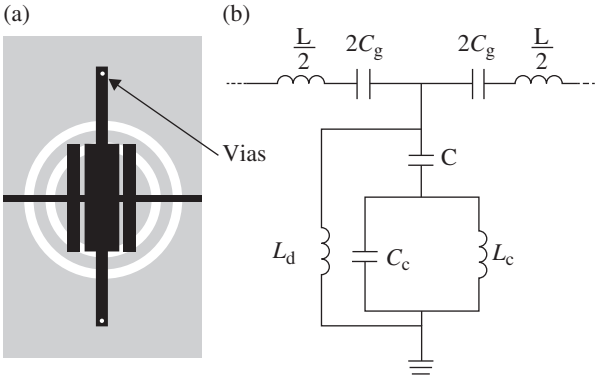

FIGURE 3.60 Typical topology of the unit cell of a metaline based on the hybrid approach (a) and lumped-element equivalent circuit model (b). In (a), the upper metal layer is depicted in black, whereas the lower metal layer (ground plane), where the CSRR is etched, is depicted in gray.

different model parameters is similar to that given for CSRR-based lines, except that now we have an additional element, the shunt inductance, L_d, that accounts for the pair of grounded (through vias) stubs.

Due to the presence of shunt stubs, hybrid lines exhibit three transmission bands, rather than two, plus one transmission zero, which is given by (3.86). As discussed before, wave propagation is possible in those frequency regions where the phase constant is a real number. The dispersion characteristics can easily be inferred from the circuit model numerically, or by means of a circuit simulator. Depending on the relative positions of the relevant frequencies of the structure, two types of dispersion result, where the differences refer to the nature, LH or RH, of the different transmission bands [9]. The two possibilities are (1) LH–LH–RH and (2) LH–RH–RH. Hence, the difference is that the central (second) band can be either LH or RH (the first and third band always exhibit LH and RH wave propagation, respectively). If $f_{ser} < f_z$ (with $f_{ser} = (LC_g)^{-1/2}/2\pi$), then the transmission bands are LH–RH–RH; if $f_{ser} > f_z$, wave transmission in the bands follows the sequence LH–LH–RH. Of particular interest is the balanced case, where two of the bands merge. Let us denote the two poles of the shunt branch of the circuit model as f_{p1} and f_{p2}, with $f_{p1} < f_{p2}$. If (i) $f_{p1} = f_{ser}$, the first (LH) and the second (RH) bands merge, and the third (RH) band is isolated; if (ii) $f_{p2} = f_{ser}$, the second (LH) and the third (RH) band merge, and the first (LH) band is isolated. The former situation is interesting for wide band filter design because it is possible to achieve broad bands with a transmission zero above these bands [129].

The dispersion and characteristic impedance corresponding to the particular hybrid structure shown in Figure 3.61a are depicted in Figure 3.61b and c. This structure is un-balanced with $f_{ser} > f_z$, thus, the sequence of the bands is LH–LH–RH. The agreement between experimental data, EM simulation and circuit simulation is good. The parameters of the circuit model were extracted following a parameter extraction method similar to that reported in Appendix G.

Although hybrid lines exhibit three transmission bands, these lines cannot be considered to be order-3 CRLH transmission lines. The reason is that the number of elements in the series branch of the T-circuit model is limited to two (L and C_g). Therefore, it is not possible to obtain certain functionalities achievable with order-3 CRLH transmission lines. For instance, it is not possible to implement tri-band components by means of hybrid lines of the type shown in Figures 3.60 or 3.61. As will be later shown (Chapter 4), to implement tri-band components it is necessary to force the characteristic impedance and phase shift of the constituent artificial lines of such tri-band circuits to the required values at three operating frequencies, and this is only possible if at least three elements for both the series and shunt branches are present. Hence hybrid lines are essentially useful to achieve certain functionality in two bands (or in a single band). However, the presence of the shunt inductive stub enhances design flexibility. This is the main advantage of hybrid lines over SRR- or CSRR-loaded lines. This design flexibility has been exploited in the design of bandpass filters, where superior performance (i.e., improved bandwidth and stopband) with respect to filters based on SRR- or CSRR-loaded lines has been achieved [127–129] (however this aspect will be discussed in Chapter 4).

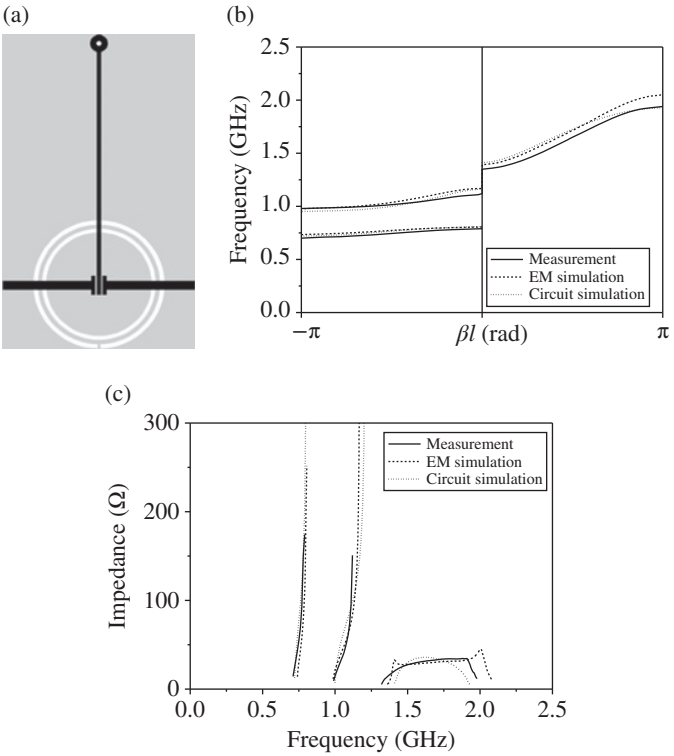

FIGURE 3.61 Topology (a), dispersion diagram (b) and characteristic impedance (c) for a hybrid microstrip structure, inferred from EM simulation (dashed line), from measurement (solid line) and from circuit simulation (dotted line). The considered substrate is the *Rogers RO3010* with thickness $h = 0.635$ mm and dielectric constant $\varepsilon_r = 10.2$. Dimensions are: host line width $W = 1$ mm, line length $l = 21.97$ mm, gaps separation $s_g = 0.2$ mm, gap width $W_g = 2.17$ mm, stub length $l_s = 26.23$ mm, and stub width $W_s = 0.44$ mm; for the CSRR, external radius $r_{ext} = 7.48$ mm, ring width $c = 0.43$ mm, and ring separation $d = 0.54$ mm. The extracted element values, used for the circuit simulation, are $L = 18.65$ nH, $C_g = 0.68$ pF, $C = 5.35$ pF, $C_c = 42.82$ pF, $L_c = 0.67$ nH, and $L_d = 4.77$ nH. Reprinted with permission from Ref. [9]; copyright 2011 IEEE.

REFERENCES

1. D. Schurig, J. J. Mock, B. J. Justice, S. A. Cummer, J. B. Pendry, A. F. Starr, and D. R. Smith, "Metamaterial electromagnetic cloak at microwave frequencies," *Science*, vol. **314**, pp. 977–980, 2006.
2. G. V. Eleftheriades and K. G. Balmain, Ed., *Negative-Refraction Metamaterials: Fundamental Principles and Applications*, Wiley-Interscience, Hoboken, NJ, 2005.
3. C. Caloz and T. Itoh, *Electromagnetic Metamaterials: Transmission Line Theory and Microwave Applications*, John Wiley & Sons, Hoboken, NJ, 2006.
4. R. Marqués, F. Martín, and M. Sorolla, *Metamaterials with Negative Parameters: Theory, Design and Microwave Applications*, Wiley-Interscience, Hoboken, NJ, 2007.

5. A. K. Iyer and G. V. Eleftheriades, "Negative refractive index metamaterials supporting 2-D waves," *IEEE-MTT Int. Microw. Symp. Dig.*, Seattle, WA, June 2002, pp. 412–415.
6. A. A. Oliner, "A periodic-structure negative-refractive-index medium without resonant elements," *URSI Dig. IEEE-AP-S USNC/URSI Natl. Radio Sci. Meet.*, San Antonio, TX, June 2002, p. 41.
7. C. Caloz and T. Itoh, "Application of the transmission line theory of left-handed (LH) materials to the realization of a microstrip LH transmission line," *Proc. IEEE-AP-S USNC/URSI National Radio Science Meeting*, vol. 2, San Antonio, TX, June 2002, pp. 412–415.
8. F. Martín, F. Falcone, J. Bonache, R. Marqués, and M. Sorolla, "Split ring resonator based left handed coplanar waveguide," *Appl. Phys. Lett.*, vol. **83**, pp. 4652–4654, 2003.
9. M. Durán-Sindreu, A. Vélez, G. Sisó, J. Selga, P. Vélez, J. Bonache, and F. Martín, "Recent advances in metamaterial transmission lines based on split rings," *Proc. IEEE*, vol. **99**, pp. 1701–1710, 2011.
10. J. D. Baena, J. Bonache, F. Martín, R. Marqués, F. Falcone, T. Lopetegi, M. A. G. Laso, J. García, I. Gil, M. Flores-Portillo, and M. Sorolla, "Equivalent circuit models for split ring resonators and complementary split rings resonators coupled to planar transmission lines," *IEEE Trans. Microw. Theory Tech.*, vol. **53**, pp. 1451–1461, 2005.
11. C. Caloz and T. Itoh, "Novel microwave devices and structures based on the transmission line approach of metamaterials," *IEEE-MTT Int. Microw. Symp. Dig.*, vol. **1**, Philadelphia, PA, June 2003, pp. 195–198.
12. D. R. Smith, W. J. Padilla, D. C. Vier, S. C. Nemat-Nasser, and S. Schultz, "Composite medium with simultaneously negative permeability and permittivity," *Phys. Rev. Lett.*, vol. **84**, pp. 4184–4187, 2000.
13. R. A. Shelby, D. R. Smith, and S. Schultz, "Experimental verification of a negative index of refraction," *Science*, vol. **292**, pp. 77–79, 2001.
14. R. A. Shelby, D. R. Smith, S. C. Nemat-Nasser, and S. Schultz, "Microwave transmission through a two-dimensional, isotropic, left-handed metamaterial," *Appl. Phys. Lett.*, vol. **78**, pp. 489–491, 2001.
15. A. Grbic and G. V. Eleftheriades, "Experimental verification of backward wave radiation from a negative refractive index metamaterial," *J. Appl. Phys.*, vol. **92**, pp. 5930–5935, 2002.
16. V. G. Veselago, "The electrodynamics of substances with simultaneously negative values of ε and μ," *Sov. Phys. Usp.*, vol. **10**, pp. 509–514, 1968.
17. N. Engheta and R. W. Ziolkowski, *Metamaterials: Physics and Engineering Explorations*, Wiley-Interscience, Hoboken, NJ, 2006.
18. A. K. Sarychev and V. M. Shalaev, *Electrodynamics of Metamaterials*, World Scientific Publishing Co., Singapore, 2007.
19. P. Markos and C. M. Sokoulis, *Wave Propagation: From Electrons to Photonic Crystals and Left-Handed Materials*, Princeton University Press, Princeton, NJ, 2008.
20. F. Capolino, Ed., *Metamaterials Handbook*, CRC Press, Boca Raton, FL 2009.
21. L. Solymar and E. Shamonina, *Waves in Metamaterials*, Oxford University Press, Oxford, 2009.
22. T. J. Cui, D. R. Smith, and R. Liu, Eds., *Metamaterials: Theory, Design and Applications*, Springer, New York, 2010.

23. R. W. Ziolkowski and E. Heynman, "Wave propagation in media having negative permeability and permittivity," *Phys. Rev. E*, vol. **64**, paper 056625, 2001.

24. V. G. Veselago, "Formulating Fermat's principle for light travelling in negative refraction materials," *Phys. Usp.*, vol. **45**, pp. 1097–1099, 2002.

25. I. V. Lindell, S. A. Tretyakov, K. I. Nikoskinen, and S. Ilvonen, "BW-media with negative parameters, capable of supporting backward waves," *Microw. Opt. Technol. Lett.*, vol. **31**, pp. 129–133, 2001.

26. A. Sihvola, "Electromagnetic emergence in metamaterials," in *Advances in Electromagnetics of Complex Media and Metamaterials*, S. Zouhdi, A. Sihvola, and M. Arsalane, Eds., NATO Science Series: II: Mathematics, Physics, and Chemistry, vol. **89**, pp. 1–17, Kluwer Academic Publishers, Dordrecht, 2003.

27. W. Rotman, "Plasma simulation by artificial dielectrics and parallel-plate media," *IRE Trans. Antennas Propag.*, vol.**10**, pp. 82–95, 1962.

28. J. B. Pendry, A. J. Holden, W. J. Stewart, and I. Youngs, "Extremely low frequency plasmons in metallic mesostructures," *Phys. Rev. Lett.*, vol. **76**, pp. 4773–4776, 1996.

29. J. B. Pendry, A. J. Holden, D. J. Robbins, and W. J. Stewart, "Low frequency plasmons in thin-wire structures," *J. Phys. Condens. Matter.*, vol. **10**, pp. 4785–4810, 1998.

30. J. B. Pendry, A. J. Holden, D. J. Robbins, and W. J. Stewart, "Magnetism from conductors and enhanced nonlinear phenomena," *IEEE Trans. Microw. Theory Tech.*, vol. **47**, pp. 2075–2084, 1999.

31. S. Ramo, J. R. Whinnery, and T. Van-Duzer, *Fields and Waves in Communication Electronics*, Wiley, Hoboken, NJ, 1965, and 2nd (1984) and 3rd (1994) Editions.

32. M. Mrozowski, *Guided Electromagnetic Waves. Properties and Analysis*, Research Studies Press, Taunton and Wiley, New York, 1997.

33. J. A. Kong, *Electromagnetic Wave Theory*, EMW Publishing, Cambridge, MA, 2000.

34. R. F. Harrington, *Time-harmonic Electromagnetic Fields*, McGraw-Hill, New York, 1961.

35. L. D. Landau, E. M. Lifshitz, and L. P. Pitaevskii, *Electrodynamics of Continuous Media*, Pergamon, New York, 1984.

36. J. D. Jackson, *Classical Electrodynamics*, 3rd Edition, Wiley, New York, 1999.

37. D. R. Smith, D. Schurig, and J. B. Pendry, "Negative refraction of modulated electromagnetic waves," *Appl. Phys. Lett.*, vol. **81**, pp. 2713–2715, 2002.

38. S. Foteinopoulou, E. N. Economou, and C. M. Soukoulis, "Refraction in media with a negative refractive index," *Phys. Rev. Lett.*, vol. **90**, paper 107402, 2003.

39. C. G. Parazzoli, R. B. McGregor, K. Li, B. E. C. Kontenbah, and M. Tlienian, "Experimental verification and simulation of negative index of refraction using Snell's law," *Phys. Rev. Lett.*, vol. **90**, paper 107401, 2003.

40. K. Li, S. J. McLean, R. B. Gregor, C. G. Parazzoli, and M. H. Tanielian, "Free-space focused-beam characterization of left-handed materials," *Appl. Phys. Lett.*, vol. **82**, pp. 2535–2537, 2003.

41. A. A. Houck, J. B. Brock, and I. L. Chuang, "Experimental observations of a left-handed material that obeys Snell's law," *Phys. Rev. Lett.*, vol. **90**, paper 137401, 2003.

42. D. Felbacq and A. Moreau, "Direct evidence of negative refraction at media with negative ε and μ," *J. Opt. A Pure Appl. Opt.*, vol. **5**, pp. L9–L11, 2003.

43. J. B. Pendry, "Negative refraction makes perfect lens," *Phys. Rev. Lett.*, vol. **85**, pp. 3966–3969, 2000.

44. A. Grbic, R. Merlin, E. M. Thomas, and M. F. Imani, "Near-field plates: metamaterial surfaces/arrays for subwavelength focusing and probing," *Proc. IEEE*, vol. **99**, pp. 1806–1815, 2011.

45. J. Lu, T. M. Gregorczyc, Y. Zhang, J. Pacheco, B. Wu, J. A. Kong, and M. Chen, "Cerenkov radiation in materials with negative permittivity and permeability," *Opt. Express*, vol. **11**, pp. 723–734, 2003.

46. P. R. Berman, "Goos-Hächen shift in negatively refractive media," *Phys. Rev. E*, vol. **66**, paper 067603, 2002.

47. J. A. Kong, B. I. Wu, and Y. Zhang, "Lateral displacement of a Gaussian beam reflected from a grounded slab with negative permittivity and permeability," *Appl. Phys. Lett.*, vol. **80**, pp. 2084–2086, 2002.

48. R. W. Ziolkowski, "Pulsed and CW Gaussian beam interactions with double negative metamaterial slabs," *Opt. Express*, vol. **11**, pp. 662–681, 2003.

49. A. Lakhtakia, "On plane wave remittances and Goos-Hänchen shifts of planar slabs with negative real permittivity and permeability," *Electromagnetics*, vol. **23**, pp. 71–75, 2002.

50. I. V. Shadrivov, A. A. Zharov, and Y. S. Kivshar, "Giant Goos-Hänchen effect at the refraction from left-handed metamaterials," *Appl. Phys. Lett.*, vol. **83**, pp. 2713–2715, 2003.

51. C. Luo, S. G. Johnson, J. D. Joannopoulos, and J. B. Pendry, "All-angle negative refraction without negative effective index," *Phys. Rev. B*, vol. **65**, paper 201104(R), 2002.

52. M. Notomi, "Theory of light propagation in strongly modulated photonic crystals: refraction like behavior in the vicinity of the photonic band gap," *Phys. Rev. B*, vol. **62**, pp. 10696–10705, 2000.

53. E. Cubukcu, K. Aydin, E. Ozbay, S. Foteinopoulou, and C. M. Soukoulis, "Electromagnetic waves: negative refraction by photonic crystals," *Nature*, vol. **423**, pp. 604–605, 2003.

54. N. B. Kundtz, D. R. Smith, and J. B. Pendry, "Electromagnetic design with transformation optics," *Proc. IEEE*, vol. **99**, pp. 1122–1633, 2011.

55. R. Marques, L. Jelinek, M. J. Freire, J. D. Baena, and M. Lapine, "Bulk metamaterials made of resonant rings," *Proc. IEEE*, vol. **99**, pp. 1660–1668, 2009.

56. D. O. Guney, T. Koschny, and C. M. Soukoulis, "Intra-connected three-dimensionally isotropic bulk negative index photonic metamaterial," *Opt. Express*, vol. **18**, pp. 12348–12353, 2010.

57. A. Grbic and G. V. Eleftheriades, "Overcoming the diffraction limit with a planar left-handed transmission-line lens," *Phys. Rev. Lett.*, vol. **92**, paper 117403, 2004.

58. A. Sanada, C. Caloz, and T. Itoh, "Planar distributed structures with negative refractive index," *IEEE Trans. Microw. Theory Tech.*, vol. **52**, pp. 1252–1263, 2004.

59. F. Elek and G. V. Eleftheriades, "A two-dimensional uniplanar transmission-line metamaterial with a negative index of refraction," *New J. Phys.*, vol. **7**, p. 163, 2005.

60. A. Grbic and G. V. Eleftheriades, "A 3-D negative-refractive-index transmission-line medium," *IEEE AP-S/URSI Int. Symp.*, Washington, DC, July 2005.

61. A. Grbic and G. V. Eleftheriades, "An isotropic three-dimensional negative-refractive-index transmission-line metamaterial," *J. Appl. Phys.*, vol. **98**, paper 043106, 2005.

62. P. Alitalo, S. Maslovski, and S. Tretyakov, "Three-dimensional isotropic perfect lens based on LC-loaded transmission lines," *J. Appl. Phys.*, vol. **99**, paper 064912, 2006.

63. P. Alitalo, S. Maslovski, and S. Tretyakov, "Experimental verification of the key properties of a three-dimensional isotropic transmission-line superlens," *J. Appl. Phys.*, vol. **99**, paper 124910, 2006.

64. M. Zedler, C. Caloz, and P. Russer, "A 3-D isotropic left-handed metamaterial based on the rotated transmission-line matrix (TLM) scheme," *IEEE Trans. Microw. Theory Tech.*, vol **55**, pp. 2930–2941, 2007.

65. A. K. Iyer and G. V. Eleftheriades, "A three-dimensional isotropic transmission-line metamaterial topology for free-space excitation," *Appl. Phys. Lett.*, vol. **92**, paper 261106, 2008.

66. C. Garcia-Meca, J. Hurtado, J. Martí, A. Martínez, W. Dickson, and A. V. Zayats, "Low-loss multilayered metamaterial exhibiting a negative index of refraction at visible wavelengths," *Phys. Rev. Lett.*, vol. **106**, paper 067402, 2011.

67. C. M. Soukoulis and M. Wegener, "Past achievements and future challenges in the development of three-dimensional photonic metamaterials," *Nat. Photonics*, vol. **5**, pp. 523–530, 2011.

68. S. A. Shelkunoff and H. T. Friis, *Antennas: Theory and Practice*, 3rd Edition, Wiley, New York, 1966.

69. R. Marques, F. Medina, and R. Rafii-El-Idrissi, "Role of bi-anisotropy in negative permeability and left handed metamaterials," *Phys. Rev. B*, vol. **65**, paper 144441, 2002.

70. I. Bahl and P. Bhartia, *Microwave Solid State Circuit Design*, Wiley, New York, 1988.

71. A. L. Pokrovsky and A. L. Efros, "Electrodynamics of photonic crystals and the problem of left-handed metarials," *Phys. Rev. Lett.*, vol. **89**, paper 093901, 2002.

72. R. Marques and D. R. Smith, "Comments to Electrodynamics of photonic crystals and the problem of left-handed metamaterials," *Phys. Rev. Lett.*, vol. **92**, paper 059401, 2004.

73. R. Marqués, J. Martel, F. Mesa, and F. Medina, "Left-handed-media simulation and transmission of EM waves in subwavelength split-ring-resonator-loaded metallic waveguides," *Phys. Rev. Lett.*, vol. **89**, paper 183901, 2002.

74. J. Esteban, C. Camacho-Peñalosa, J. E. Page, T. M. Martin-Guerrero, and E. Marquez-Segura, "Simulation of negative permittivity and negative permeability by means of evanescent waveguide modes—theory and experiment," *IEEE Trans. Microw. Theory Tech.*, vol. **53**, pp. 1506–1514, 2005.

75. R. Marqués, J. D. Baena, J. Martel, F. Medina, F. Falcone, M. Sorolla, and F. Martin, "Novel small resonant electromagnetic particles for metamaterial and filter design," *Proc. ICEAA'03*, Torino, Italy, September 8–12, 2003, pp. 439–442.

76. J. D. Baena. R. Marqués, F. Medina, and J. Martel, "Artificial magnetic metamaterial design by using spiral resonators," *Phys. Rev. B*, vol. **69**, paper 014402, 2004.

77. M. Makimoto, S. Yamashita, "Compact bandpass filters using stepped impedance resonators," *Proc. IEEE*, vol. **67**, pp. 16–19, 1979.

78. D. Schurig, J. J. Mock, and D. R. Smith, "Electric-field-coupled resonators for negative permittivity metamaterials," *Appl. Phys. Lett.*, vol. **88**, paper 041109, 2006.

79. J. García-García, F. Martín, J. D. Baena, R. Marqués, and L. Jelinek, "On the resonances and polarizabilities of split ring resonators," *J. Appl. Phys.*, vol. **98**, paper 033103, 2005.

80. J. Martel, R. Marqués, F. Falcone, J. D. Baena, F. Medina, F. Martín and M. Sorolla, "A new LC series element for compact band pass filter design," *IEEE Microw. Wireless Compon. Lett.*, vol. **14**, pp. 210–212, 2004.

81. H. G. Booker, "Slot aerials and their relation to complementary wire aerials (Babinet's principle)," *J. IEE*, vol. **93**, pt. III–A, no. 4, pp. 620–626, 1946.

82. G. A. Deschamps, "Impedance properties of complementary multiterminal planar structures," *IRE Trans. Antennas Propag.*, vol. **AP–7**, pp. 371–378, 1959.

83. W. J. Getsinger, "Circuit duals on planar transmission media," *IEEE MTT-S Int. Microw. Symp. Dig.*, Boston, MA, May–June 1983, pp. 154–156.

84. F. Falcone, T. Lopetegi, J. D. Baena, R. Marqués, F. Martín, and M. Sorolla, "Effective negative-ε stop-band microstrip lines based on complementary split ring resonators," *IEEE Microw. Wireless Compon. Lett.*, vol. **14**, pp. 280–282, 2004.

85. F. Falcone, T. Lopetegi, M. A. G. Laso, J. D. Baena, J. Bonache, R. Marqués, F. Martín, and M. Sorolla, "Babinet principle applied to the design of metasurfaces and metamaterials," *Phys. Rev. Lett.*, vol. **93**, paper 197401, 2004.

86. A. Velez, F. Aznar, J. Bonache, M. C. Velázquez-Ahumada, J. Martel, and F. Martín, "Open complementary split ring resonators (OCSRRs) and their application to wideband CPW band pass filters," *IEEE Microw. Wireless Compon. Lett.*, vol. **19**, pp. 197–199, 2009.

87. C. Caloz, "Dual composite right/left-handed (D-CRLH) transmission line metamaterial," *IEEE Microw. Wireless Compon. Lett.*, vol. **16**, pp. 585–587, 2006.

88. A. Rennings, S. Otto, J. Mosig, C. Caloz, and I. Wolff, "Extended composite right/left-handed metamaterial and its application as quadband quarter-wavelength transmission line," *Proc. Asia-Pacific Microw. Conf. (APMC)*, Yokohama, Japan, December 2006, pp. 1405–1408.

89. G. V. Eleftheriades, "A generalized negative-refractive-index transmission-line (NRL-TL) metamaterial for dual-band and quad-band applications," *IEEE Microw. Wireless Compon. Lett.*, vol. **17**, pp. 415–417, 2007.

90. G Sisó, M. Gil, J. Bonache, and F. Martín, "Generalized model for multiband metamaterial transmission lines," *IEEE Microw. Wireless Compon. Lett.*, vol. **18**, pp. 728–730, 2008.

91. C. Camacho-Peñalosa, T. M. Martín-Guerrero, J. Esteban, and J.E. Page, "Derivation and general properties of artificial lossless balanced composite right/left-handed transmission lines of arbitrary order," *Prog. Electromagn. Res. B*, vol. **13**, pp. 151–169, 2009.

92. A. Rennings, T. Liebig, C. Caloz, and I. Wolff, "Double-Lorentz transmission line metamaterial and its application to tri-band devices," *IEEE MTT-S Int. Microw. Symp., Dig.*, Honolulu, HI, June 2007, pp. 1427–1430.

93. R. A. Foster, "A reactance theorem," *Bell Syst. Tech. J.*, vol. **3**, pp. 259–267, 1924.

94. C. Caloz, H. Okabe, T. Iwai, and T. Itoh, "Transmission line approach of left handed materials," *USNC/URSI Natl. Radio Sci. Meet.*, San Antonio, TX, vol. **1**, June 2002, p. 39.

95. D. Sievenpiper, L. Zhang, R. F. J. Broas, N. G. Alexopolous, and E. Yablonovitch, "High impedance electromagnetic surfaces with a forbidden frequency band," *IEEE Trans. Microw. Theory Tech.*, vol. **47**, pp. 2059–2074, 1999.

96. Y. Horii, C. Caloz, T. Itoh, "Super-compact multilayered left-handed transmission line and diplexer application," *IEEE Trans. Microw. Theory Tech.*, vol. **53**, pp. 1527–1534, 2005.

97. Y. Horii, N. Inoue, T. Kawakami, and T. Kaneko, "Super-compact LTCC-based multilayered CRLH transmission lines for UWB applications," *Proc. 41st Eur. Microw. Conf.*, Manchester, UK, October 2011.

98. P. Turalchuk, I. Munina, P. Kapitanova, D. Kholodnyak, D. Stoepel, S. Humbla, J. Mueller, M. A. Hein, and I. Vendik, "Broadband small-size LTCC directional couplers," *Proc. 40 Eur. Microw. Conf.*, Paris, France, September 2010.

99. R. Marqués, F. Mesa, J. Martel, and F. Medina, "Comparative analysis of edge and broadside coupled split ring resonators for metamaterial design. Theory and experiment," *IEEE Trans. Antennas Propag.*, vol. **51**, pp. 2572–2582, 2003.

100. F. Aznar, M. Gil, J. Bonache, and F. Martín, "Modelling metamaterial transmission lines: a review and recent developments," *Opto-Electron. Rev.*, vol. **16**, pp. 226–236, 2008.

101. F. Aznar, J. Bonache, and F. Martín, "Improved circuit model for left handed lines loaded with split ring resonators," *Appl. Phys. Lett.*, vol. **92**, paper 043512, 2008.

102. L. Roglá, J. Carbonell, and V. E. Boria, "Study of equivalent circuits for open-ring and split-ring resonators in coplanar waveguide technology," *IET Microw. Antennas Propag.*, vol. **1**, pp. 170–176, 2007.

103. D. M. Pozar, *Microwave Engineering*, Addison Wesley, New York, 1990.

104. F. Aznar, M. Gil, J. Bonache, J. D. Baena, L. Jelinek, R. Marqués, and F. Martín, "Characterization of miniaturized metamaterial resonators coupled to planar transmission lines," *J. Appl. Phys.*, vol. **104**, paper 114501, 2008.

105. G. V. Eleftheriades, O. Siddiqui, and A. Iyer, "Transmission line models for negative refractive index media and associated implementations without excess resonators," *IEEE Microw. Wireless Compon. Lett.*, vol. **13**, pp. 51–53, 2003.

106. J. Bonache, M. Gil, O. García-Abad, and F. Martín, "Parametric analysis of microstrip lines loaded with complementary split ring resonators," *Microw. Opt. Technol. Lett.*, vol. **50**, pp. 2093–2096, 2008.

107. F. Aznar, M. Gil, J. Bonache, and F. Martín, "Revising the equivalent circuit models of resonant-type metamaterial transmission lines," *IEEE MTT-S Int. Microw. Symp. Dig.*, Atlanta, GA, June 2008.

108. M. Gil, J. Bonache, J. Selga, J. García-García, and F. Martín, "Broadband resonant type metamaterial transmission lines," *IEEE Microw. Wireless Compon. Lett.*, vol. **17**, pp. 97–99, 2007.

109. F. Aznar, M. Gil, J. Bonache, and F. Martín, "SRR- and CSRR-loaded metamaterial transmission lines: a comparison to the light of duality," *2nd Int. Congr. Adv. Electromagn. Mater. Microw. Opt. (Metamaterials'08)*, Pamplona, Spain, September 2008.

110. T. Tamir and A. A. Oliner, "Guided complex waves," *Proc. IEEE*, vol. **110**, pp. 310–34, 1963.

111. R. Islam and G. V. Eleftheriades, "On the independence of the excitation of complex modes in isotropic structures," *IEEE Trans. Antennas Propag.*, vol. **58**, pp. 1567–1578, 2010.

112. P. J. B. Clarricoats and K. R. Slinn, "Complex modes of propagation in dielectric loaded circular waveguide," *Electron. Lett.*, vol. **1**, pp. 145–146, 1965.

113. A. S. Omar and K. F. Schünemann, "The effect of complex modes at finline discontinuities," *IEEE Trans. Microw. Theory Tech.*, vol. **34**, pp. 1508–1514, 1986.

114. W. Huang and T. Itoh, "Complex modes in lossless shielded microstrip lines," *IEEE Trans. Microw. Theory Tech.*, vol. **36**, pp. 163–164, 1988.

115. F. Elek and G. V. Eleftheriades, "Dispersion analysis of the shielded Sievenpiper structure using multiconductor transmission line theory," *IEEE Microw. Wireless Compon. Lett.*, vol. **14**, pp. 434–436, 2004.

116. J. Naqui, M. Durán-Sindreu, A. Fernández-Prieto, F. Mesa, F. Medina, and F. Martín, "Multimode propagation and complex waves in CSRR-based transmission line metamaterials," *IEEE Antennas Wireless Propag. Lett.*, vol. **11**, pp. 1024–1027, 2012.

117. J. Naqui, A. Fernández-Prieto, F. Mesa, F. Medina, and F. Martín, "Effects of interresonator coupling in split ring resonator (SRR) loaded metamaterial transmission lines," *J. Appl. Phys.*, vol. **115**, paper 194903, 2014.

118. R. Mongia, I. Bahl, and P. Barthia, *RF and Microwave Coupled Line Circuits*, Artech House, Norwood, MA, 1999.

119. J. Shekel, "Matrix analysis of multi-terminal transducers," *Proc. IRE*, vol. **42**, pp. 840–847, 1954.

120. R. Islam, M. Zedler, and G. V. Eleftheriades, "Modal analysis and wave propagation in finite 2D transmission-line metamaterials," *IEEE Trans. Antennas Propag.*, vol. **59**, pp. 1562–1570, 2011.

121. M. Beruete, F. Falcone, M. J. Freire, R. Marqués, and J. D. Baena, "Electroinductive waves in chains of complementary metamaterial elements," *Appl. Phys. Lett.*, vol. **88**, paper 083503, 2006.

122. J. Naqui, M. Durán-Sindreu, and F. Martín, "Modeling split ring resonator (SRR) and complementary split ring resonator (CSRR) loaded transmission lines exhibiting cross polarization effects," *IEEE Ant. Wireless Propag. Lett.*, vol. **12**, pp. 178–181, 2013.

123. J. Naqui, A. Fernández-Prieto, M. Durán-Sindreu, F. Mesa, J. Martel, F. Medina, and F. Martín, "Common mode suppression in microstrip differential lines by means of complementary split ring resonators: theory and applications," *IEEE Trans. Microw. Theory Tech.*, vol. **60**, pp. 3023–3034, 2012.

124. M. Durán-Sindreu, A. Vélez, F. Aznar, G. Sisó, J. Bonache, and F. Martín, "Application of open split ring resonators and open complementary split ring resonators to the synthesis of artificial transmission lines and microwave passive components," *IEEE Trans. Microw. Theory Tech.*, vol. **57**, pp. 3395–3403, 2009.

125. M. Durán-Sindreu, *Miniaturization of planar microwave components based on semi-lumped elements and artificial transmission lines: application to multi-band devices and filters*, PhD dissertation, Universitat Autònoma de Barcelona, Barcelona, Spain, 2011.

126. M. Durán-Sindreu, P. Vélez, J. Bonache, and F. Martín, "Broadband microwave filters based on open split ring resonators (OSRRs) and open complementary split ring resonators (OCSRRs): improved models and design optimization," *Radioengineering*, vol. **20**, pp. 775–783, 2011.

127. J. Bonache, I. Gil, J. García-García, and F. Martín, "Novel microstrip band pass filters based on complementary split rings resonators," *IEEE Trans. Microw. Theory Tech.*, vol. **54**, pp. 265–271, 2006.

128. J. Bonache, M. Gil, I. Gil, J. García-García, and F. Martín, "Limitations and solutions of resonant-type metamaterial transmission lines for filter applications: the hybrid approach," *IEEE MTT-S Int. Microw. Symp. Dig.*, San Francisco, CA, June 2006, pp. 939–942.

129. M. Gil, J. Bonache, J. García-García, J. Martel, and F. Martín, "Composite right/left handed (CRLH) metamaterial transmission lines based on complementary split rings resonators (CSRRs) and their applications to very wide band and compact filter design," *IEEE Trans. Microw. Theory Tech.*, vol. **55**, pp. 1296–1304, 2007.